

**EFFECT OF SMALL FIELD DOSIMETRY ON ACCURACY OF
DOSE CALCULATION USING AAA 8.6 ALGORITHM
IN HEAD AND NECK IMRT**



THIDA NIYOMTHAI

**A THESIS SUBMITTED IN PARTIAL FULFILLMENT
OF THE REQUIREMENTS FOR
THE DEGREE OF MASTER OF SCIENCE
(MEDICAL PHYSICS)
FACULTY OF GRADUATE STUDIES
MAHIDOL UNIVERSITY**

2013

COPYRIGHT OF MAHIDOL UNIVERSITY

Thesis
entitled

**EFFECT OF SMALL FIELD DOSIMETRY ON ACCURACY OF
DOSE CALCULATION USING AAA 8.6 ALGORITHM
IN HEAD AND NECK IMRT**

Thida Niyomthai

Miss Thida Niyomthai
Candidate

L. Tuntipumiamorn

Assoc. Prof. Lalida Tuntipumiamorn,
M.Sc. (Radiation Science)
Major advisor

Puangpen Tanboonduangjit

Lect. Puangpen Tanboonduangjit,
Ph.D. (Medical Radiation Physics)
Co-advisor

Nuanpen Damrongkijudom

Lect. Nuanpen Damrongkijudom,
Ph.D. (Medical Radiation Physics)
Co-advisor

B. Mahaisavariya

Prof. Banchong Mahaisavariya,
M.D., Dip. Thai Board of Orthopedics
Dean
Faculty of Graduate Studies
Mahidol University

Puangpen Tanboonduangjit

Lect. Puangpen Tanboonduangjit,
Ph.D. (Medical Radiation Physics)
Program Director
Master of Science Program
in Medical Physics
Faculty of Medicine
Ramathibodi Hospital
Mahidol University

Thesis
entitled

**EFFECT OF SMALL FIELD DOSIMETRY ON ACCURACY OF
DOSE CALCULATION USING AAA 8.6 ALGORITHM
IN HEAD AND NECK IMRT**

was submitted to the Faculty of Graduate Studies, Mahidol University
for the degree of Master of Science (Medical Physics),

on
December 17, 2013

Thida Niyomthai

.....
Miss Thida Niyomthai
Candidate

Sivalee Suriyapee

.....
Assoc. Prof. Sivalee Suriyapee,
M.Eng. (Nuclear Technology)
Chair

Lalida Tuntipumiamorn

.....
Assoc. Prof. Lalida Tuntipumiamorn,
M.Sc. (Radiation Science)
Member

Puangpen Tanboonduangjit

.....
Lect. Puangpen Tanboonduangjit,
Ph.D. (Medical Radiation Physics)
Member

Nuanpen Damrongkijudom

.....
Lect. Nuanpen Damrongkijudom,
Ph.D. (Medical Radiation Physics)
Member

B. Mahaisavariya

.....
Prof. Banchong Mahaisavariya,
M.D., Dip. Thai Board of Orthopedics
Dean
Faculty of Graduate Studies
Mahidol University

Winit Phuapradit

.....
Prof. Winit Phuapradit,
M.D., M.P.H.
Dean
Faculty of Medicine
Ramathibodi Hospital,
Mahidol University

ACKNOWLEDGEMENTS

I would like to express my sincere gratitude and deep appreciation to my major advisor, Assoc. Prof. Lalida Tuntipumiamorn for her valuable guidance, comments, encouragement and support throughout all the time of this research. In addition, I am equally grateful to my co-advisors, Lect. Puangpen Tanbooungjit for the suggestions, constructive comments in the experiments and the presentation and Lect. Nuanpen Damrongkijudom for the valuable assistance on the knowledge in TLD preparation and calibration process.

I would like to express sincere thanks to Asst. Prof. Chirapa Tannanonta, Chief of Medical Physicist, Chulabhorn Hospital for her constructive advice and comments in the research proposal.

I am grateful for the good cooperation from all therapists, engineering and staffs in Division of Radiation Oncology, Department of Radiology, Faculty of Medicine, Siriraj Hospital. I am also thankful to Mr. Wutthichai Boonrat and Miss Patchareporn Dechsupa for the assistance, nicely consultant during collecting beam data. I wish to thank Miss Siwaporn Sakulsingharoj and Department of Diagnostic and Therapeutic Radiology, Ramathibodi hospital for the support in this experiment. Specially thank is express to Miss Lukkana Apipunyasopon, Miss Khummook Krongyuth and Miss Piyanan Liammookda for their assistance, comments, discussion, and kindness cheer up, without their support this thesis cannot complete.

I am also thankful to all teachers, lectures, staffs and my classmates in the School of Medical Physics at Division of Radiation Oncology and Nuclear Medicine, Ramathibodi Hospital for their kind support and teaching me in the Medical Physics Program.

Finally, I have to sincerely regard mention to my parents. Thank you for their understanding, love and inspiration throughout my whole study. The productiveness of this thesis, I dedicate to my family and all teachers who taught me since my childhood.

Thida Niyomthai

EFFECT OF SMALL FIELD DOSIMETRY ON ACCURACY OF DOSE CALCULATION USING AAA 8.6 ALGORITHM IN HEAD AND NECK IMRT

THIDA NIYOMTHAI 5236464 RAMP/M

M.Sc. (MEDICAL PHYSICS)

THESIS ADVISORY COMMITTEE: LALIDA TUNTIPUMIAMORN, M.Sc. (RADIATION SCIENCE), NUANPEN DAMRONGKIJUDOM, Ph.D. (MEDICAL RADIATION PHYSICS), PUANGPEN TANGBOONDUANGJIT, Ph.D. (MEDICAL RADIATION PHYSICS)

ABSTRACT

The main objective of this study was to determine the accuracy, limitation and evaluate the effect of additional small field beam dosimetry of AAA algorithm [version 8.6] on Eclipse treatment planning system for calculating dose distribution in head and neck treatment using IMRT technique. Eclipse TPS were commissioned using three different beam datasets. The dataset A, B and C which included the depth doses, 5 depths profiles and output factors were collected for the field size in the range of 1×1 - 40×40 cm², 2×2 - 40×40 cm² and 3×3 - 40×40 cm² respectively. For the small field less than 3×3 cm², relative beam dosimetry was measured with the beam scanning system using SRS diode detector and using 0.015 cm³ Pinpoint chamber for the output measurement. Evaluation of the IMRT dose calculation was performed by generating the seven-field, sliding window, head and neck IMRT plan on the humanoid head and neck phantom. Three dose distribution plans were then computed using each commissioned beam data. Accuracy of the calculated dose on each plan was verified with the measured doses from MapCHECK QA system and TLD-100 dosimeters. The measurements with TLD dosimeters were repeated three times for each plan.

The result of the verification showed all IMRT plans that were calculated from beam dataset A, B and C presented a similar number of segments, monitor units, segment shape and dose distribution. Accuracy of the measurement was found to be satisfactorily acceptable, by percent difference between TLD measured dose and calculation dose at point of the central axis was within $\pm 3\%$. About fifty percent of TLD measuring points from total number of sixty points were detected to be 10% greater than the TPS calculated dose. Average percent differences of the measurement from calculation dose were observed to be 9.284 ± 3.751 , 9.827 ± 3.3771 and 9.88 ± 3.358 , for IMRT plan A, B and C, respectively. However, the planar dose distribution of all IMRT plan that verify with the MapCHECK QA system are passed within 98-99% using the criteria of dose difference 3% and 3 mm. DTA. From these results, It can be concluded that the addition of the small field beam data for the AAA 8.6 commissioning does not affect on the quality of IMRT dose calculation. It is noticeable that the underestimation of the AAA dose calculation will be furthered investigated from TLD-100 measurement but it was disable to detect in MapCHECK QA system. Further study is needed to confirm the effect of additional small field beam dosimetry. The verification should be included on the other head and neck IMRT or SRS plans and high-resolution measurement techniques used such as film dosimetry for planar and point dose measurement.

KEY WORDS : AAA 8.6/SMALL FIELD BEAM DATA/ DOSIMETRIC VERIFICATION

89 pages

ผลของข้อมูลลำรังสีในพื้นที่ขนาดเล็กต่อความถูกต้องของการคำนวณรังสีจากการใช้สมการคำนวณชนิด AAA เวอร์ชัน 8.6 ในเทคนิคการฉายรังสีแบบปรับความเข้มของมะเร็งบริเวณศีรษะและลำคอ
EFFECT OF SMALL FIELD DOSIMETRY ON ACCURACY OF DOSE CALCULATION USING AAA 8.6 ALGORITHM IN HEAD AND NECK IMRT

ธิดา นิยมไทย 5236464 RAMP/M

วท.ม. (ฟิสิกส์การแพทย์)

คณะกรรมการที่ปรึกษาวิทยานิพนธ์ : ลลิตา ดันติภูมิอมร, M.Sc. (RADIATION SCIENCE), นวลเพ็ญ คำรังกิจอุดม, Ph.D. (MEDICAL RADIATION PHYSICS), พวงเพ็ญ ตั้งบุญดวงจิตร, Ph.D. (MEDICAL RADIATION PHYSICS)

บทคัดย่อ

วัตถุประสงค์ของงานวิจัยนี้คือการประเมินข้อจำกัดและความแม่นยำในการคำนวณการกระจายรังสี ของสมการคำนวณปริมาณรังสีแบบ AAA 8.6 ที่มีการเพิ่มข้อมูลลำรังสีในพื้นที่ขนาดเล็ก ในการฉายรังสีมะเร็งศีรษะและลำคอด้วยเทคนิคการฉายรังสีแบบปรับความเข้ม เครื่องวางแผนการรักษาจะทำการคำนวณโดยใช้ข้อมูลลำรังสีที่แตกต่างกัน 3 ชุด ชุดข้อมูลที่ใช้ในการทดสอบประกอบไปด้วย depth doses, beam profiles ที่ 5 ระดับความลึกและ output factors ซึ่งจัดเก็บในขนาดพื้นที่ต่างกันคือ $1 \times 1-40 \times 40$, $2 \times 2-40 \times 40$ และ $3 \times 3-40 \times 40$ ตารางเซนติเมตร สำหรับข้อมูลชุด A, B และ C ตามลำดับ การเก็บข้อมูล depth doses และ beam profiles ในพื้นที่ขนาดต่ำกว่า 3×3 ตารางเซนติเมตร จะใช้หัววัดรังสีชนิด SRS diode ส่วนค่า output factor จะเก็บข้อมูลโดยใช้หัววัดรังสีชนิด Pinpoint ขนาด 0.015 ลูกบาศก์เซนติเมตร การคำนวณการกระจายรังสีใน humanoid head and neck phantom ด้วยแผนการรักษาทดสอบแบบ sliding window IMRT ซึ่งใช้มุมในการฉายรังสี 7 มุม แต่ละแผนการรักษาจะคำนวณโดยใช้ข้อมูลลำรังสีที่เตรียมไว้ในแต่ละชุด ตรวจสอบถูกต้องของการคำนวณโดยใช้ MapCHECK QA system และหัววัดรังสีชนิด TLD-100 การวัดรังสีโดยใช้หัววัดรังสีชนิด TLD จะทำซ้ำ 3 ครั้งในทุกแผนการรักษา

ผลของการศึกษาพบว่าทุกแผนการรักษาทดสอบจะมีจำนวนและรูปร่างของ segments, monitor units และรูปแบบการกระจายรังสีที่คล้ายกัน เมื่อประเมินความถูกต้องของการวัดปริมาณรังสีในการศึกษานี้พบว่า มีความแม่นยำที่ยอมรับได้ เนื่องจากมีความแตกต่างของค่าปริมาณรังสีในแนวกึ่งกลางระหว่างการวัดและการคำนวณมีค่าไม่เกิน 3% เมื่อตรวจสอบความแตกต่างระหว่างการวัดและการคำนวณพบว่าประมาณครึ่งหนึ่งจากทั้งหมด 60 ตำแหน่งที่ทำการวัด มีค่าปริมาณรังสีมากกว่าการคำนวณอยู่ 10% ค่าเฉลี่ยเปอร์เซ็นต์ความแตกต่างของปริมาณรังสีที่ได้จากการวัดเทียบกับการคำนวณมีค่า 9.284 ± 3.751 , 9.827 ± 3.3771 และ 9.88 ± 3.358 ในแผนการรักษา A, B และ C ตามลำดับ อย่างไรก็ตามการเปรียบเทียบการกระจายรังสีในแนวระนาบซึ่งวัดโดย MapCHECK QA system ซึ่งเปรียบเทียบโดยใช้เกณฑ์การยอมรับความผิดพลาดที่ dose difference 3% และ 3 mm. DTA กลับพบว่ามีความสอดคล้องกัน 98-99% ในทั้งสามแผนการรักษา จากผลการศึกษาสามารถสรุปได้ว่าการเพิ่มข้อมูลลำรังสีในพื้นที่ขนาดเล็กไม่ส่งผลกระทบต่อคุณภาพของการคำนวณปริมาณรังสีในเทคนิคการฉายแบบปรับความเข้มของ AAA 8.6 เป็นที่น่าสังเกตว่าค่าปริมาณรังสีที่น้อยกว่าของการคำนวณเมื่อเปรียบเทียบกับที่วัดด้วย TLD-100 กลับไม่สามารถตรวจพบได้จาก MapCHECK QA system จึงควรมีการศึกษาเพิ่มเติมเพื่อยืนยันผลดังกล่าวในแผนการรักษาอื่นๆ ของมะเร็งศีรษะและลำคอ โดยใช้เทคนิคการวัดปริมาณรังสีที่มีความละเอียดสูงเช่น film dosimetry

CONTENTS

	Page
ACKNOWLEDGEMENTS.....	iii
ABSTRACT (ENGLISH).....	iv
ABSTRACT (THAI).....	v
LIST OF TABLES.....	vii
LIST OF FIGURES.....	ix
LIST OF ABBREVIATIONS.....	xv
CHAPTER I INTRODUCTION.....	1
CHAPTER II OBJECTIVES.....	8
CHAPTER III LITERATURE REVIEW.....	9
CHAPTER IV MATERIALS AND METHODS.....	18
CHAPTER V RESULTS.....	40
CHAPTER VI DISCUSSION AND CONCLUSIONS.....	66
REFERENCES.....	73
APPENDICES.....	77
BIOGRAPHY.....	89

LIST OF TABLES

Table	Page
1.1 Typical commissioning measurements for photon beam data [14]	6
4.1 The required field sizes of small and rectangular fields for output factors measurement	29
4.2 Proposed values of the tolerances for δ for application in different test configuration [42]	31
5.1 Mean (\bar{X}), standard deviation (SD), percentage of coefficient of variation (%CV) of TLD readings and their individual calibration factor (CF)	40
5.2 The output factors in the series of field size, value in blue obtaining from field size 1×1 and 2×2 cm ² and black from the routine measurement data of 3×3-40×40 cm ² field .	46
5.3 The measured and calculated dose in 1×1, 2×2, 3×3, 5×5, 10×10 and 20×20 cm ² . The calculation was performed with three beam data set at depth 10 cm, SSD 90 cm in water phantom.	52
5.4 Gantry angle and detail of treatment field used in IMRT plan	53
5.5 Comparison of the monitor unit (MU) and field segmentation in three calculated IMRT plans	54
5.6 The subfield area in field segment no.1 and no.2 of three IMRT plans	57
5.7 The subfield area in field segment no.3 and no.4 of three IMRT plans	57
5.8 Summation of the maximum dose (D_{max}), mean dose (D_{mean}) and minimum dose (D_{min}) in the target volumes and organ at risks of the IMRT calculated on beam data set A, B and C, respectively.	59
6.1 The result of depth dose verification in 1×1, 2×2, 3×3 and 10×10 cm ² at d_{max} depth of three beam data sets	67
6.2 The result of beam profile verification in 1×1, 2×2, 3×3 and 10×10 cm ² at d_{max} depth of three beam data sets.	68

LIST OF TABLES (cont.)

Table		Page
6.3	The result of beam profile verification in 1×1 , 2×2 , 3×3 and 10×10 cm^2 at 10 cm depth of three beam data sets.	69

LIST OF FIGURES

Figure	Page
1.1 The step-and-shoot IMRT technique: The intensity patterns are composed from a number of field segments in each gantry position.	3
1.2 The sliding window or dynamic IMRT technique: Modulated intensity are created from moving leaves independently in unidirectional while the beam is on.	3
3.1 A diagram illustrated the different lateral build up field configuration for the relative output measurement using ion chamber.	12
4.1 Scanditronix-Wellhofer Blue phantom dosimetry systems	18
4.2 MT-150 water phantom	19
4.3 Farmer chamber (a), Pinpoint chamber (b) and Diode detector (c)	20
4.4 Electrometer DOSE1 from IBA dosimetry	21
4.5 Varian Clinac 23 EX linear accelerator	21
4.6 Anthropomorphic phantom: Anderson radiation therapy phantom (ART)	22
4.7 Brilliance Computed Tomography 16-slice machine	23
4.8 Thermoluminescence dosimeters (TLD-100) rod and vacuum tweezers set	24
4.9 Harshaw model 5500 TLD reader	24
4.10 TLDO annealing oven	25
4.11 MapCHECK2 TM (a) and MapPHAN TM (b)	26
4.12 The 6 MV photon depth dose curve for field size 1×1 and 2×2 cm ²	27
4.13 The x-plane profile of 1×1 cm ² field at d _m , 5, 10, 20 and 30 cm depth	28
4.14 The x-plane profile of 2×2 cm ² field at d _m , 5, 10, 20 and 30 cm depth.	28
4.15 The verification criteria to compare calculated and measured depth-dose (PDD) curves (a) and cross plan profiles (b)	32
4.16 The ART phantom was scanned in CT simulation	33

LIST OF FIGURES (cont.)

Figure	Page
4.17 2D dose distribution IMRT verification using MapCHECK2™ and MapPHAN™	34
4.18 The TLD measuring points were shown in eight slabs of humanoid head and neck phantom. The number in each point represents the position of TLD.	36
4.19 TLDs holders (a) and two TLDs were packed in the holder (b)	38
4.20 The holder was placed at the measurement point in ART phantom (a) and the phantom was irradiated with Varian Clinac 23EX linear accelerator (b).	39
5.1 The comparison of PDD curves between the calculation (red) and measurement (blue) on beam dataset A (1×1-40×40 cm ²) in 1×1 cm ² field size at 100 cm SSD	47
5.2 The comparison of PDD curves between the calculation (red) and measurement (blue) on beam dataset A (1×1-40×40 cm ²) in 2×2 cm ² field size at 100 cm SSD.	47
5.3 The comparison of PDD curves between the calculation (red) and measurement (blue) on beam dataset A (1×1-40×40 cm ²) in 3×3 cm ² field size at 100 cm SSD.	48
5.4 The comparison of PDD curves between the calculation (red) and measurement (blue) on beam dataset A (1×1-40×40 cm ²) in 10×10 cm ² field size at 100 cm SSD.	48
5.5 Comparison of the cross plane profiles between calculation and measurement in 1×1 cm ² field size from beam commissioning data 1×1-40×40 cm ²	49
5.6 Comparison of the cross plane profiles between calculation and measurement in 2×2 cm ² field size from beam commissioning data 1×1-40×40 cm ²	49

LIST OF FIGURES (cont.)

Figure	Page
5.7 Comparison of the cross plane profiles between calculation and measurement in 3×3 cm ² field size from beam commissioning data 1×1 - 40×40 cm ²	50
5.8 Comparison of the cross plane profiles between calculation and measurement in 10×10 cm ² field size from beam commissioning data 1×1 - 40×40 cm ²	50
5.9 Virtual water phantoms were simulated in the Eclipse treatment planning system and used to calculate the point dose at depth 10 cm , SAD =100 cm in 1×1 (a), 2×2 (b), 3×3 (c), 5×5 (d), 10×10 (e) and 20×20 (f) cm ² field size.	51
5.10 Beam directions of seven-field head and neck IMRT treatment plan in ART phantom, shown in 2D view (a) and 3D view (b).	53
5.11 Four samples of IMRT segmental shapes observed at gantry 0 degree on three different plans of head and neck IMRT.	55
5.12 Four samples of IMRT segmental shapes observed at gantry 220 degree on three different plans of head and neck IMRT	56
5.13 Cumulative DVH of (a) the clinical target volumes (CTV70, CTV59.4 and CTV 54) and (b) spinal cord, brainstem and brain (right and left temporal lobes) in all three IMRT plans	58
5.14 Planar dose distribution verified with MapCHECK on three head and neck IMRT plans. Left side (a), (c), (e) are the measured dose distribution obtained from IMRT plan A, B and C, respectively and the right side are the TPS planned dose	60
5.15 The percent difference of the calculation dose in plan A compared with the TLDs measurement for each point	62
5.16 The percent difference of the calculation dose in plan B compared with the TLDs measurement for each point	63

LIST OF FIGURES (cont.)

Figure	Page
5.17 The percent difference of the calculation dose in plan C compared with the TLDs measurement for each point	64
5.18 Percent dose difference between calculation and measurement at each TLD point in humanoid head and neck phantom of three IMRT plans	65
5.19 The percent difference frequency between the measurement and the calculation of three IMRT plans.	65
6.1 Percent dose difference between calculation and measurement at each TLD point in humanoid head and neck phantom, compared between AAA 8.6 and 8.9 version.	71
B.1 The comparison of PDD curves between the calculation (red) and measurement (blue) on beam data set B (2×2 - 40×40 cm ²) in 1×1 cm ² field size at 100 cm SSD.	79
B.2 The comparison of PDD curves between the calculation (red) and measurement (blue) on beam data set B (2×2 - 40×40 cm ²) in 2×2 cm ² field size at 100 cm SSD.	80
B.3 The comparison of PDD curves between the calculation (red) and measurement (blue) on beam data set B (2×2 - 40×40 cm ²) in 3×3 cm ² field size at 100 cm SSD.	80
B.4 The comparison of PDD curves between the calculation (red) and measurement (blue) on beam data set B (2×2 - 40×40 cm ²) in 10×10 cm ² field size at 100 cm SSD.	81
B.5 The comparison of PDD curves between the calculation (red) and measurement (blue) on beam data set C (3×3 - 40×40 cm ²) in 1×1 cm ² field size at 100 cm SSD.	81

LIST OF FIGURES (cont.)

Figure	Page
B.6 The comparison of PDD curves between the calculation (red) and measurement (blue) on beam data set C ($3\times 3\text{-}40\times 40\text{ cm}^2$) in $2\times 2\text{ cm}^2$ field size at 100 cm SSD.	82
B.7 The comparison of PDD curves between the calculation (red) and measurement (blue) on beam data set C ($3\times 3\text{-}40\times 40\text{ cm}^2$) in $3\times 3\text{ cm}^2$ field size at 100 cm SSD.	82
B.8 The comparison of PDD curves between the calculation (red) and measurement (blue) on beam data set C ($3\times 3\text{-}40\times 40\text{ cm}^2$) in $10\times 10\text{ cm}^2$ field size at 100 cm SSD.	83
B.9 Comparison of the cross plane profiles between calculation (red) and measurement (blue) in $1\times 1\text{ cm}^2$ field size from beam commissioning data set B ($2\times 2\text{-}40\times 40\text{ cm}^2$)	83
B.10 Comparison of the cross plane profiles between calculation (red) and measurement (blue) in $2\times 2\text{ cm}^2$ field size from beam commissioning data set B ($2\times 2\text{-}40\times 40\text{ cm}^2$)	84
B.11 Comparison of the cross plane profiles between calculation (red) and measurement (blue) in $3\times 3\text{ cm}^2$ field size from beam commissioning data set B ($2\times 2\text{-}40\times 40\text{ cm}^2$)	84
B.12 Comparison of the cross plane profiles between calculation (red) and measurement (blue) in $10\times 10\text{ cm}^2$ field size from beam commissioning data set B ($2\times 2\text{-}40\times 40\text{ cm}^2$)	85
B.13 Comparison of the cross plane profiles between calculation (red) and measurement (blue) in $1\times 1\text{ cm}^2$ field size from beam commissioning data set C ($3\times 3\text{-}40\times 40\text{ cm}^2$)	85

LIST OF FIGURES (cont.)

Figure	Page
B.14 Comparison of the cross plane profiles between calculation (red) and measurement (blue) in $2 \times 2 \text{ cm}^2$ field size from beam commissioning data set C (3×3 - $40 \times 40 \text{ cm}^2$)	86
B.15 Comparison of the cross plane profiles between calculation (red) and measurement (blue) in $3 \times 3 \text{ cm}^2$ field size from beam commissioning data set C (3×3 - $40 \times 40 \text{ cm}^2$)	86
B.16 Comparison of the cross plane profiles between calculation (red) and measurement (blue) in $10 \times 10 \text{ cm}^2$ field size from beam commissioning data set C (3×3 - $40 \times 40 \text{ cm}^2$)	87

LIST OF ABBREVIATIONS

Abbreviation	Term
2D	Two Dimensions
3D	Three Dimensions
3D-CRT	Three-dimensional conformal radiation therapy
AAA	Anisotropic Analytical Algorithm
AAPM	American Association of Physicists in Medicine
C	coulomb
CAX	Central axis
cc	Cubic centimeter
CF	Calibration factor
cGy	Centigray
cm	Centimeter
cm ²	Square centimeter
cm ³	Cubic centimeter
CPE	Charge Particle Equilibrium
CT	Computed tomography
CTV	Clinical target volume
CV	Coefficient of variation
d _{max}	Depth of dose maximum
D _{max}	Maximum dose
D _{mean}	Mean dose
D _{min}	Minimum dose
DTA	Distance to agreement
DVH	Dose volume histograms
EDW	Enhance dynamic wedges

LIST OF ABBREVIATIONS (cont.)

Abbreviation	Term
FSPB	Finite size pencil beam
g	gram
GTV	Gross tumor volume
Gy	Gray
ICRU	International Commission on Radiation Units and Measurements
IMRT	Intensity modulated radiotherapy
IMST	Intensity-modulated stereotactic radiotherapy
KeV	kiloelectron volt
kV	Kilovolts
LiF	Lithium fluoride
LINAC	Linear accelerator
mA	milliampere
MeV	Megaelectron volt
Mg	Magnesium
MLC	Multileaves collimator
mm	Millimeter
mm ³	Cubic millimeter
MOSFET	Metal-oxide silicon semiconductor field- effect transistor
MU	Monitor unit
MV	Megavolt
N ₂	Nitrogen gas
nA	Nanoampere
nC	Nanocoulomb
No.	Number

LIST OF ABBREVIATIONS (cont.)

Abbreviation	Term
OAR	Organs at risk
°C	Celsius
OF	Output factor
pA	Picoampere
pC	picocoulomb
PDD	Percent depth doses
pGy	picogray
PMMA	Polymethyl methacrylate
PTV	Planning target volume
QA	Quality assurance
R	Roentgen
RT	radiotherapy
RW	Radiological width
SAD	Source axis distance
S_{cp}	Total output factors
SD	Standard deviation
sec	Seconds
SFD	Stereotactic field detector
SRS	Stereotactic radiosurgery
SSD	Source skin distance
Sv	Sievert
TERMA	Total energy released per unit mass
TG	Task group
Ti	Titanium
TLD	Thermoluminescent dosimetry
TPS	Treatment planning systems
TSF	Total scatter factors

LIST OF ABBREVIATIONS (cont.)

Abbreviation	Term
\bar{X}	Mean



CHAPTER I

INTRODUCTION

Head and neck cancer is the sixth most common cancer worldwide and the statistics showed a record of about 640,000 diagnosed cases per year with approximately 350,000 deaths [1]. Current treatment options for head and neck cancer typically include surgery, radiotherapy and chemotherapy. The type and combination of treatments will depend on the site and stage of the cancer, as well as the patient's overall health status. For radiotherapy (RT), it has long been a crucial therapeutic modality in head and neck carcinoma as the multimodality or as the primary treatment. However, anatomy of the head and neck consists of many functional organs which are critical to patients' quality of life. In addition, the complex irregular shape of the target volumes, usually are adjacent to many surrounding critical structures. Thus, the dose delivered to tumor was often limited by the radiation tolerance of surrounding structures. With the conventional radiation treatment technique, the maximum feasible tumor dose was usually between 65 to 70 Gy. At this dose, the recurrence chance has been increasing [2], since the tumor control probability is highly correlated with the tumor dose received.

Advances in computer technology have significantly impacted on treatment of the head and neck carcinoma. The driven computer-controlled linear accelerator provide a capability to generate the three dimensional dose distribution that sharply conform to the target while minimizing the dose delivered to the surrounding normal tissues. The technology is then further developed to be the intensity modulated radiotherapy (IMRT) which the radiation beam in any direction will be split into a number of beamlets. This method allows the intensities across the beam are varied and can be painted the required dose to each organ of interest. Hunt et al (2000) had compared the IMRT technique with the traditional and three-dimensional conformal radiation therapy (3D-CRT) on 23 primary nasopharyngeal cancer patients. The study showed that the mean planning target volume (PTV) dose can be increased from 67.9

Gy in conventional technique, to be 74.6 Gy with 3D-CRT and upto 77.3 Gy when using IMRT technique, respectively. PTV dose coverage from IMRT plans were as well improved in the parapharyngeal region and all normal structures received minimal dose when compared to the other treatment approaches. Promising clinical outcomes from head and neck IMRT treatment were as well shown on many reports [3, 4, 5, 6].

1.1 Intensity-modulated radiation therapy (IMRT)

By principle, IMRT is an advanced form of 3D-CRT technique, in which the non-uniform fluence can be delivered across the radiation beam. Using the three dimensional computed tomography imaging of the patient to identify and contour the target volumes and surrounding avoided structures. Then a number of different beam directions were selected at the appropriate angles and were optimized to deliver a high dose to the target volume and passable low dose to the surrounding normal organs. To obtain this objective, each radiation beam is subdivided into a large number of field segmentations with their individual intensity level. The optimal setting fluence was determined to satisfy to the predefined dose distribution criteria. To be successfully implemented in a clinic, IMRT technique requires an inverse treatment-planning computer system and the radiation treatment machine with a capability to deliver the non-uniform fluences as planned.

Typically, the linear accelerator (LINAC) equipped with the multileaves collimator (MLC) is a common method to provide the intensity modulation in IMRT technique. Advantage of the MLCs is the smaller shaping of the radiation beam (up to the millimeter) with the designed intensities can be created. Fluence distribution will be modulated by motion of the leaves and jaws which were controlled by the computer software. Generally, there are two approaches for IMRT delivery using MLCs; the step-and-shoot and sliding window techniques. The method of step-and-shoot is based on the superposition of the intensity in each beamlet, in order to create the modulation of the dose distribution across the field. In this technique, the collimator shape is set prior to the irradiation and there is no MLC motion during the beam is turned on as the diagram shown in figure 1.1. The desired intensity pattern is obtained by the fractional

weight summary of the intensity pattern from all subfields. In dynamic approach, intensity modulated fields are created by moving leaves independently while the beam is on. In this technique, the gantry does not move during irradiation, only the collimator shape changes during irradiation [7, 8] as shown in figure 1.2.

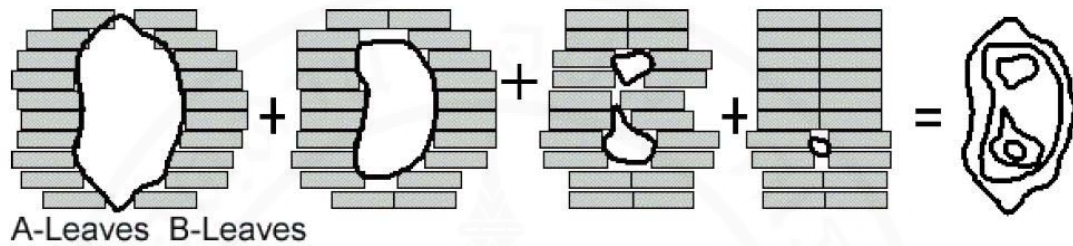


Figure 1.1 The step-and-shoot IMRT technique: The intensity patterns are composed from a number of field segments in each gantry position [9].

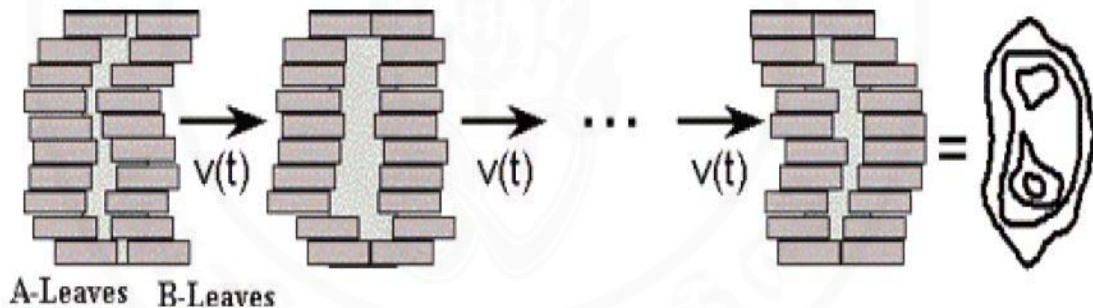


Figure 1.2 The sliding window or dynamic IMRT technique: Modulated intensity are created from moving leaves independently in unidirectional while the beam is on [9].

1.2 Computerized treatment planning systems (TPS)

1.2.1 Inverse Planning System

In practice, uniform dose distribution can be obtained from the forward planning method which works well for tumors of simple shape and not surrounded by numerous critical structures. For the complex tumor geometries, this may be limited from the experience of the planner and by the restricted beam intensity variation inside each beam. In IMRT planning, many small beamlets and problem of determining individual intensities is very complex. Thus it required computerized methods for solution which was called the inverse planning. In this process, the planner designates

beam directions, the plan outcome in terms of the tumor dose and normal structure dose limits. Then the dose calculation algorithm calculates the resulting dose distribution which will be compared with the prescribed dose distribution, specified by the radiation oncologist. If the desired dose distribution is not met, beam intensity and MLC movement's model will be adjusted by the optimization algorithm until the intensity patterns best matched to the desired plan.

1.2.2 Dose Calculation Algorithm for IMRT

Dose calculation algorithms are important components on the computerized treatment planning systems. They perform as a central role for the clinical practice of radiation therapy and become increase significantly in the development of complex treatment technique such as IMRT. They are generally classified as the correction-based and model-based algorithm. The correction-based methods use the complete set of beam measurement data in homogeneous water phantom. The patient dose is calculated by extrapolating the beam data from the measurements and applied correction factors for the effects such as irregular shaped fields, patient surface contour and primary beam modulators. The limitation of the algorithms were the assumption of electronic equilibrium and inaccurate of tissue inhomogeneity. On the other hand, the model-based algorithms do consider the energy deposition around photon interaction sites. The algorithm provides more realistic description of the absorbed dose in the heterogeneous media because it separates the effect of primary photons incident from the effect of secondary radiation generated within the patient.

Model-based dose calculation concept algorithms require a minimal amount of measurement data. The photon beam fluence will be modeled into three components - primary photon fluence, total energy released per unit mass and dose kernels. The photons emerging from the linear accelerator were used to model the primary energy fluence (radiation output). This data was calibrated to measured data for the simple fields under reference conditions. The total energy released per unit mass (TERMA) was considered of the energy absorption within the patient. And the transport of this energy via secondary electrons and photons is accounted for dose kernels, which describes in different levels of the energy transport. For the application

to inhomogeneous patient geometries, the dose has to account for the local tissue densities follow the electron densities derived from CT images [8, 10, 11].

The accuracy of dose calculation algorithms is directly affects to the patient dose. The International Commission on Radiation units and measurements [12] recommends that radiation dose be delivered within $\pm 5\%$ of the prescribed dose. The uncertainty of each step in the treatment process is required to be minimal and the total error has to be less than the quoted 5%. Therefore well understanding of the algorithm details is necessary in order to comprehend the limitations of accuracy in dose calculations in IMRT.

1.2.3 Treatment Plan Verification

The objective of plan validation is to verify that the accurate dose and dose distribution will be delivered to the patient. Treatment plan verification will help to determine the accuracy of the entire process which includes beam parameters setting and dose calculation algorithm. Usually the algorithms afford reasonable accuracy of dose calculation in reference conditions but they do have some uncertainties in clinical situation such as tissue inhomogeneities or small field condition. The ability of algorithm to compute the correct dose at any point depended on the completeness and accuracy of measurement beam data. AAPM Task Group No. 53 [13] has provided the treatment planning commissioning verification which is divided in two categories: (1) comparisons involving simple water phantom-type geometries and (2) comparisons involving complex geometries in clinical situations. These complex tests are critical for evaluating and use to explain the limitation of dose calculation.

Most of the IMRT verification tests require the system which allows the calculated and measured intensity pattern can be compared and examined. Normally, the process was performed by applying the desired complex intensity obtained from a number of MLC segments, leaf sequence and MU on each IMRT field from the patient specific plan to the measurement phantom which contained an appropriate set of dosimeters. This TPS calculated phantom plan will be verified with the measured data which included the absorbed dose at point of central axis and relative planer dose distribution. The criterion of 3% of dose difference and 3 mm distance to agreement (DTA) was typically used to evaluate the accuracy of the IMRT treatment plan.

1.2.4 Commissioning the radiation treatment planning system (TPS)

To obtain the successful treatment outcome, the accurate absorbed dose has to be delivered to the patient. And the accurate calculated dose from radiation treatment planning system is one of the most important factors for this objective. Commissioning the TPS to provide the accurate computed dose, it as well depends on the type and amount of the beam data specified by the TPSs. Normally, they are the percent depth doses (PDD) beam data-acquired at the central axis on a number of open and wedged fields from water phantom surface to depth 40 cm [14]. For a capability to generate the isodose distributions, they also needed the different depths of beam profiles with adequate penumbra tails, measured on of the same set of field sizes as on PDD measurement. The output factors are another parameters required by the TPS to calculate the absorbed dose. The MLCs create the small field segments, their commissioning data such as light and radiation field congruence, interleaf and intraleaf leakage, tongue and groove effect, and leaf penumbra also was needed for the TPS. To obtain the accurate dosimetry, AAPM report TG 106 [14] has recommended the commissioning measurements for photon beam data, which depend on the level of accuracy needed in the clinical application as shown in Table 1.1

Table 1.1 Typical commissioning measurements for photon beam data [14]

(a)	Description	Square field size (cm)																
		1	2	3	4	5	6	8	10	12	14	16	20	25	30	40	>40	
Scan data	Application PDD/TMR	×	×	×	×	×	×	×	×	×	×	×	×	×	×	×	×	×
	Profiles @ 5-7 depths Diagonal or star profiles	×	×	×	×	×	×	×	×	×	×	×	×	×	×	×	×	×
Nonscan data	S_c	×	×	×	×	×	×	×	×	×	×	×	×	×	×	×	×	×
	S_{cp}	×	×	×	×	×	×	×	×	×	×	×	×	×	×	×	×	×
	WF/TF				×	×	×	×	×	×	×	×	×	×	×	×	×	×
	Surface dose	×	×	×	×	×	×	×	×	×	×	×	×	×	×	×	×	×

1.3. Small field dosimetry

Both step-and-shoot and dynamic IMRT uses a combination of many small subfields to create intensity pattern. For accurate IMRT dose calculation, the

collection of small beam dosimetry, 1×1 - 3×3 cm², are recommended as shown in Table 1.1. For these narrow fields, the disequilibrium condition is able to introduce significant uncertainty in the clinical dosimetry. There are challenges to expect the accuracy of small field dosimetry. Firstly, the definition is not clear, commonly means the field size less than 3×3 cm². Beam energy, medium composition and density were the factors to consider the small field condition. The Charge Particle Equilibrium (CPE) is associated with the range of secondary particle by the lateral range is the critical parameter rather than the forward range of the electron. Hence, this condition is called lateral disequilibrium. It is obtained at the central axis of beams when the lateral electron range exceeds the beam radius. Therefore, small field can define as a field with a size smaller than the lateral range of charged particles [15].

When the CPE condition does not exist, a special attention on the physical size as well as the water equivalent of the detectors was needed. They can change the photons and electrons energy transportation and their interaction properties. The choice of a suitable detector for small field dosimetry is a challenging and can be a confusing task without proper guidelines. Normally, the small volume detectors were often used for the small field dosimetry such as microion chambers, semiconductor diode detectors, diamond detector, thermoluminescent dosimetry (TLD), film and metal-oxide silicon semiconductor field-effect transistor (MOSFET) dosimeters [14]. These detectors have an appropriate and limitation for different application. For example, small volume ion chamber and diodes are suited for beam data commissioning but should not be for all field size. TLD has been used for point dose measurement for verification in small fields and IMRT. Film is used for dose distribution measurement with high resolution but may not be accurate in data acquired than ion chambers. The selection of detectors should be considered in types of application, resolution and field size including time needed to data collection.

CHAPTER II

OBJECTIVES

The main objectives of this study are:

1. To evaluate an effect of additional small field beam dosimetry on accuracy of the head and neck IMRT dose distribution calculated by AAA algorithm [version 8.6] on Eclipse treatment planning system.
2. To determine the accuracy and limitation of AAA algorithm [version 8.6] for calculating dose distribution in head and neck treatment using IMRT technique.

The sub-objectives of this study are:

3. To determine the suitable beam data set for AAA version 8.6 algorithm for accurate IMRT dose calculation.

CHAPTER III

LITERATURE REVIEWS

The intent of a dose calculation algorithm is to predict the dose to any point within a patient with as much accuracy as possible. However, the interactions of radiation in human tissues are quite complex and the treatment planning need the practically rapid calculation times. Thus, the inherent limitation from using the approximations on the calculation algorithms was affected on the accuracy of dose delivered to the patient. To validate the calculation algorithm, the TPS beam commissioning which included the verification process to verify the accuracy of the computed dose was performed. Many different approaches have been proposed to investigate the accuracy and precision of the dose calculation algorithms on the commercial TPS [8, 13, 14, 17]. Generally, most of the algorithms are accurate in condition of homogeneous medium and simple geometry. But in the presence of inhomogeneity and complex dose delivery pattern, the ability of the TPS to predict the accurate dose is very challenge.

3.1 Lack of charge particle equilibrium in IMRT

The use of small fields has increased substantially in advance radiotherapy technique such as the stereotactic radiosurgery (SRS) with high-resolution multileaf collimator, SRS with the Gammaknife, SRS with the Cyberknife and special radiation treatment as IMRT.

Both the step and shoot or Dynamic IMRT technique uses a series of different MLC configuration create the small field apertures for modulation of the dose. The non-equilibrium condition found on these small fields will associate with the dosimetric uncertainly due to the lack of charged particle equilibrium (CPE). Moreover, the penumbra region of the subfields will exhibit in combination of the physical penumbra from the linac's finite x-ray source size. The physical size of

radiation detectors also becomes important if the size of the detector is comparable with the field dimension from a consequence of electronic disequilibrium. The selection and proper use of a wide range of radiation detectors for the small field dosimetry have been investigated and addressed by many studies [14, 15, 18].

Juan et al. [19] had compared the IMRT absolute dose and isodose distribution obtained from the TPS calculation with the measurement dose. The study was performed with 15 MV photon from Siemens Mevatron Primus linear accelerator and the optimization and calculation algorithm from the MDS Nordion TMS treatment planning system version 5.1B. In the point dose assessment, PTW31002 ionization chamber with a volume of 0.125 cm^3 was placed at low gradient points in clinical cases and radiographic films were used to obtain the relative dose distributions.

IMRT treatment plans from five pelvic tumors cases were investigated. All cases consist of five and seven gantry positions. The numbers of segments on each case are 36, 34, 44, 65 and 28, respectively. The treatment fields contain some small size segments while the enclosed segments are 7×11 , 8×10 , 17×15 , 14×18 and $5 \times 7 \text{ cm}^2$, respectively. Effect from the transmission head scatter and small segment output factors modeling was examined, by only the first two clinical cases were included the transmission factor for the dose calculation. The output factors on several small fields, with the area $< 9 \text{ cm}^2$, were as well compared between the TPS calculation and the measured dose using the Scanditronix stereotactic diode with a 0.6 mm diameter as the detector.

The result showed discrepancy between the calculated and measured absolute dose on the cases included the transmission factor on the beam modeling, were 5.8% and 6.75%, respectively. The deviations were observed to be improved on the plans calculated without correction for transmission factor. By percent difference on the case number 3, 4 and 5 were 2.825%, 1.267% and 5.2% respectively.

Each IMRT field segmentation has a difference of the MLC position. But in the final dose calculation, the TMS treatment planning considered the jaws to be at a fixed position in the smallest opening that expose of all segments. This leads to a difference in the transmission of the primary x-ray fluence and the dose deviation will be greater on those fields which much smaller than the others. The part of uncertainty could be related from incorrect modeling of the output factors on the small segment

fields. The comparison of the calculated and measured output factors in small fields showed the overestimated values from the TPS, by 5% up to 13%. The study pointed that the correct modeling of scatter and transmission factor as well as small field output factors are important for the accuracy of IMRT dose calculation. The overall error which found in clinical cases is 1% up to 7%.

Sohn et al. [20] had investigated the output and beam shape of small fields from commercial treatment planning system, which using the acquired beam data from relatively large fields (4×4 - 4×40 cm²) for commissioning. In the study, they had compared the shapes of penumbra, percent depth-dose (PDD) and output factor of various small beamlets, in the dimension of 0.5×0.5 to 6×6 cm² with 1 cm² increment, calculated from the finite size pencil beam (FSPB) dose calculation algorithm with the measurements. They used the radiochromic films to measure the dose distributions and analyzed the optical density distribution with Matlab software. The evaluation was performed using the gamma quantity (γ), 2 mm distance and 2% dose-difference, with 0.1×0.1 mm² pixel grids size for the comparison.

The results from the study showed that the FSPB accurately modeled the depth doses and central-axis outputs at depths deeper than 2 cm. This was in contrast with the dose distributions at the build-up and penumbra regions, of the field size $\leq 2 \times 2$ cm², which were not accurately modeled. With the criteria of 2 mm. and 2% dose difference, FSPB presented the accurate prediction of penumbra. They as well observed that for the single small beams, the compared dose distributions passed the gamma index criteria. But for the clinical appropriateness of this criteria, for a composite IMRT plan, may be not clear.

Cheng et al. [21] had studied the insufficient lateral buildup of the small beamlets from step and shoot IMRT technique and their effect on dose accuracy. By the relative output factor as a function of field dimension, depth and energy was examined. Dose measurements using a 0.015 cm³ PinPoint ion chamber at the central axis at depth of maximum dose (1.5 cm of 6 MV and 3.0 cm of 15 MV) and depth at 5 cm and 10 cm on the field sizes in the range of 2×2 to 12×12 cm² were performed. Then two different lateral buildup thickness, 1 and 3 cm were investigated as illustrated in figure 3.1. By maintaining the stationary leaves (X2) at 1 and 3 cm position from the chamber axis and varying the opposite leaves (X1) in the range 1-11

cm sequentially, to produce the field width of 2-12 cm. The field lengths defined by the set of upper collimator jaws (Y) were as well varied symmetrically over the range 2-10 cm.

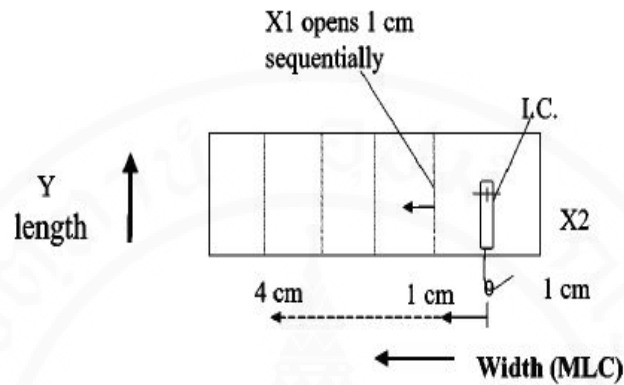


Figure 3.1 A diagram illustrated the different lateral build up field configuration for the relative output measurement using ion chamber.

Then, machine outputs of these various field configurations, normalized by the charge collected in $10 \times 10 \text{ cm}^2$, were collected and compared with those obtained from the machine commissioning for both 6 and 15 MV photon, which the output factors were collected using a diode detector in the symmetric collimator setting at depth of d_{max} . The effect of insufficient buildup on absolute dose measurement in step-and-shoot IMRT plan was as well examined. A five-field IMRT plan with five segments per field using 15 MV delivered dose 180 cGy to the isocenter was measured using a Farmer chamber in solid water phantom. The measurements were repeated four times with each phantom rotated 90° .

The results showed that, in 6 MV photon beam, the output factor measured on the field size $2 \times 2 \text{ cm}^2$ ($X1 = 1 \text{ cm}$, $X2 = 1 \text{ cm}$; $Y = 2 \text{ cm}$) at d_{max} is lower than the others about 6-10% and smaller than 10% at depth 10 cm. At the given beam length, if the field widths increased by X1 leaves, then the output factor will be increased slowly over the range of 3-7%. On the other hand, at the constant field width, the output factor will be increased over a large range of 9-14% depend on the field length. The results explained more scatter contribution from both the cephalic and caudal directions were found from the increased field length and the lateral build up distance

increases with depth. Results in 15 MV were found to be similar as 6 MV, with more variation was observed.

About the output factor, measured in the asymmetric collimator setting, when compared to those obtained during commissioning process with symmetric field, was found to be less than the calculated ones. The result shows the effect of insufficient lateral buildup in at least one direction affect the machine output. It was found that, the output factors from asymmetric field with 1 cm lateral buildup in X2 direction and Y=2 cm (in the range of equivalent square field $2\times 2-4\times 4\text{ cm}^2$), in 6 and 15 MV, were 5-7% and 5-10% less than those from the symmetric jaw respectively.

For clinical example, the variation of dose determined most occur in the segments that have less 1 cm buildup at least two edges and use the small MU. There is a 7% difference between the lowest and the highest dosed measured for the four orientations. It is evident that the calculated dose in the segments using commissioning data may be underestimated depending on energy and the segments size.

3.2 Anisotropic Analytical Algorithm verification

Anisotropic Analytical Algorithm (AAA) is a three dimensional (3D) pencil beam convolution/superposition algorithm which uses Monte Carlo derived kernels. The principle is dose deposition come from two photon sources (primary and secondary) and electron contamination source which all detail was shown in appendix A. Performance of AAA algorithm from the basis tests to clinical condition was examined by several studies.

Fogliata et al [22] had investigated the AAA for three photon beams, 6 MV of a Varian 6EX and 6&15 MV from a Varian 2100C/D linear accelerator. They performed measurements in water phantom, using 0.125 cm^3 ionization chamber for relative measurements and PTW-LA48 ion chamber array for the enhanced dynamic wedges. The results showed, the AAA calculations with 2.5 mm grid size, presented an excellent agreement between the calculated and measured dose in all situations. The PDD and transverse profiles curves contained the maximum deviation, smaller than 1% or 1 mm, for both the open and wedged fields. Only the small wedge field ($3\times 3\text{ cm}^2$) which the deviation can be observed at 3%. The computed OF and wedge

transmission factors in the symmetric collimator were found very close to the measured data. In the asymmetric and MLC defined field, average percentage difference are smaller than 1.5% with the range is within $\pm 2\%$ for all cases.

Next step for AAA accuracy test was studied by Bragg et al [23, 24]. They performed an investigation in the homogeneous and inhomogeneous media, as well as in the simulated lung plan and IMRT dose distribution calculation

The measurements in the uniform medium, showed the good consensus between the calculation and measurement, within 2% dose difference or 2 mm DTA, of all beam profiles and percentage depth doses (PDD) both in the simple and complex geometries, by most points of the calculated dose were less than the measurements. In the inhomogeneous condition, measurements in solid water phantom which consisted of bone and lung equivalent block, the point dose and depth dose calculations showed the overall uncertainty within 2.5% from the measurements. Two simulated lung plans, calculated with AAA version 7.5.18 with 2.5 mm calculation grid in the semi-anthropomorphic phantom, were determined an accuracy of dose prediction by using the pinpoint chamber measured at various locations. The dose deviation within 2.5% can be seen, except for two points near the field edge in the high dose gradient region.

For dose distribution calculation in IMRT plan, the prostate, parotid, nasopharynx and lung IMRT plans using 6 MV were transferred to three semi-anthropomorphic phantoms (pelvic, head and neck and thorax region) and recalculated using AAA with inhomogeneity corrections and 2.5 mm grid size. The PTW 31016 pinpoint chamber has been used to measure the dose at 3 to 6 locations in each phantom, and the results showed the excellent agreement between the calculation and measurement in the prostate and parotid plans with no discrepancy exceeding 3% or 1.6 mm DTA. But in the lung and nasopharynx plans, the agreement was slightly worse by the maximum discrepancies was seen at 3% or 3.5 mm.

The study of Van Esch et al [25] had also reported the accuracy and limitations of the analytical anisotropic algorithm (AAA) dose calculation in Eclipse treatment planning system. The investigation contained two parts: the acceptance testing of dose calculation algorithm and inhomogeneity tests. For the acceptance testing, the relative point doses were measured in water phantom using NE 2571 thimble chamber and films or 2D ion chamber array in solid water phantom for planar

measurements. These tests were performed in open fields, wedge fields (reference and non-reference condition) and IMRT fields. Dosimetric validation was evaluated by comparing agreement between the calculated and measured profiles, depth dose curves and output factors on 6 and 18 MV photon beams. For inhomogeneity tests, all profiles and depth dose curves measurements were performed in slab phantom that consist of solid water plates and cork (lung) slab. The clinical situation was simulated in the humanoid phantom that comprise with tissue, bone and lung equivalent materials using ionization chamber to measure in the right and left lung and at the isocenter on 6 and 15 MV.

The results showed the AAA algorithm is excellent for calculating doses in the basic beam data of 6 and 18 MV. In non-reference condition, the calculated profile and depth dose curves of two half-beams show only a slight underestimate of the dose around 0.5%. The monitor unit calculation shows a trend to underestimate the dose and the agreement is better in high energy photon (average 1.91% in 6 MV and 1.17% in 18 MV). The absolute dose comparison in all asymmetric fields using physical and enhance dynamic wedges (EDW) show a good correspondence on the beam axis is within 0.5%. In asymmetric fields, the agreement of the profiles is excellent in both wedges. The deviation of absolute dose compare with physical wedge is up to 4% at the center of the field are involving the main collimator overtravel. The measured and calculated depth dose curves showed an agreement within 1%, and 1 mm of the depth below d_{\max} . At build-up region, the discrepancies were found to be increased at the smaller source-to-phantom distance. For the IMRT field, calculated depth dose curves below d_{\max} showed good agreement with the measurement within 1% dose difference and 1 mm DTA, but all the deviations still be observed about 2.5% at d_{\max} .

In the inhomogeneities test, AAA shows good conformity profiles versus the film measurement which a smooth transition at the solid water and cork interface. For the depth dose comparison, AAA shows the underestimate dose in the cork. This underestimate dose is up to 7% in the smallest field size. In Anthropomorphic measurement, AAA will underestimate the dose in lung but show the overestimate dose at isocenter by 3% for 6 and 15 MV.

The performance of AAA version 6.5 commissioned with golden beam data was studied by Karen Breitman et al [26]. By comparison of the measured and calculated relative doses, absolute doses with the measurements in anthropomorphic phantom in two institutions using 6 and 15 MV photon beams on Varian 21EX linear accelerator was undertaken. Using multiple test cases, including open square and rectangular fields, extended SSD (125 cm), wedge fields, Cerrobend-blocked field, oblique incidence, asymmetric half-beam and MLC fields, relative dose comparisons were carried out in water using Wellhofer scanning system and CC13 ion chamber at four different depths. Comparative evaluation used the point passing criteria that obtained the tolerance from TG-53 in inner, penumbra, outer and buildup beam region. For MU calculation accuracy test, the absolute doses were compared with the measurements in the same test cases. The ratio of validate value is defined to be the total scatter factors difference (Δ TSF) which is a percent difference between the measured (TSF_{measured}) and AAA-calculated (TSF_{AAA}).

About the anthropomorphic phantom measurement, it was used to evaluate the accuracy of dose calculation in inhomogeneous media. At the first department, the study was performed in simulated human thoracic, CIRS phantom using Pinpoint ion chamber for the dose measurement in 6 and 15 MV. In the second department, TLD measurements were performed in two section of Alderson Rando anthropomorphic phantom. The thorax section, 12 measurement points were inserted in the central-axis of this section that used anterior beam of 15 MV. In neck section, 6 TLDs were inserted in the center slice of neck section and 2 TLDs inserted in next superior slice that used 6 MV of lateral beam.

In the relative dose comparison from all 700 profiles, the 90% of profiles that calculated by AAA passing the criteria in both institution. The inaccuracy of calculation was found at depth near the buildup region and the penumbra modeling. For calculated absolute dose verification, mean value of calculated TSF is slightly lower than the measurement, about 0.2% to 0.4%. The difference of point dose measurement in inhomogeneous phantom show the calculation is slightly higher than the measurement. The mean discrepancy in thorax phantom is -2.2% with a maximum of -5.2% and -1.6% with a maximum -5.3% in the neck section. The result show all

differences between the measured and calculated are pass the 7% criteria that recommended by TG-53.

The accuracy of AAA algorithm for predicting dose at tissue interface in stereotactic radiotherapy of nasopharyngeal carcinoma was investigated by Kan et al [27]. They had measured the central axis depth dose of the small fields in solid phantom containing two different sizes of rectangular air cavities, $5 \times 5 \times 30 \text{ cm}^3$ and $3 \times 3 \times 30 \text{ cm}^3$, using Markus parallel plate ion chamber and TLD-100 chips, respectively. Proximal and distal interface dose were as well to be examined by thin TLDs and radiochromic films to assess the dose discrepancy between calculation and measurement. For lateral profiles, they were measured at the distal interface, 1 and 3 mm beyond the air cavity using the radiochromic films in 2×2 to $5 \times 5 \text{ cm}^2$ fields. To evaluate accuracy of dose at air-tissue interface in clinical situation, six intensity-modulated stereotactic radiotherapy (IMST) boost plans of nasopharyngeal region using TLD-100 chips to measure dose at five points in the air-tissue interfaces of nasal and oral cavity were performed in anthropomorphic phantom. All dose calculations were performed with AAA version 8.6, with grid size of 2.5 mm and heterogeneous correction from CT number of the materials.

Result of AAA calculation in single small field in rectangular air cavity phantom, the overestimated central axis dose at and beyond the first few millimeters of the air-water interface was found. The overestimate predict of algorithm was seen to be more severe in decreasing field sizes and the larger air cavity at the distal interface. Calculated interface dose was detected to be three times more of the measurement dose in $2 \times 2 \text{ cm}^2$ field. About the lateral profiles, at the central dose, the measured doses were much lower than those predicted by the algorithm, while the doses outside the field edge were seen higher than the calculation. This must be from the increased lateral range of secondary electrons travelling through the air cavity. In the anthropomorphic interface measurements, the mean errors of the five points comparison between the calculation and the TLD measurement ranged from 1.1% to 4% with the maximum overestimation was 8.3% that occurred in interface region of oral cavity.

CHAPTER IV

MATERIALS AND METHODS

4.1 Materials

4.1.1 Beam scanning systems

As shown in figure 4.1, relative beam data needed in the commissioning for this study were collected using the Blue phantom scanning system (Scanditronix-Wellofer Dosimetric, Schwarzenbruck, Germany). The system is composed of the control unit (CU500E), water phantom with three-dimension servo and an optional chamber array. The phantom is an acrylic plastic (Perspex) water tank with $480 \times 480 \times 410 \text{ mm}^3$ scanning volume. The CU500E combines the controller and two independent integrated electrometers. To acquire the beam data, scanning parameters and sequences including the analysis were operated under the OmniPro-Accept 6.1 software. The scanning position accuracy and reproducibility is within $\pm 0.5 \text{ mm}$ and $\pm 0.1 \text{ mm}$, respectively. A variety of detectors including cylindrical and parallel plate ionization chambers as well as diode semiconductors can be selected to meet the specific requirement of the measurement. With this system, the data acquisitions and analysis have been done with high spatial resolution [27].



Figure 4.1 Scanditronix-Wellhofer Blue phantom dosimetry systems

4.1.2 Water phantom tank

The acrylic wall 9.525 mm thick and $38 \times 38 \times 38 \text{ cm}^3$ in size of MT-150 water phantom tank is manufactured by MED-TECH Company that present in figure 4.2. It was used to perform the output factor measurements in this study. The crank-operated depth positioning allows the depth of measurement can be adjusted in 0.1 mm step and the total vertical travel is 25 cm. The probe holder is available with several chamber types such as micro chamber, ion chamber or parallel plate chamber [28].



Figure 4.2 MT-150 water phantom

4.1.3 Detectors

Two types of ionization chamber and diode detector were used to collect beam data in this study.

4.1.3.1 Farmer ionization chamber

A Farmer thimble 0.6 cc (NE2571) ionization chamber (Nuclear Enterprises, Fairfield, New Jersey, USA) with aluminum electrode in figure 4.3 (a) was used in the measurement. The sensitive volume for this chamber is 0.69 cm^3 with 24.1 mm length and the graphite wall is 0.36 mm thickness [29].

4.1.3.2 Pinpoint ionization chamber

Pinpoint chamber type 31014 (PTW, Freiburg, Germany) is a waterproof ion chamber with 0.015 cm^3 nominal sensitive volume. The chamber wall consists of acrylic (PMMA) 0.57 mm thickness and 0.09 mm of graphite material and the aluminum electrode. The chamber is designed for acquisition of the small photon

beam dosimetry in the energy range of 1.25 MV up to 50 MV with a long-term stability ($\leq 1\%$ per year), as shown in figure 4.3 (b) [30].

4.1.3.3 Stereotactic field detector (SFD)

The SFD diode field detector (Scanditronix Wellhofer, IBA Dosimetry, Schwarzenbruck, Germany) in figure 4.3 (c) is a p-type silicon detector chip which is designed to measure the radiation dose on the field size range from 10×10 cm down to 2 mm diameter with high spatial resolution. The diameter of an active area is 0.6 mm and thickness of active volume is 0.06 mm. This detector was used for the depth dose, beam profile and output factor measurements in small photon beams [31].

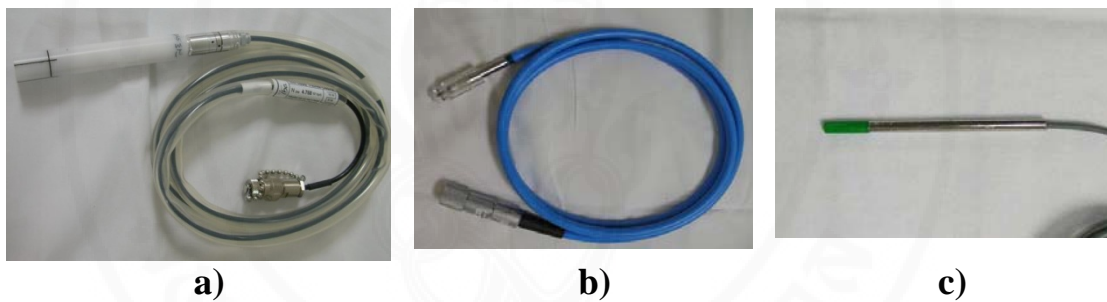


Figure 4.3 Farmer chamber (a), Pinpoint chamber (b) and Diode detector (c)

4.1.4 Electrometer

DOSE1 (IBA Dosimetry, Schwarzenbruck, Germany) in figure 4.4 is a high-precision electrometer which can be used with the ionization chamber and semiconductor for absorbed dose measurements. The measuring quantities and units can be displayed in several integrate of Gy, Sv, R, rad and rem. There are two measuring modes, charge mode (dose) with the range from 40pC to 1.0C at 0.1pC resolution and current mode (dose rate) with range from 40pA to 1000nA at 0.1pA resolution [32].



Figure 4.4 Electrometer DOSE1 from IBA dosimetry

4.1.5 Varian Clinac 23EX linear accelerator

Varian Clinac 23EX linear accelerator (Varian, Palo Alto, USA) in figure 4.5 provide dual photon beam energies of 6 and 10 MV and six electron beam energies of 6, 9, 12, 15, 18 and 22 MeV, respectively. The 120-leaf MLC, with eighty leaves contain 0.5 cm leaf width and 1 cm width for the others were equipped to the machine. All leaves are moving parallel with the x-jaw direction and working cooperate with the backup jaw. This machine offers the dynamic movement of the multileaf collimator to provide an efficient method of delivering IMRT. 6 MV photon beam was used in the head and neck IMRT treatment planning in this study [33].



Figure 4.5 Varian Clinac 23 EX linear accelerator

4.1.6 Eclipse™ treatment planning system

Eclipse™ TPS (Varian, Palo Alto, USA) is a Windows® based operating system. It consists of the virtual simulation tools which include the organ contouring, multimodality imaging and automatic field positioning. The photon dose distribution will be generated using the Anisotropic Analytical Algorithm (AAA) version 8.6 which is the 3D pencil beam convolution/superposition algorithm [34].

4.1.7 Anderson radiation therapy phantom (ART)

ART phantom (Radiology support devices, Long Beach, USA) was constructed with a natural human skeletons, soft-tissue and lung simulating material. The skeletons conform closely to the standards of ICRU report No.44 and lung materials are modeled from syntactic foam with a specific gravity of 0.30 g/cc. ART is transected horizontally into 2.5 cm thick slice which contains holes for In vivo dosimetry by TLD. Dosimetry holes spacing are drilled in grids 1.5 cm × 1.5 cm with 7 mm holes diameters as shown in figure 4.6 [35].



Figure 4.6 Anthropomorphic phantom: Anderson radiation therapy phantom (ART)

4.1.8 CT Simulators

The Brilliance, Big Bore CT 16-slice (Philips, Andover, USA) display in figure 4.7 is a spiral computed tomography system which provides the cross-sectional imaging for radiation therapy planning. The gantry aperture is 85 cm diameter that support for scanning patients with immobilization devices. The true size scan field of

view is 60 cm. and the scan rotation time can be selected in the range between 0.44 to 2.0 sec. The 16-slice detector is covering 2.4 cm for data acquisition [36].



Figure 4.7 Brilliance Computed Tomography 16-slice machine

4.1.9 Thermoluminescence Dosimetry (TLD) system

4.1.9.1 Thermoluminescent Dosimeter (TLD-100)

The thermoluminescent dosimeters (TLD-100), rod type, $1 \times 1 \times 6 \text{ mm}^3$ in size were used for point dose measurement in the humanoid phantom in this study. The dosimeter is lithium fluoride (LiF) crystals doped with magnesium and titanium (LiF: Mg, Ti) with the density is of 2.64 g/cm^3 that is nearly tissue equivalent. The operating dose measurement range is between 10 pGy to 10 Gy. They were manufactured by Thermo Scientific Inc (Erlangen, Germany). This material should be handling by vacuum tweezers or plastic forceps because the small scratches and loss of mass deposit dose affect in light emission [37]. The TLD materials and vacuum tweezers set were shown in figure 4.8.

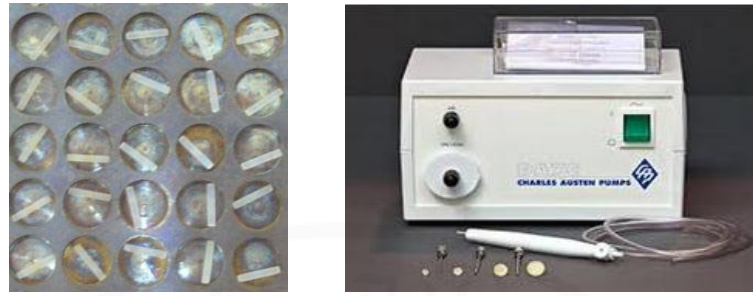


Figure 4.8 Thermoluminescence dosimeters (TLD-100) rod and vacuum tweezers set

4.1.9.2 Thermoluminescence reader

The system of Harshaw 5500 TLD Reader (Thermo Scientific Inc, Erlangen, Germany) shown in figure 4.9 contain a linear, programmable heating system and a photomultiplier tube for measurement of the TL light output. It can be used with rod, chip or disc shape of TLD and automatic operation for up to 50 dosimeters in a single loading. The heating profiles included pre-heat, acquire and anneal cycles which operated with the hot nitrogen gas (N_2) heating system. The suitable energy for the photon dose measurement is >5 keV with $10 \mu\text{Gy}$ to 1Gy range of linear response [38].



Figure 4.9 Harshaw model 5500 TLD reader

4.1.9.3 Thermoluminescence annealing oven

The TLD annealing oven (PTW, Freiburg, Germany) has two predefined standard temperature programs, preheating and annealing. In the heating

cycle, the hot air stream is circulated throughout by built-in fan that makes the equal temperature distribution in the oven volume. TLD elements can be annealed with the maximum temperature 400°C and a safety circuit prevents heating to temperatures above 450 °C. The actual temperature was shown in a digital display by built-in lamps indicate the program progress [39]. The oven and accessories are showing in figure 4.10.



Figure 4.10 TLDO annealing oven

4.1.10 Diode array for IMRT QA

MapCHECK2™ (Sun Nuclear, Melbourne, USA) in figure 4.11(a) is a widely used, two-dimensional (2D) detector arrays for IMRT verification. It contains 1527 diode detectors arranged with 7.07 mm grid spacing on the area of 32×26 cm². The active volume of detector is 0.000019 cm³ that can be used in the small and intensity modulated fields. The sensitivity variation of detector is less than 0.5%/kGy at 6MV photon and is pressure independent. The radiation measurement range for the photon is between 1.25 MV to 25 MV. For IMRT QA process, MapCHECK2™ detector arrays was used with MapPHAN™ (Sun Nuclear, Melbourne, USA) which is a water equivalent phantom , 35×38 cm² in size as shown in figure 4.11 (b) [40].



Figure 4.11 MapCHECK2™ (a) and MapPHAN™ (b)

4.2 Methods

Three main procedures included collection of the small field beam data, beam entry and verification of configured beam data were performed for the AAA 8.6 algorithm on the Eclipse treatment planning system.

4.2.1 Collection of the small field beam data and beam configuration

According to the Beam Configuration Reference Guide of the Eclipse application software, commissioning the AAA 8.6 algorithm for 6 MV photon beams required specific measured beam and machine data of the linear accelerator. The required beam data consist of the open and wedge fields depth doses, beam profiles and output factors. For open fields, the mandatory depth doses were measured on 4×4, 6×6, 10×10, 20×20 cm² and the largest field size at central axis of the beam. The additional data was recommended to measure on 8×8, 30×30 cm² and the smallest field size. The cross plane profiles were scanned at five depths (d_{max} , 5, 10, 20 and 30 cm) in the same set of field size. Output factors were as well collected at depth 5 or 10 cm depend on beam energy, in the series of width and height [35]. All measurement data were processed and converted to proper format before transferring to the planning system for configuration step.

4.2.1.1 Measurements of the small field beam data

At Division of Radiation Oncology, Siriraj hospital, the routine measurement data to validate AAA 8.6 algorithm is the beam dataset of 3×3-40×40

cm² field size. To investigate an effect of small field dosimetry (field size smaller than 3×3 cm²) on accuracy of IMRT dose calculation, beam data of the field size 1×1 and 2×2 cm² on 6 MV photon from Varian Clinac 23EX linear accelerator were additional collected and configured to the Eclipse TPS.

i. Measurement of the small field depth doses

Measurements of the depth dose for field size 1×1 and 2×2 cm² were performed at 100 cm SSD with the stereotactic diode detector and Blue phantom scanning system. The collection method is step by step with 2.5 mm step. The collected value at given depth were normalized to the depth of dose maximum (d_{max}) which is 1.6 cm for 6 MV photon in this study. All 120 data points were obtained at water surface until 30 cm depth as shown in Figure 4.1.

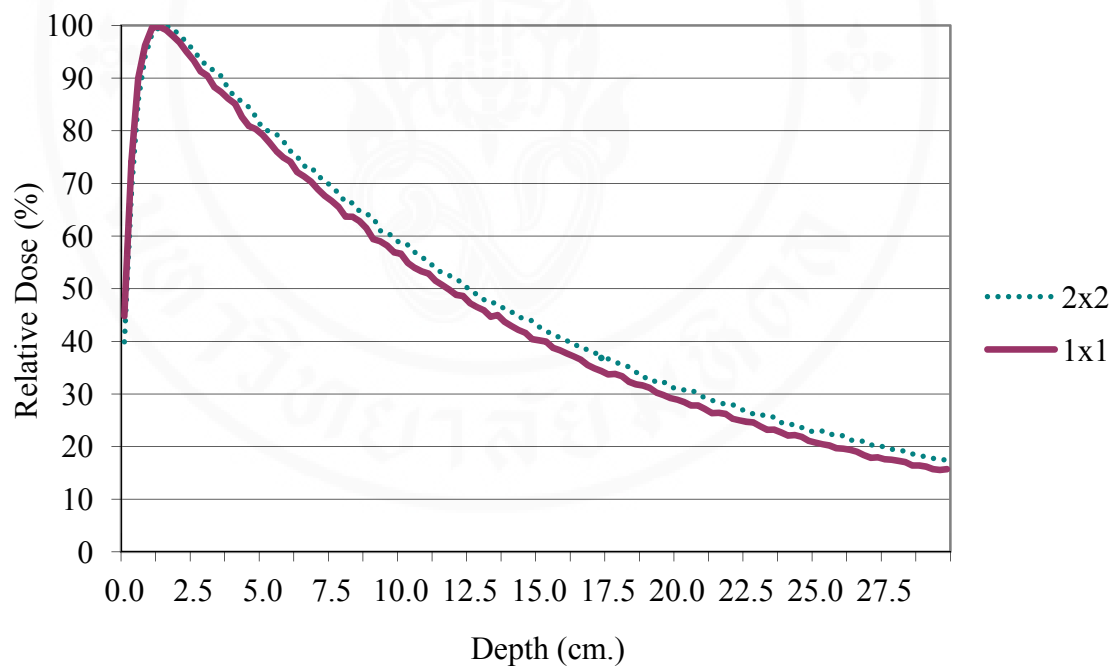


Figure 4.12 The 6 MV photon depth dose curve for field size 1×1 and 2×2 cm²

ii. Measurement of cross plane beam profiles

Cross plane beam profiles, at five depths (d_{max} , 5, 10, 20 and 30 cm) on field size 1×1 and 2×2 cm² of 6 MV photon was also measured using diode detector in water phantom. Figure 4.2 and 4.3 shows the profiles at various depths on field size 1×1 and 2×2 cm² fields, respectively.

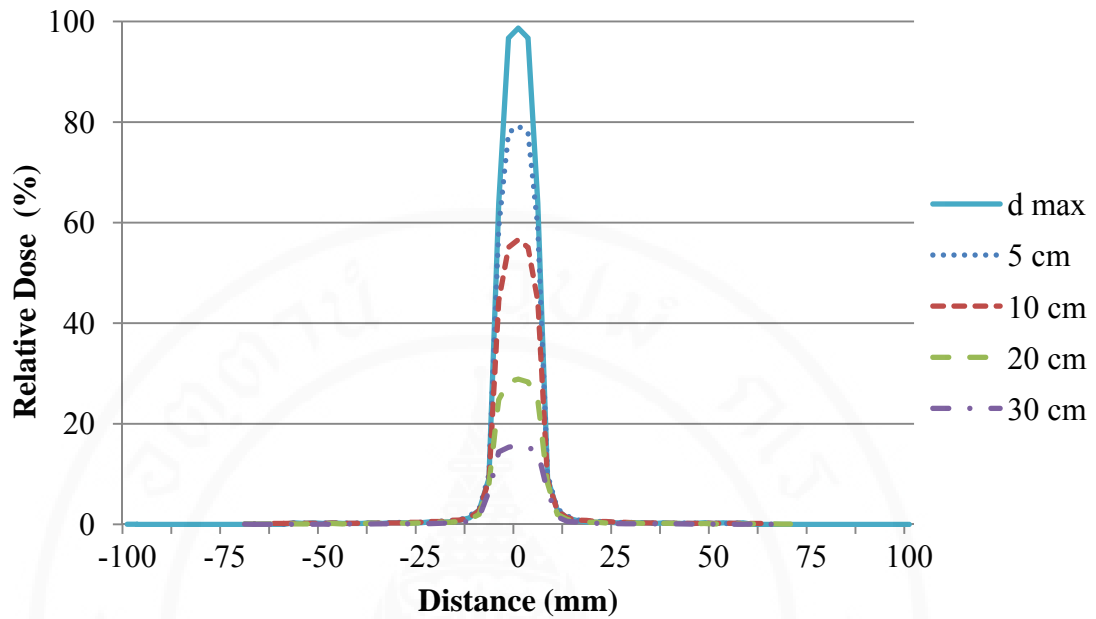


Figure 4.13 The x-plane profile of $1 \times 1 \text{ cm}^2$ field at d_m , 5, 10, 20 and 30 cm depth.

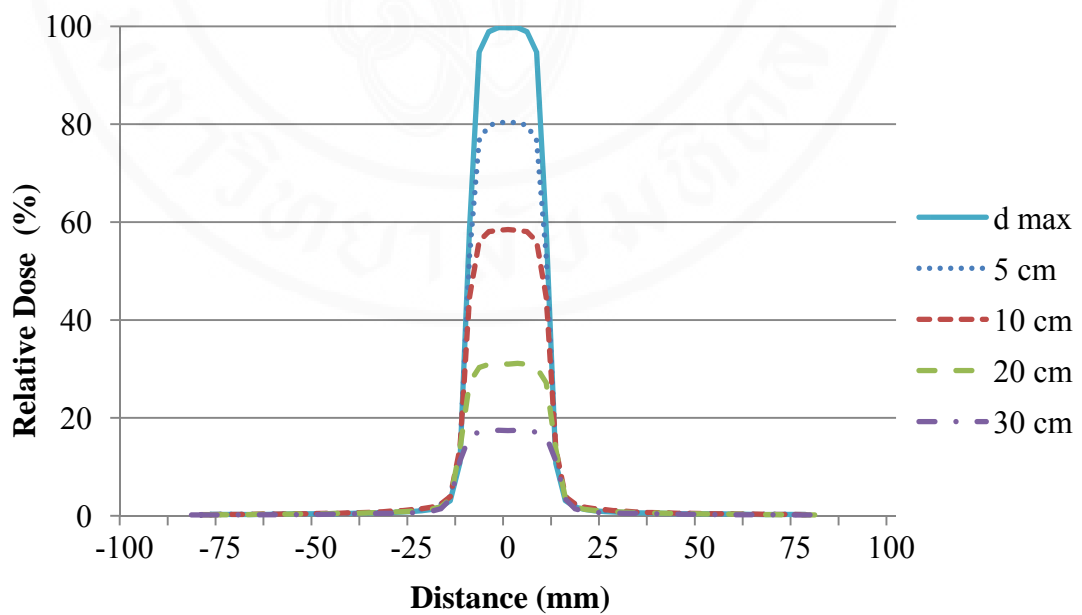


Figure 4.14 The x-plane profile of $2 \times 2 \text{ cm}^2$ field at d_m , 5, 10, 20 and 30 cm depth.

iii. Measurement of the output factors

The output factor (OF) of 6 MV photon was measured in small and rectangular fields at 10 cm depth using Pinpoint chamber. The measurements were

performed on a series of the field width (X) and field length (Y), when X or Y jaw was kept to be 1 and 2 cm, as illustrated in Table 4.1

Table 4.1 The required field sizes of small and rectangular fields for output factors measurement

Field size		OF	Field size		OF	Field size		OF	Field size		OF
X	Y		X	Y		Y	X		Y	X	
1	1		2	1		1	1		2	1	
	2			2			2			2	
	3			3			3			3	
	4			4			4			4	
	5			5			5			5	
	6			6			6			6	
	8			8			8			8	
	10			10			10			10	
	12			12			12			12	
	15			15			15			15	
	20			20			20			20	
	30			30			30			30	
	35			35			35			35	
40		40		40		40					

4.2.1.2 TPS beam configuration

All the collected beam data were converted into ASCII files format and grouped into three sets. Each group contained the specific beam data needed for beam configuration process. This data set was consisting of the depth dose, cross plan beam profiles and output factor by

1. Beam dataset of the field size from 1×1 to 40×40 cm²
2. Beam dataset of the field size from 2×2 to 40×40 cm²
3. Beam dataset of the field size from 3×3 to 40×40 cm²

4.2.2 Beam data verification

Basic beam data measured that required by the dose calculation algorithm can be used directly as input to the beam data library. After beam data was imported into the treatment planning system. The TPS was required the QA process to determine the accuracy of the calculation. The performance verification is analyzed

by criteria for acceptability of the calculated and measured comparison. That result demonstrates the calculation is working correctly. The accurately predict the depth dose, cross plan profile and absolute dose calculation in this study were done in open field of 1×1, 2×2, 3×3 and 10×10 cm² basic situations. The measured data were compared with the calculated data that calculated with three beam data set. The acceptance criteria are usually displayed as a combination of dose deviation and distance to agreement (DTA) in a geometrical concept, low and high dose gradient region. The deviations (δ) described above refer to comparisons of individual calculated and measured points. These values can be expressed as a percentage of the locally measured dose according the equation below.

$$\text{Deviation } (\delta) = 100 \times \frac{(D_{\text{calc}} - D_{\text{meas}})}{D_{\text{meas}}} \quad (1)$$

Where D_{meas} is the measured dose

D_{calc} is the calculated dose at the same point

The DTA was defined as the distance between a reference data point and the nearest point with the same dose value in the calculated distribution. The criteria of acceptability for δ should be according to Venselaar et al [42] and the task group 53 of AAPM report [13] that shown in Table 4.2.

Table 4.2 Proposed values of the tolerances for δ for application in different test configuration [42]

Tolerance	Homogeneous, simple geometry
δ_1 (central beam axis data)	2%
δ_2 (build-up region of central beam data)	2 mm or 10%
δ_3 (outside central beam axis region)	3%
δ_4 (outside beam edges)	3%
RW ₅₀ (radiological width)	2 mm
δ_{50-90} (beam fring)	2 mm

For the accurately predict the depth dose, the evaluation were compared the consistency of the data point on the central axis (δ_1) and the data in the build-up region (δ_2). δ_1 is defining the data beyond the depth of d_{max} in the high dose and small dose gradient region. For δ_2 , the comparison was separated in to two parts that $\delta_2(a)$ was specified the difference in the depth at the 90% isodose. $\delta_2(b)$ was defined the accordance of the data points in the high dose and large dose regions. For the cross plan profile verification, there were compared of the consistency in four criteria. First, the data points outside beam axis beyond d_{max} (δ_3) are in a high dose and small dose gradient region. Second, the data in a low dose and small dose gradient is a point off the beam edges (δ_4). Because of these criteria are applied in low dose regions where the dose calculations are usually less accurate. The equation (1) is not useful to relate deviations between calculations and measurements. An alternative is to replace expression by the equation (2) that the deviation might be related to the dose measured at a point at the same depth on the central axis.

$$Deviation (\delta) = 100 \times \frac{(D_{calc} - D_{meas})}{D_{meas,cax}} \quad (2)$$

Where $D_{meas,cax}$ is the measured dose at the central axis

Third, RW_{50} is the quantity that defined the width of a profile at half its height at the beam axis. The final criteria were compared the distance between the 50% and 90% dose in the penumbra (δ_{50-90}). The regions of validation of all criteria in depth dose and cross plan profile were shown in figure 4.15.

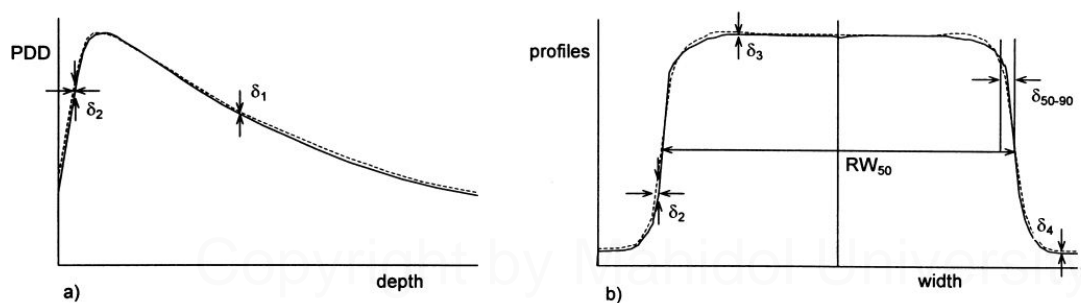


Figure 4.15 The verification criteria to compare calculated and measured depth-dose (PDD) curves (a) and cross plan profiles (b)

The performance of the system in calculating the absolute dose was validated in six open square fields. The test fields were consisting of 1×1, 2×2, 3×3, 5×5, 10×10 and 20×20 cm². The criteria for the acceptable was follow the gold of dose delivery accuracy in 5% [13]. It concludes that the accuracy of the beam calibration (2.5%), the dose calculation (3-4%) and the treatment delivery (3-4%). The Accuracy of all the calculation doses on three beam data set was verified with the measurements in water phantom using ionization chamber.

4.2.3 IMRT dose distribution calculation

Due to complex dose distribution of IMRT planning came from the superposition of dose on a number of small fields. In this study, accuracy of AAA 8.6 algorithm for IMRT dose calculation based on three groups of commissioning data will be assessed. Head and neck IMRT planning will be created on humanoid phantom and then dose distribution was calculated using each beam dataset (A, B and C). Three dose distributions from different configured beam data were compared and accuracy of the point doses will be verified using thermoluminescent dosimeters.

4.2.3.1 Generating head and neck IMRT plan

Cross sectional images of the ART (Anderson radiation therapy) phantom were acquired with a Philips Brilliance, Big Bore 16-slice CT simulator as shown in figure 4.16. These images were performed at 3 mm slice thickness from the vertex to 5 cm below the sternoclavicular notch. The phantom was in supine position with proper head support and using the laser system to mark for the reference point. Image scanning was undergone with the head and neck scan protocol at 120 kV, 300 mA and 3 mm slice thickness.

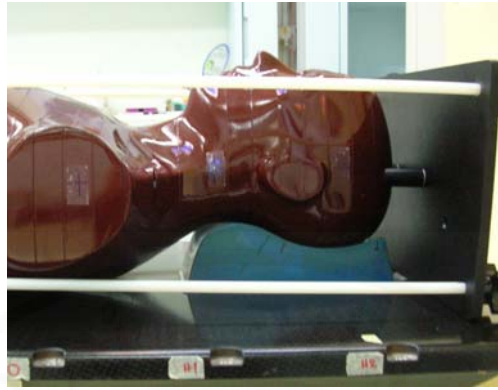


Figure 4.16 The ART phantom was scanned in CT simulation

All phantom CT images were imported to the Eclipse treatment planning system and fused with the nasopharyngeal carcinoma patient CT images. All structures delineated on the patient IMRT plan will be pasted on the phantom images and were used in the IMRT optimization process. Contouring organs of head and neck IMRT planning consist of the target volumes and the organs at risk (OARs). The Gross Tumor Volume (GTV) is defined as the gross tumor disease determined from CT images. The Clinical Target Volume (CTV) is defined as the GTV plus potential microscopic disease region that delineated by physician. The different CTVs will defined, namely CTV70 for the GTV included high risk margin of potential microscopic spread. CTV59.4 and CTV54 were designed to present intermediate and low risk disease regions, respectively. The three planning target volumes (PTV70, PTV59.4 and PTV54) were extended with 5 mm margins from CTV regions. The OARs including the brainstem, optic nerves, optic chiasm, eyes, lens, brain (temporal lobes), parotid glands, spinal cord, auditory structures, constrictor muscles, larynx, oral cavity, mandible, trachea and esophagus were contoured on axial CT images.

The seven-field, sliding window IMRT plans at gantry angles 0° , 45° , 100° , 145° , 220° , 250° and 330° was generated using 6 MV photon. The prescribed dose was set to be 70 Gy to PTV70, 59.4 Gy to PTV59.4 and 54 Gy to PTV54 in 33 fractions. For OARs, dose constraints were designed to limit the maximum does not to exceed 25 Gy for lens, 45 Gy for spinal cord, 50 Gy for eyes, 54 Gy for brainstem, optic nerves and optic chiasm, 70 Gy for brain. The mean dose was

less than 26 Gy for parotid glands, 40 Gy for oral cavity, 45 Gy for larynx and esophagus, 50 Gy for auditory structures [43]. With the same optimization, the computed dose distributions from three different beam dataset were performed using 2.5 mm calculation grid and normalization to 95% of isodose level.

4.2.3.2 Comparison and verification of the head and neck IMRT plan

All three IMRT plans as described from the previous section were compared in term of monitor unit, number of segments and segment size. For the dosimetric calculation accuracy, the point dose and dose volume histograms (DVHs) on each plan will be assessed. The planar dose distributions of IMRT plan were measured by using Sun Nuclear 2D detector arrays QA system (MapCHECK2™) and verified using gamma analysis (3% dose difference and 3 mm DTA criteria) as shown in figure 4.17.



Figure 4.17 2D dose distribution IMRT verification using MapCHECK2™ and MapPHAN™

4.2.4 Verification of the IMRT Point Dose Calculation Accuracy Using TLD-100 Dosimeters

The accuracy of IMRT dose calculation from AAA 8.6 algorithm will be assessed by performing the point dose measurements using TLD-100 dosimeters in

head and neck ART phantom and compared with the calculated dose. Measurements were performed with 6MV photon and repeated three times for each IMRT plan.

4.2.4.1 TLD measurement in ART phantom

The ART phantom is transected horizontally into 2.5 cm thick slice which contains holes for In vivo dosimetry. Holes spacing are drilled in grids $1.5 \text{ cm} \times 1.5 \text{ cm}$ with 7 mm. holes diameters which are designed to hold the TLD rods. In this investigation, the treatment field of head and neck IMRT plan covered on eight slabs of the head and neck phantom. Total numbers of sixty TLD measurement points were distributed at various locations of the phantom as shown in figure 4.18. Measured dose at the selected points from three measurements were averaged and compared to the calculation dose.

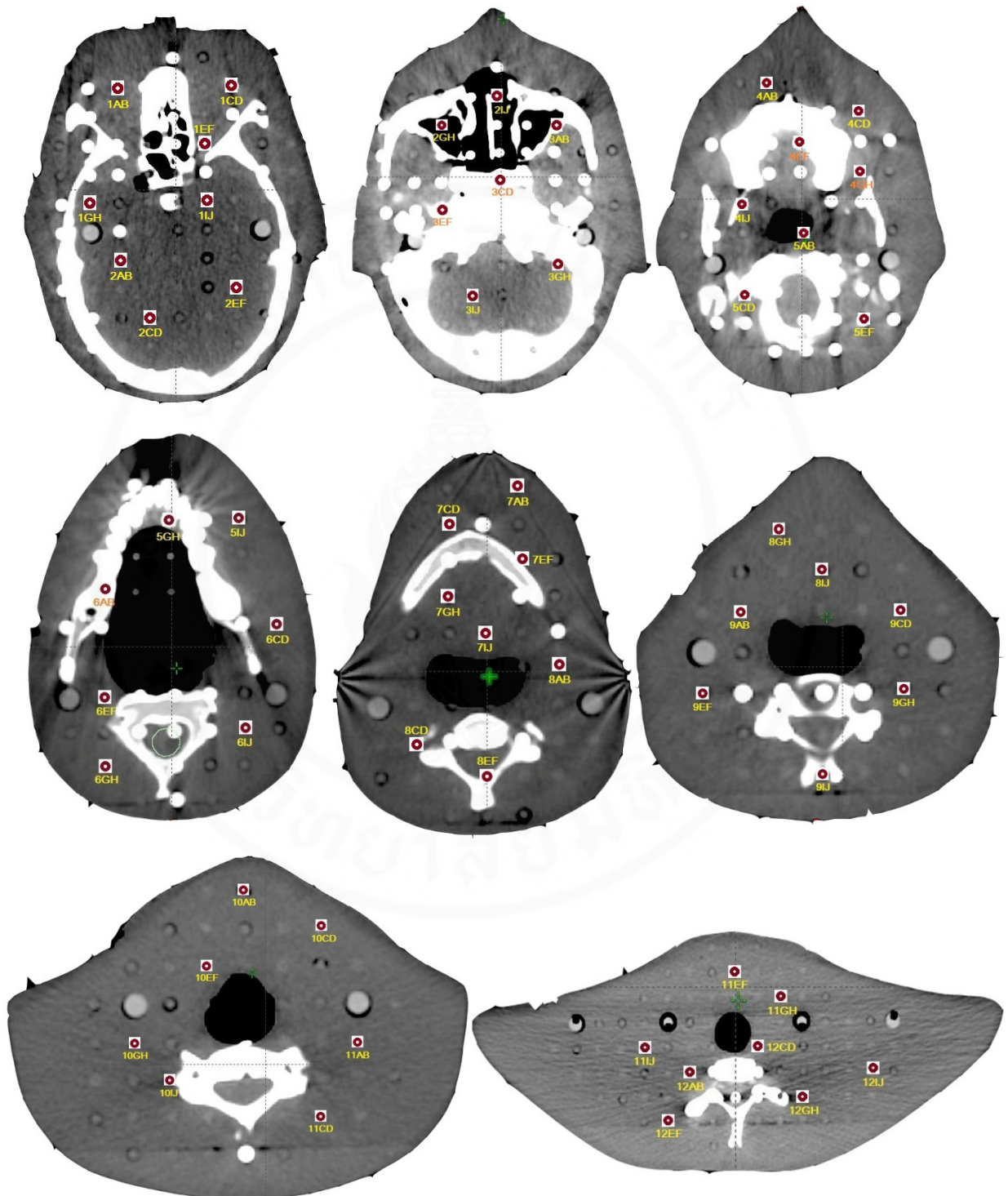


Figure 4.18 The TLD measuring points were shown in eight slabs of humanoid head and neck phantom. The number in each point represents the position of TLD.

4.2.4.2 TLD Preparation and calibration

Thermoluminescent Dosimeter (TLD) is a type of small-field dosimeter which used in radiation therapy for dose measurement and verification of dose delivery. It is used to determine radiation dose in complex geometries, to estimate the critical organs dose and used for dose measurement in small fields. Because of the TLDs have a very high sensitivity and reusable. Thus before the measurement, TLDs need to erase the residual signal and finding the calibration factor that a reduction of the uncertainties in the dose determination.

a). *TLD Preparation*

All TLDs were annealed with high temperature (400°C for 1 hour) and low temperature (100°C heating for 2 hours) without the signal reading for erase the residual signal. This process was repeated in three times. The background signal of each TLD was estimated from the average reading behind the annealing process from TLDs rod not exposed to radiation. The background signal was performed in three times and recorded the values of each dosimeter for background subtraction.

b) *TLD Calibration*

In this experiment, the individual calibration factor were investigated because of each TLD has a difference sensitivity. First procedure, the dosimeters were annealed at 400°C in 1 hour and 100°C in 2 hours for erase the remaining signal. The process of the TLD calibration was:

(i) All TLD was placed in the perspex planchet that covers with plastic of a 0.5 cm thick. The dosimeters were irradiated with known dose of Co-60 machine with the exposure time for 100 cGy. The treatment field size is 15×15 cm² with the source to surface distance 80 cm. After irradiation, the exposed TL was annealed at 100 °C for 10 minutes in pre-read annealing. Then the TL signals were recorded in nanocoulomb (nC) by the TLD reader.

(ii) After the TLDs are read-out, they are annealed in order to ensure the signal has been completely removed and the TLD is again ready for use. This process was repeated at three times and averages the signal reading.

(iii) The calibration factor (CF) of individual TLDs was calculated following the equation below:

$$\text{Individual TLD calibration factor (CF)} = \frac{\text{TL Signal (nC)}}{\text{Known Dose (cGy)}} \quad (3)$$

(iv) The coefficient of variation (CV) was used to determine the uncertainties of the measurement. %CV represents the percentage ratio of the standard deviation to the mean that it was calculated by equation below. The statistic value was used for comparing the degree of variation from one data series to another and useful even if the means are very different from each other. In this experiment, the dosimeter has a %CV more than 3% should not be used in point dose verification.

$$\text{Coefficient of variation (CV)} = \frac{\text{standard deviation (SD)}}{\text{Mean } (\bar{X})} \quad (4)$$

c) TLDs packing and measurement in ART phantom

All used TLD were arranged by the calibration factor from the highest to lowest. Two TLDs were coupled from the calibration factor close to each other and packed in a holder for the measurement. Figure 4.19 show the TLD holders and the position of the dosimeter in the holder.

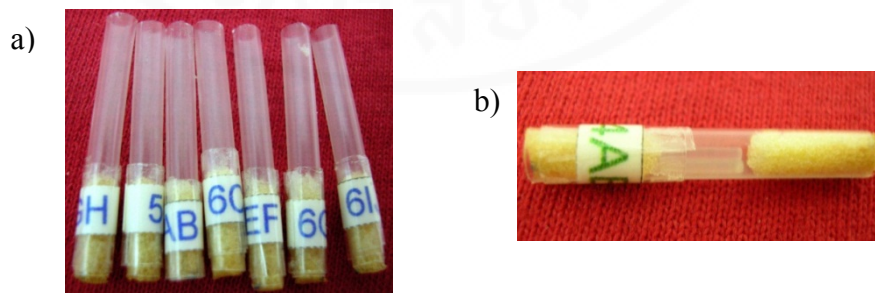


Figure 4.19 TLDs holders (a) and two TLDs were packed in the holder (b).

The TLD holder was placed in ART phantom at the measurement point in figure 4.20. The phantom with the holder inside was irradiated with the three IMRT plan from computer planning for three data sets. The dose measurement was performed in three times of each plan. The average signal in (nC) at

each point was used to calculate the dose distribution at the measurement point follow the equation 3.

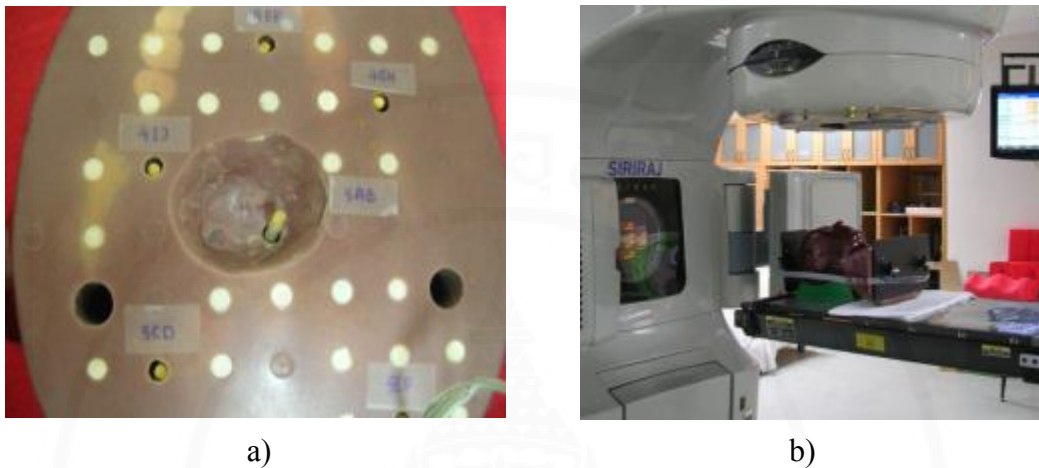


Figure 4.20 The holder was placed at the measurement point in ART phantom (a) and the phantom was irradiated with Varian Clinac 23EX linear accelerator (b).

4.2.4.3 Dosimetric verification

The dose measurement using at the representative points in head and neck region of ART phantom were evaluated by comparing with the corresponding TPS calculated dose. The variation of dose distribution was presented in term of percent difference from three different plans.

CHAPTER V

RESULTS

5.1 TLDs calibration and preparation for the measurement

From total number of 120 TLDs used in this experiment, the TLD signals from calibration with the known dose from Cobalt-60 gamma ray were from three repeated measurements. Using a statistical analysis, value of the mean (\bar{X}) standard deviation (SD) and percentage of coefficient of variation (%CV) from three readings were founded and the individual TLD calibration factor (CF) in nC/cGy were calculated as shown in table 5.1 The TLDs which exhibited their %CV greater than 3% will be ignored in this investigation. The TLD calibration factors were used to translate the TLD reading signal (nC) to the absorbed doses (cGy) for each measurement point in the humanoid phantom.

Table 5.1 Mean (\bar{X}), standard deviation (SD), percentage of coefficient of variation (%CV) of TLD readings and their individual calibration factor (CF)

TLD No.	Reading 1	Reading 2	Reading 3	\bar{X}	SD	%CV	CF (nC/cGy)
1	2239.00	2249.20	2216.60	2234.93	16.68	0.75	22.36
2	2237.40	2216.80	2235.00	2229.73	11.26	0.51	22.31
3	2117.20	2129.00	2133.30	2126.50	8.34	0.39	21.28
4	2134.60	2124.30	2091.20	2116.70	22.68	1.07	21.18
5	2105.10	2121.00	2118.00	2114.70	8.45	0.40	21.16
6	2133.00	2107.10	2099.80	2113.30	17.45	0.83	21.15
7	2103.40	2121.90	2106.30	2110.53	9.95	0.47	21.12
8	2065.00	2080.10	2113.70	2086.27	24.93	1.19	20.88
9	2070.60	2083.70	2093.30	2082.53	11.39	0.55	20.84
10	2058.90	2088.20	2096.90	2081.33	19.91	0.96	20.83

Table 5.1 Mean (\bar{X}) standard deviation (SD), percentage of coefficient of variation (%CV) of TLD readings and their individual calibration factor (CF) (cont.)

TLD No.	Reading 1	Reading 2	Reading 3	\bar{X}	SD	%CV	CF (nC/cGy)
11	2058.00	2107.00	2071.70	2078.90	25.28	1.22	20.80
12	2067.40	2091.70	2062.50	2073.87	15.64	0.75	20.75
13	2099.40	2061.20	2040.70	2067.10	29.79	1.44	20.68
14	2066.00	2067.70	2056.00	2063.23	6.32	0.31	20.65
15	2051.70	2067.50	2062.40	2060.53	8.06	0.39	20.62
16	2042.20	2063.30	2058.30	2054.60	11.03	0.54	20.56
17	2054.20	2066.50	2039.30	2053.33	13.62	0.66	20.55
18	2045.40	2050.60	2062.40	2052.80	8.71	0.42	20.54
19	2046.80	2040.90	2066.30	2051.33	13.29	0.65	20.53
20	2040.00	2038.30	2072.40	2050.23	19.22	0.94	20.51
21	2046.30	2044.50	2040.60	2043.80	2.91	0.14	20.45
22	2055.50	2055.80	2019.40	2043.57	20.93	1.02	20.45
23	2025.50	2060.70	2043.10	2043.10	17.60	0.86	20.44
24	2035.30	2029.70	2054.20	2039.73	12.84	0.63	20.41
25	2039.80	2063.40	2013.00	2038.73	25.22	1.24	20.40
26	2048.60	2024.40	2037.40	2036.80	12.11	0.59	20.38
27	2037.30	2027.00	2033.90	2032.73	5.25	0.26	20.34
28	2041.60	2025.40	2027.10	2031.37	8.90	0.44	20.33
29	2026.50	2045.60	2009.30	2027.13	18.16	0.90	20.29
30	2046.00	2013.30	2019.90	2026.40	17.29	0.85	20.28
31	2012.00	2006.50	2030.30	2016.27	12.46	0.62	20.18
32	1994.50	2024.80	2016.40	2011.90	15.64	0.78	20.13
33	2008.10	1987.00	2026.20	2007.10	19.62	0.98	20.08
34	1994.40	1997.10	2007.90	1999.80	7.14	0.36	20.01
35	2004.50	1992.90	1981.00	1992.80	11.75	0.59	19.94
36	1984.30	1993.90	1992.60	1990.27	5.21	0.26	19.92

Table 5.1 Mean (\bar{X}), standard deviation (SD), percentage of coefficient of variation (%CV) of TLD readings and their individual calibration factor (CF) (cont.)

TLD No.	Reading 1	Reading 2	Reading 3	\bar{X}	SD	%CV	CF (nC/cGy)
37	1989.20	1996.10	1980.20	1988.50	7.97	0.40	19.90
38	1958.80	2010.90	1945.20	1971.63	34.68	1.76	19.73
39	1965.60	1987.90	1948.80	1967.43	19.61	1.00	19.69
40	1961.80	1976.10	1953.10	1963.67	11.61	0.59	19.65
41	1986.20	1961.10	1892.40	1946.57	48.56	2.49	19.47
42	1622.80	1628.50	1636.70	1629.33	6.99	0.43	16.30
43	1620.50	1627.40	1639.50	1629.13	9.62	0.59	16.30
44	1625.00	1628.20	1613.80	1622.33	7.56	0.47	16.23
45	1613.90	1632.50	1610.70	1619.03	11.77	0.73	16.20
46	1587.60	1613.40	1592.60	1597.87	13.68	0.86	15.99
47	1614.90	1590.30	1585.20	1596.80	15.88	0.99	15.98
48	1606.60	1607.60	1576.10	1596.77	17.90	1.12	15.98
49	1597.40	1593.90	1590.30	1593.87	3.55	0.22	15.95
50	1587.20	1594.10	1594.60	1591.97	4.14	0.26	15.93
51	1588.10	1593.60	1579.60	1587.10	7.05	0.44	15.88
52	1594.10	1585.80	1579.10	1586.33	7.51	0.47	15.87
53	1588.20	1590.60	1576.00	1584.93	7.83	0.49	15.86
54	1589.60	1589.50	1573.80	1584.30	9.09	0.57	15.85
55	1575.10	1576.20	1594.30	1581.87	10.78	0.68	15.83
56	1585.90	1586.70	1572.60	1581.73	7.92	0.50	15.83
57	1587.50	1571.30	1585.40	1581.40	8.81	0.56	15.82
58	1576.90	1589.60	1576.90	1581.13	7.33	0.46	15.82
59	1588.10	1569.50	1576.20	1577.93	9.42	0.60	15.79
60	1583.50	1568.90	1574.00	1575.47	7.41	0.47	15.77
61	1588.80	1564.00	1567.60	1573.47	13.40	0.85	15.74
62	1577.70	1566.70	1572.90	1572.43	5.51	0.35	15.73

Table 5.1 Mean (\bar{X}) standard deviation (SD), percentage of coefficient of variation (%CV) of TLD readings and their individual calibration factor (CF) (cont.)

TLD No.	Reading 1	Reading 2	Reading 3	\bar{X}	SD	%CV	CF (nC/cGy)
63	1577.80	1571.50	1564.20	1571.17	6.81	0.43	15.72
64	1568.60	1574.30	1568.10	1570.33	3.44	0.22	15.71
65	1563.10	1567.00	1568.60	1566.23	2.83	0.18	15.67
66	1554.70	1559.30	1564.80	1559.60	5.06	0.32	15.61
67	1556.20	1551.40	1569.20	1558.93	9.21	0.59	15.60
68	1562.40	1561.20	1548.60	1557.40	7.64	0.49	15.58
69	1537.50	1577.20	1549.00	1554.57	20.43	1.31	15.56
70	1570.80	1549.40	1541.60	1553.93	15.12	0.97	15.55
71	1546.10	1548.10	1566.30	1553.50	11.13	0.72	15.54
72	1558.30	1556.60	1537.80	1550.90	11.38	0.73	15.52
73	1526.70	1545.60	1579.70	1550.67	26.86	1.73	15.52
74	1528.40	1566.00	1548.40	1547.60	18.81	1.22	15.49
75	1545.90	1538.30	1538.10	1540.77	4.45	0.29	15.42
76	1528.30	1555.60	1528.80	1537.57	15.62	1.02	15.38
77	1551.80	1528.30	1521.80	1533.97	15.78	1.03	15.35
78	1515.10	1540.50	1546.00	1533.87	16.48	1.07	15.35
79	1533.90	1530.30	1524.60	1529.60	4.69	0.31	15.31
80	1542.20	1520.50	1521.30	1528.00	12.30	0.81	15.29
81	1506.70	1517.10	1540.50	1521.43	17.31	1.14	15.22
82	1513.80	1527.90	1520.00	1520.57	7.07	0.46	15.22
83	1514.90	1535.40	1511.20	1520.50	13.04	0.86	15.21
84	1512.70	1512.00	1521.90	1515.53	5.52	0.36	15.17
85	1517.40	1505.10	1504.30	1508.93	7.34	0.49	15.10
86	1510.80	1507.80	1504.80	1507.80	3.00	0.20	15.09
87	1498.50	1495.10	1494.80	1496.13	2.06	0.14	14.97
88	1496.00	1494.40	1491.30	1493.90	2.39	0.16	14.95

Table 5.1 Mean (\bar{X}) standard deviation (SD), percentage of coefficient of variation (%CV) of TLD readings and their individual calibration factor (CF) (cont.)

TLD No.	Reading 1	Reading 2	Reading 3	\bar{X}	SD	%CV	CF (nC/cGy)
89	1494.40	1501.40	1485.80	1493.87	7.81	0.52	14.95
90	1508.30	1484.80	1487.40	1493.50	12.88	0.86	14.94
91	1507.30	1485.40	1484.40	1492.37	12.94	0.87	14.93
92	1481.70	1497.40	1485.70	1488.27	8.16	0.55	14.89
93	1481.90	1469.10	1493.90	1481.63	12.40	0.84	14.83
94	1495.00	1476.40	1471.30	1480.90	12.47	0.84	14.82
95	1459.00	1454.30	1457.20	1456.83	2.37	0.16	14.58
96	1417.00	1474.10	1450.60	1447.23	28.70	1.98	14.48
97	1449.20	1438.90	1427.60	1438.57	10.80	0.75	14.40
98	1435.50	1462.20	1415.60	1437.77	23.38	1.63	14.38
99	1423.30	1414.60	1472.20	1436.70	31.05	2.16	14.37
100	1394.00	1409.50	1420.00	1407.83	13.08	0.93	14.09
101	1405.50	1378.30	1403.50	1395.77	15.16	1.09	13.96
102	1358.40	1362.00	1354.70	1358.37	3.65	0.27	13.59
103	1358.50	1349.40	1359.40	1355.77	5.53	0.41	13.57
104	1353.70	1362.40	1332.80	1349.63	15.21	1.13	13.51
105	1353.80	1342.60	1347.60	1348.00	5.61	0.42	13.49
106	1341.20	1351.10	1348.10	1346.80	5.08	0.38	13.48
107	1361.70	1345.80	1332.60	1346.70	14.57	1.08	13.48
108	1346.40	1345.00	1346.60	1346.00	0.87	0.06	13.47
109	1340.30	1335.80	1338.10	1338.07	2.25	0.17	13.39
110	1365.70	1343.80	1298.20	1335.90	34.44	2.58	13.37
111	1339.20	1341.80	1323.30	1334.77	10.02	0.75	13.36
112	1340.40	1330.80	1331.10	1334.10	5.46	0.41	13.35
113	1345.80	1340.50	1312.60	1332.97	17.84	1.34	13.34
114	1344.60	1334.20	1309.60	1329.47	17.97	1.35	13.30

Table 5.1 Mean (\bar{X}) standard deviation (SD), percentage of coefficient of variation (%CV) of TLD readings and their individual calibration factor (CF) (cont.)

TLD No.	Reading 1	Reading 2	Reading 3	\bar{X}	SD	%CV	CF (nC/cGy)
115	1339.50	1323.30	1316.80	1326.53	11.69	0.88	13.27
116	1323.30	1322.80	1326.20	1324.10	1.84	0.14	13.25
117	1323.40	1328.40	1317.00	1322.93	5.71	0.43	13.24
118	1327.00	1318.50	1316.20	1320.57	5.69	0.43	13.21
119	1321.20	1323.00	1315.50	1319.90	3.92	0.30	13.21
120	1323.40	1312.70	1318.00	1318.03	5.35	0.41	13.19

5.2 Small field total output factor (S_{cp})

To investigate an effect of small field dosimetry on accuracy of IMRT dose calculation, beam data of the small field, 1×1 and 2×2 cm², on 6 MV photon were additional collected and configured to the Eclipse TPS. The total output factors (S_{cp}) which is defined as the ratio of the dose in the field of interest to the reference field 10×10 cm², were measured in water phantom at 10 cm depth with a Pinpoint chamber. The results of the total output factors in the series of the field size were shown in table 5.2

Table 5.2 The output factors in the series of field size, value in blue obtaining from field size 1×1 and 2×2 cm² and black from the routine measurement data of 3×3 - 40×40 cm² field .

Length (cm)	Width (cm)														
	1	2	3	4	5	6	8	10	12	15	20	25	30	35	40
1	0.721	0.758	0.766	0.770	0.772	0.775	0.776	0.778	0.779	0.780	0.781	0.782	0.782	0.783	0.782
2	0.791	0.843	0.857	0.866	0.870	0.874	0.879	0.881	0.883	0.885	0.887	0.890	0.889	0.889	0.890
3	0.797	0.859	0.856	0.868	0.874	0.880	0.887	0.890	0.890	0.895	0.899	0.902	0.902	0.902	0.902
4	0.804	0.871	0.889	0.902	0.909	0.917	0.927	0.931	0.934	0.936	0.941	0.946	0.946	0.946	0.948
5	0.808	0.877	0.898	0.914	0.923	0.931	0.941	0.949	0.952	0.956	0.961	0.966	0.966	0.966	0.967
6	0.812	0.883	0.907	0.927	0.936	0.946	0.956	0.966	0.971	0.975	0.980	0.985	0.985	0.985	0.985
8	0.816	0.888	0.917	0.938	0.952	0.966	0.975	0.987	0.993	1.000	1.005	1.010	1.013	1.015	1.015
10	0.818	0.895	0.927	0.942	0.959	0.975	0.990	1.000	1.010	1.015	1.023	1.029	1.029	1.034	1.032
12	0.820	0.897	0.907	0.947	0.964	0.980	1.000	1.017	1.020	1.029	1.039	1.042	1.049	1.049	1.047
15	0.822	0.901	0.912	0.956	0.972	0.988	1.010	1.023	1.029	1.039	1.049	1.059	1.064	1.069	1.066
20	0.826	0.906	0.917	0.961	0.979	0.998	1.020	1.034	1.044	1.057	1.069	1.076	1.083	1.088	1.088
25	0.827	0.908	0.922	0.966	0.984	1.003	1.025	1.042	1.052	1.064	1.078	1.086	1.093	1.098	1.098
30	0.829	0.910	0.924	0.969	0.989	1.010	1.029	1.044	1.059	1.072	1.086	1.096	1.103	1.108	1.108
35	0.831	0.913	0.927	0.971	0.990	1.010	1.034	1.054	1.062	1.078	1.093	1.101	1.111	1.116	1.118
40	0.832	0.915	0.931	0.971	0.992	1.013	1.038	1.054	1.067	1.080	1.098	1.106	1.118	1.121	1.122

5.3 TPS commissioned beam data

5.3.1 Verification of the TPS calculated beam depth doses and profiles

To validate the commissioning beam data, the calculated beam depth doses and profiles which generated from AAA 8.6 algorithm were verified with those from measurements. Comparison of the depth doses and profiles between the calculated and measured in different field sizes and depths in all beam data sets showed an excellent agreement. Figure 5.1-5.8 presented the depth doses and profiles of beam data set A (1×1 - 40×40 cm²) in the range of field size 1×1 - 3×3 and 10×10 cm². For beam data set B (2×2 - 40×40 cm²) and C (3×3 - 40×40 cm²), the comparisons were performed and shown in Appendix B.

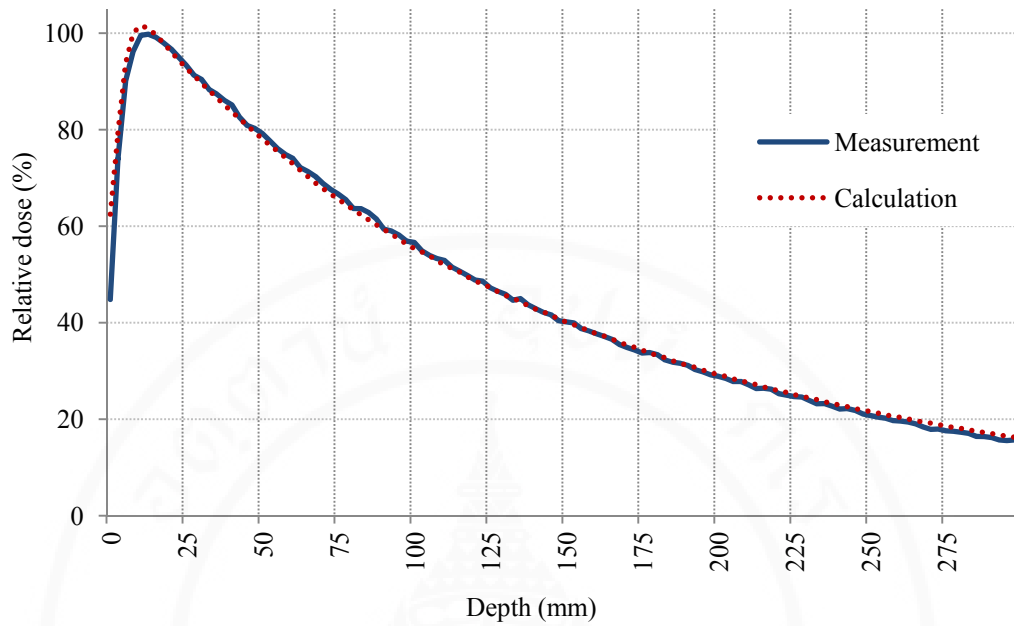


Figure 5.1 The comparison of PDD curves between the calculation (red) and measurement (blue) on beam dataset A (1×1 - 40×40 cm²) in 1×1 cm² field size at 100 cm SSD.

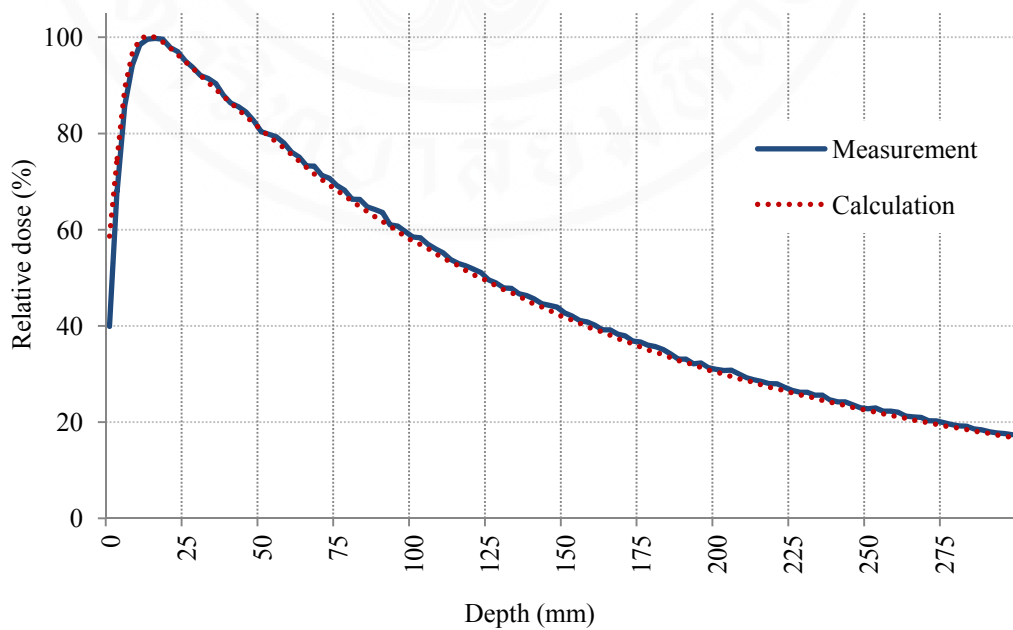


Figure 5.2 The comparison of PDD curves between the calculation (red) and measurement (blue) on beam dataset A (1×1 - 40×40 cm²) in 2×2 cm² field size at 100 cm SSD.

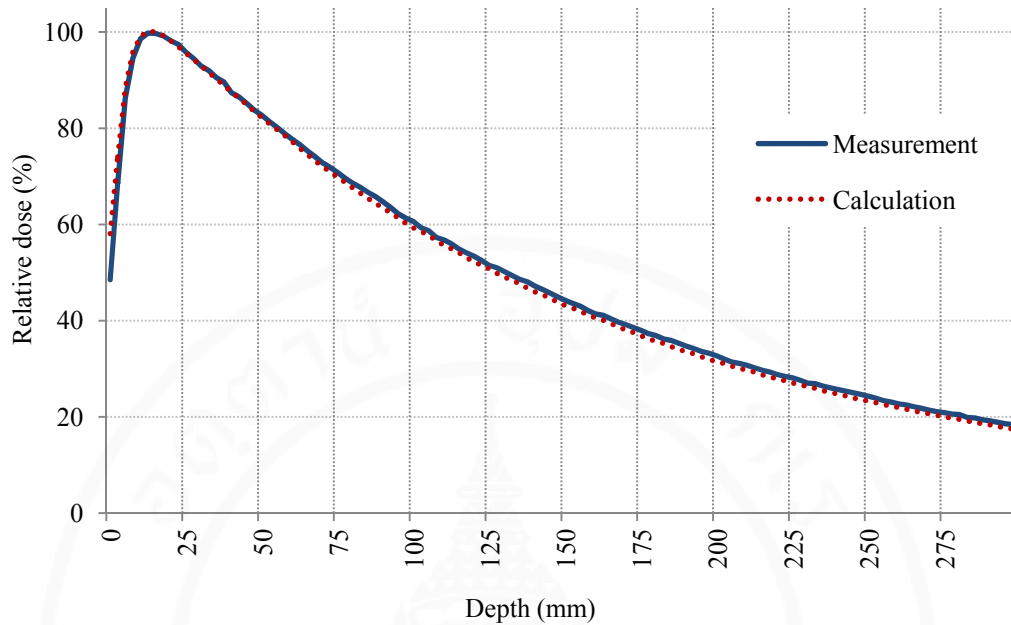


Figure 5.3 The comparison of PDD curves between the calculation (red) and measurement (blue) on beam dataset A ($1 \times 1-40 \times 40 \text{ cm}^2$) in $3 \times 3 \text{ cm}^2$ field size at 100 cm SSD.

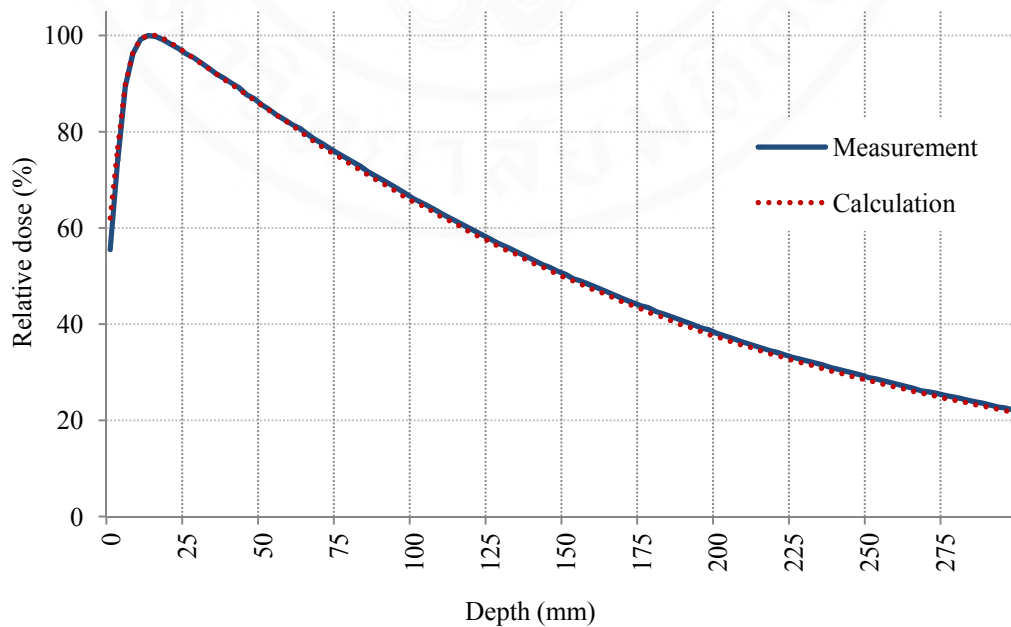


Figure 5.4 The comparison of PDD curves between the calculation (red) and measurement (blue) on beam dataset A ($1 \times 1-40 \times 40 \text{ cm}^2$) in $10 \times 10 \text{ cm}^2$ field size at 100 cm SSD.

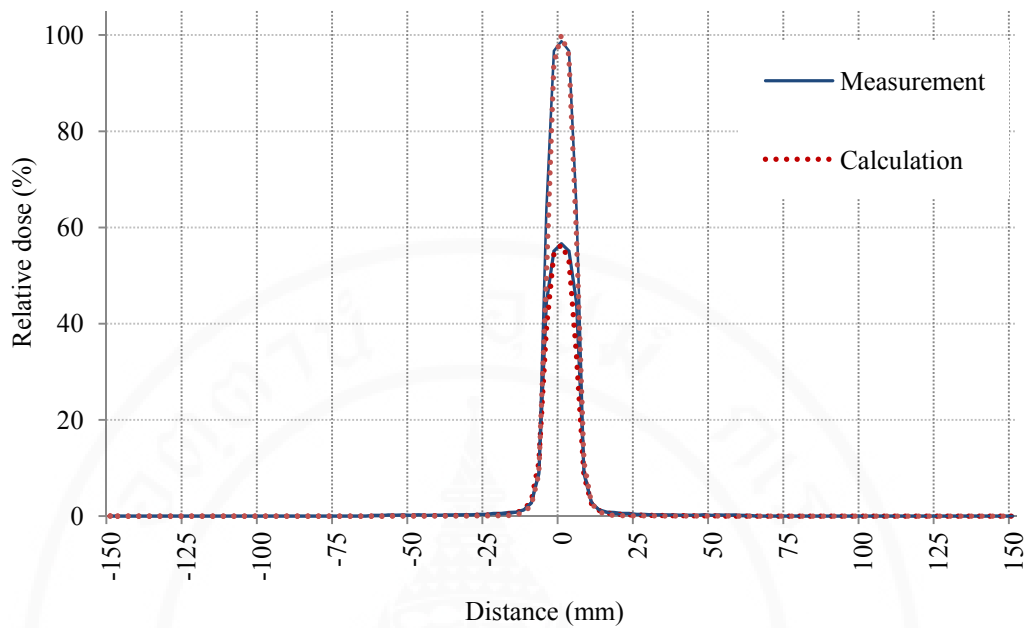


Figure 5.5 Comparison of the cross plane profiles between calculation and measurement in $1 \times 1 \text{ cm}^2$ field size from beam commissioning data $1 \times 1\text{-}40 \times 40 \text{ cm}^2$

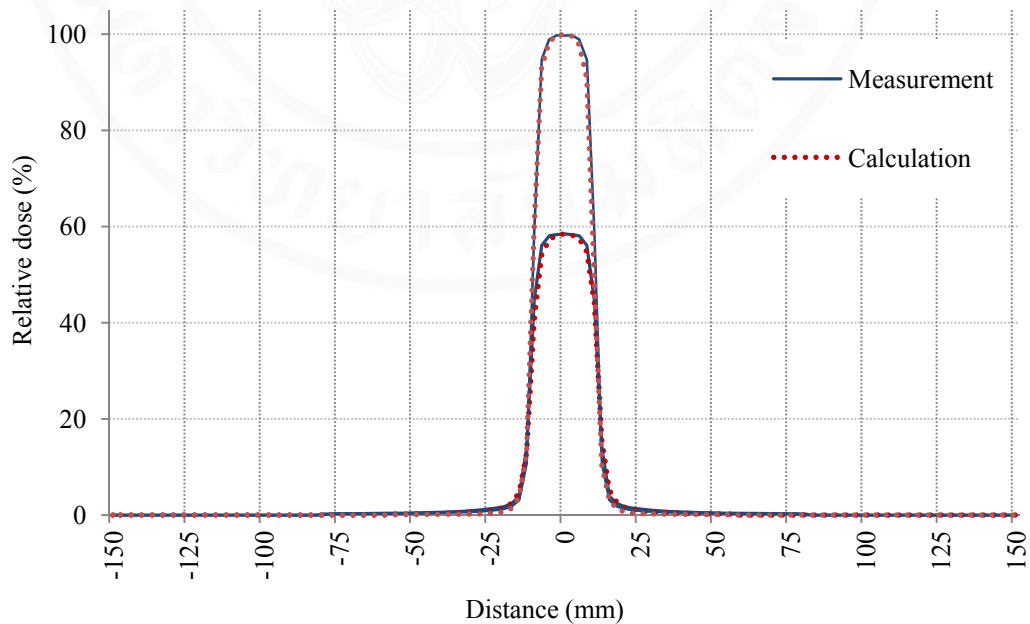


Figure 5.6 Comparison of the cross plane profiles between calculation and measurement in $2 \times 2 \text{ cm}^2$ field size from beam commissioning data $1 \times 1\text{-}40 \times 40 \text{ cm}^2$

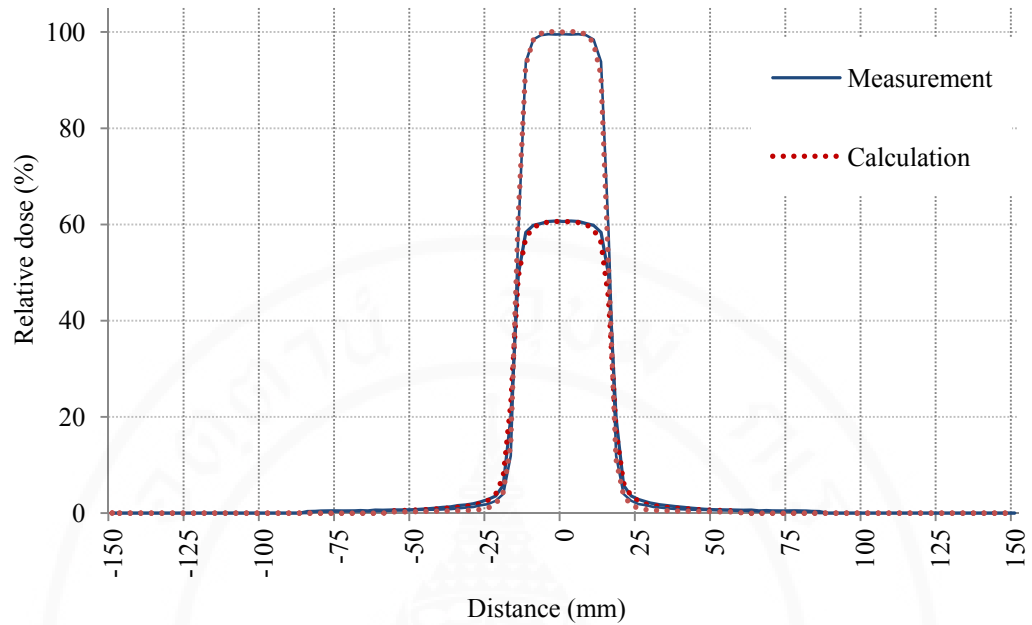


Figure 5.7 Comparison of the cross plane profiles between calculation and measurement in $3 \times 3 \text{ cm}^2$ field size from beam commissioning data $1 \times 1 - 40 \times 40 \text{ cm}^2$

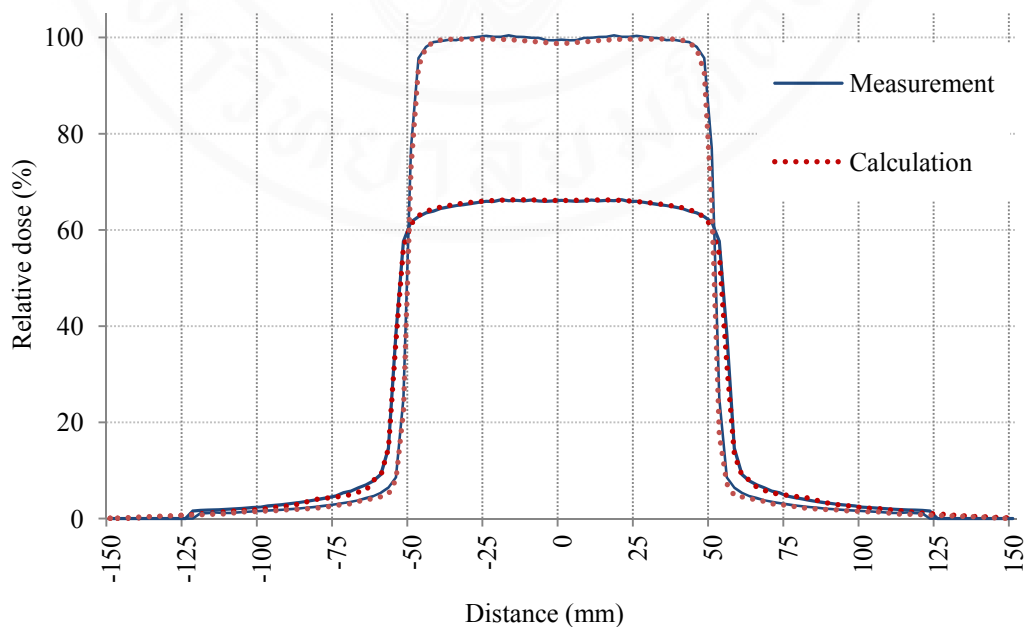


Figure 5.8 Comparison of the cross plane profiles between calculation and measurement in $10 \times 10 \text{ cm}^2$ field size from beam commissioning data $1 \times 1 - 40 \times 40 \text{ cm}^2$

5.3.2 Verification of the AAA 8.6 point dose calculation

Absolute measurement of point dose using the ionization chamber and water phantom at depth 10 cm for six square fields were performed at the same geometry as the verification plans illustrated in figure 5.9. In 1×1 to 3×3 cm^2 , the absolute dose were measured by Scanditronix Wellhofer CC01 (0.01 cc) and used Scdx-Wellhofer FC650-G/IC 70 farmer (0.65 cc) for measurement in large fields. Table 5.3 presented the percentage of dose difference between the AAA point dose calculation using 2.5 mm. grid size on different beam commissioning datasets with the measurement results. All deviations were found to be not greater than 2.5%.

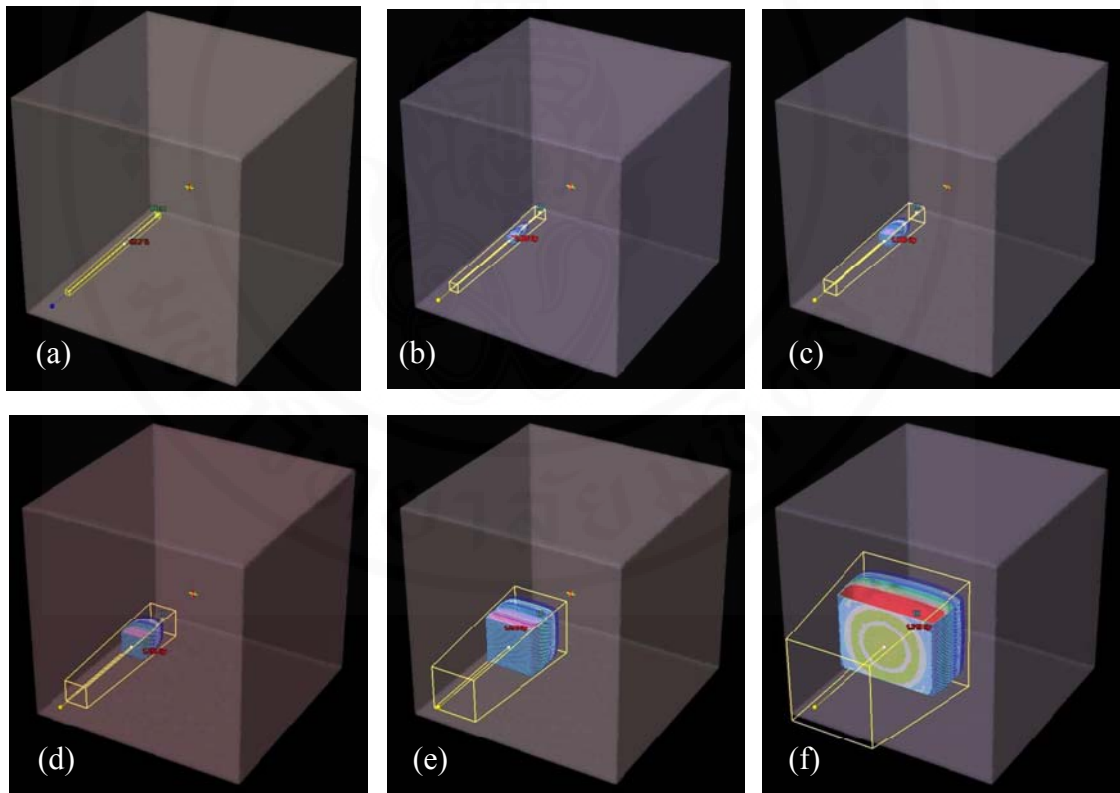


Figure 5.9 Virtual water phantoms were simulated in the Eclipse treatment planning system and used to calculate the point dose at depth 10 cm , SAD =100 cm in 1×1 (a), 2×2 (b), 3×3 (c), 5×5 (d), 10×10 (e) and 20×20 (f) cm^2 field size.

Table 5.3 The measured and calculated dose in 1×1, 2×2, 3×3, 5×5, 10×10 and 20×20 cm². The calculation was performed with three beam data set at depth 10 cm, SSD 90 cm. in water phantom.

Field size (cm ²)	Measurement (cGy)	1×1-40×40 cm ²		2×2-40×40 cm ²		3×3-40×40 cm ²	
		Dose (cGy)	%diff	Dose (cGy)	%diff	Dose (cGy)	%diff
1×1	50.94	51.6	1.30	52.2	2.47	52.4	2.87
2×2	61.5	61	-0.81	61	-0.81	61.3	-0.33
3×3	65.82	64.8	-1.55	64.9	-1.40	64.5	-2.01
5×5	70.76	69.2	-2.20	69.3	-2.06	69.3	-2.06
10×10	79.71	77.8	-2.40	77.9	-2.27	77.9	-2.27
20×20	88.14	86	-2.43	86.2	-2.20	86.1	-2.31

5.4 Head and neck IMRT dose distribution calculated from different beam commissioning data

5.4.1 Number of monitor units and subfields on three IMRT plans

Beam geometry and detail of treatment field in each direction of the seven-field sliding window head and neck IMRT plan was shown in figure 5.10 and table 5.4. The target volume prescription dose and dose constraint at organ at risk were optimized based on the protocol of head and neck IMRT plan at department of radiation oncology, Siriraj hospital. After the optimization process was successfully obtained, the final IMRT dose distribution was firstly calculated using AAA 8.6 algorithm on the routine commissioning beam data (3×3-40×40 cm²). Then two more copied of IMRT plans were created and dose distributions were recalculated using beam commissioning data on set A (1×1-40×40 cm²) and set B (2×2-40×40 cm²), respectively. Monitor units (MU) and number of field segments in all three IMRT plans were as well compared. It was observed that all three plans on different beam commissioning data have the same number of MUs and subfields as presented in table 5.5.

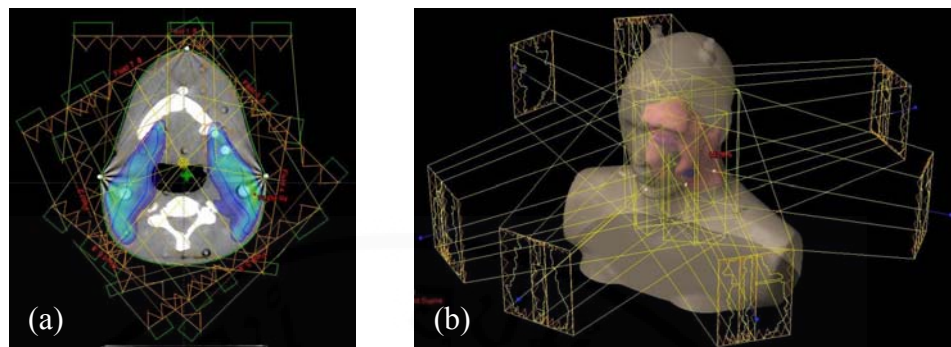


Figure 5.10 Beam directions of seven-field head and neck IMRT treatment plan in ART phantom, shown in 2D view (a) and 3D view (b).

Table 5.4 Gantry angle and detail of treatment field used in IMRT plan

Field	Gantry	Field X	X1	X2	Field Y	Y1	Y2
1_1	0	11.4	9	2.4	21.6	10.3	11.3
1_2	0	10.1	1.3	8.8	21.6	10.3	11.3
2	250	13.5	8	5.5	21.8	10.5	11.3
3_1	45	8.3	6.4	1.9	22	10.5	11.5
3_2	45	11.6	1.8	9.8	22	10.5	11.5
4	100	12.6	5.1	7.5	21.8	10.5	11.3
5_1	145	13	7	6	21.8	10.5	11.3
5_2	145	8	-2	10	21.8	10.5	11.3
6_1	220	11.9	9.8	2.1	21.8	10.5	11.3
6_2	220	7.6	1.6	6	21.8	10.5	11.3
7_1	330	8.1	10	1.9	21.8	10.3	11.5
7_2	330	12.6	5.8	6.8	21.8	10.3	11.5

Table 5.5 Comparison of the monitor unit (MU) and field segmentation in three calculated IMRT plans.

Field	Plan A (1×1-40×40 cm ²)		Plan B (2×2-40×40 cm ²)		Plan C (3×3-40×40 cm ²)	
	MU	No. segment	MU	No. segment	MU	No. segment
1_1	147	66	147	66	147	66
1_2	170	79	170	79	170	79
2	190	124	190	124	190	124
3_1	124	102	124	102	124	102
3_2	129	108	129	108	129	108
4	160	118	160	118	160	118
5_1	220	166	220	166	220	166
5_2	84	72	84	72	84	72
6_1	155	152	155	152	155	152
6_2	140	138	140	138	140	138
7_1	90	69	90	69	90	69
7_2	180	142	180	142	180	142

5.4.2 Comparison of the IMRT segmental field shape and area

In IMRT technique, the treatment field can be divided into more than one hundred irregular-shaped subfields. Using the same optimization, in this study the segmental field shape and area were examined among three IMRT plans. Sampling of four subfields from IMRT field at each gantry were examined. It can be seen that all three plans exhibited the similar segmental field shape as shown in figure 5.11 and 5.12 which were the subfields from gantry angle 0 and 220 degree, respectively. All investigated subfields area from all gantry angles were summarized and shown in table 5.6 and 5.7. The results showed that all three IMRT plans in this study, provided the same field segmental shape and area. By percentage difference of the subfield area doses not exceed than 0.5%, thus the parameter of field area do not affect on the dose calculation.

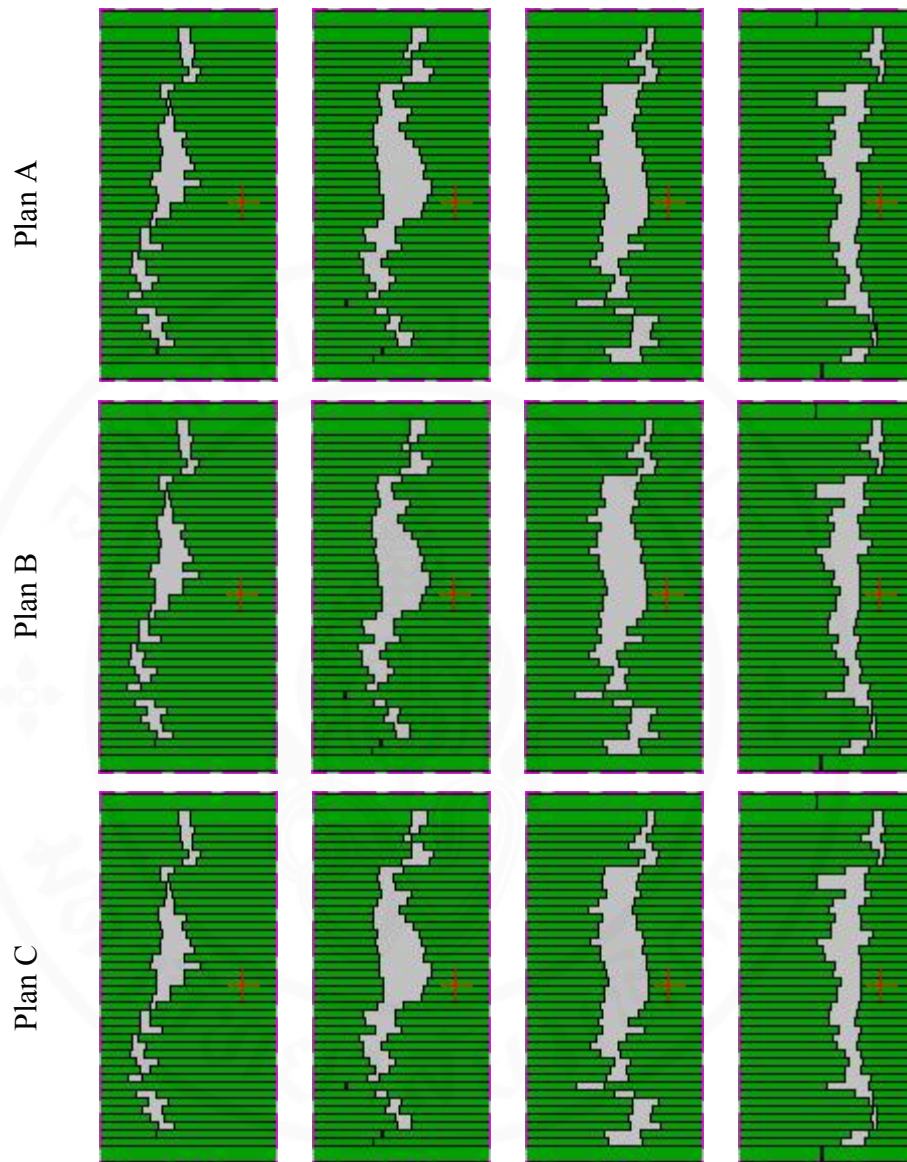


Figure 5.11 Four samples of IMRT segmental shapes observed at gantry 0 degree on three different plans of head and neck IMRT.

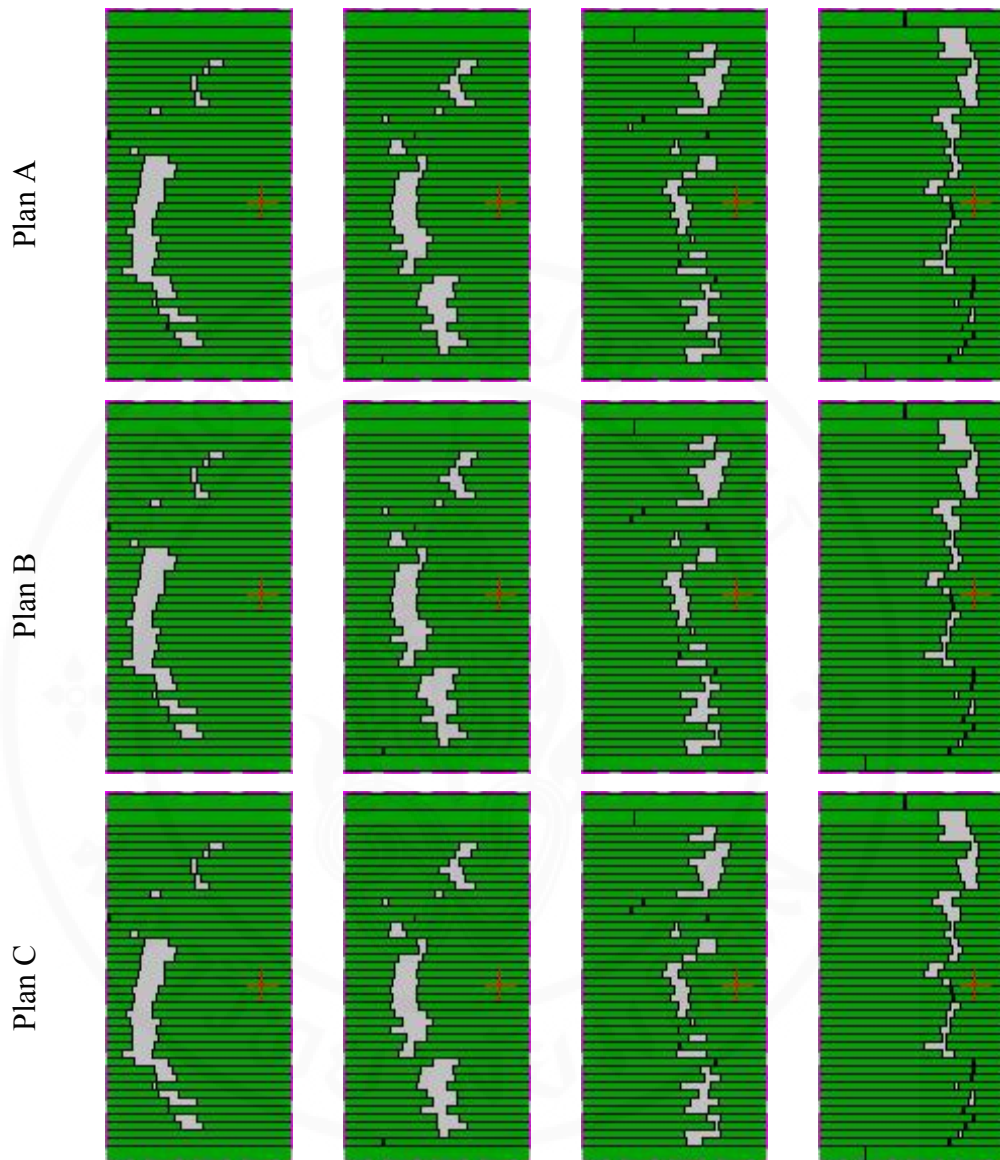


Figure 5.12 Four samples of IMRT segmental shapes observed at gantry 220 degree on three different plans of head and neck IMRT.

Table 5.6 The subfield area in field segment no.1 and no.2 of three IMRT plans

Field	Field area in segment no.1 (cm ²)			Field area in segment no.2 (cm ²)		
	Plan A	Plan B	Plan C	Plan A	Plan B	Plan C
1_1	21.1	21.0	21.0	32.9	32.8	32.8
1_2	21.5	21.5	21.4	26.7	26.7	26.7
2	15.9	15.9	15.9	23.5	23.4	23.4
3_1	10.4	10.4	10.4	15.6	15.6	15.6
3_2	5.8	5.8	5.8	11.2	11.1	11.1
4	38.4	38.3	38.3	49.8	49.7	49.7
5_1	16.4	16.3	16.3	22.8	22.8	22.8
5_2	9.2	9.2	9.3	16.3	16.4	16.4
6_1	20.1	20.1	20.1	23.9	23.8	23.8
6_2	10.1	10.1	10.1	18.2	18.1	18.1
7_1	8.9	8.9	8.9	12.8	12.7	12.7
7_2	13.2	13.2	13.2	17.7	17.7	17.8

Table 5.7 The subfield area in field segment no.3 and no.4 of three IMRT plans

Field	Field area in segment no.3 (cm ²)			Field area in segment no.4 (cm ²)		
	Plan A	Plan B	Plan C	Plan A	Plan B	Plan C
1_1	40.3	40.3	40.3	30.7	30.6	30.6
1_2	27.2	27.2	27.2	21.0	21.0	20.9
2	36.0	36.0	36.0	29.0	29.0	29.0
3_1	21.4	21.3	21.4	24.5	24.5	24.5
3_2	17.3	17.2	17.3	24.3	24.2	24.2
4	36.4	36.3	36.3	18.9	18.9	18.9
5_1	22.8	22.8	22.8	23.8	23.8	23.8
5_2	20.1	20.1	20.1	13.1	13.1	13.1
6_1	20.1	20.1	20.0	14.5	14.5	14.5
6_2	28.5	28.5	28.5	21.1	21.2	21.1
7_1	11.7	11.6	11.6	9.0	9.0	9.1
7_2	28.5	28.4	28.5	28.8	28.7	28.7

5.4.3 Dose volume histograms (DVHs) comparison

To examine the calculated IMRT dose distribution based on three different beam data commissionings, cumulative DVHs were as well generated on each plan and compared. It was found that, all three IMRT plans showed the similar cumulative DVHs. By statistical dose parameters such as a maximum dose (D_{max}), a minimum dose (D_{min}) and a mean dose (D_{mean}) of the target volume (GTV, CTV and PTV) as well as a number of organs at risk (spinal cord, brainstem, right and left temporal lobes, parotid glands) showed a variation of dose from each other less than 1%. Figure 5.13 showed the cumulative DVH of the CTV and critical organs; spinal cord, brain stem and temporal lobes. Evaluated dose parameters were as well summarized in table 5.8.

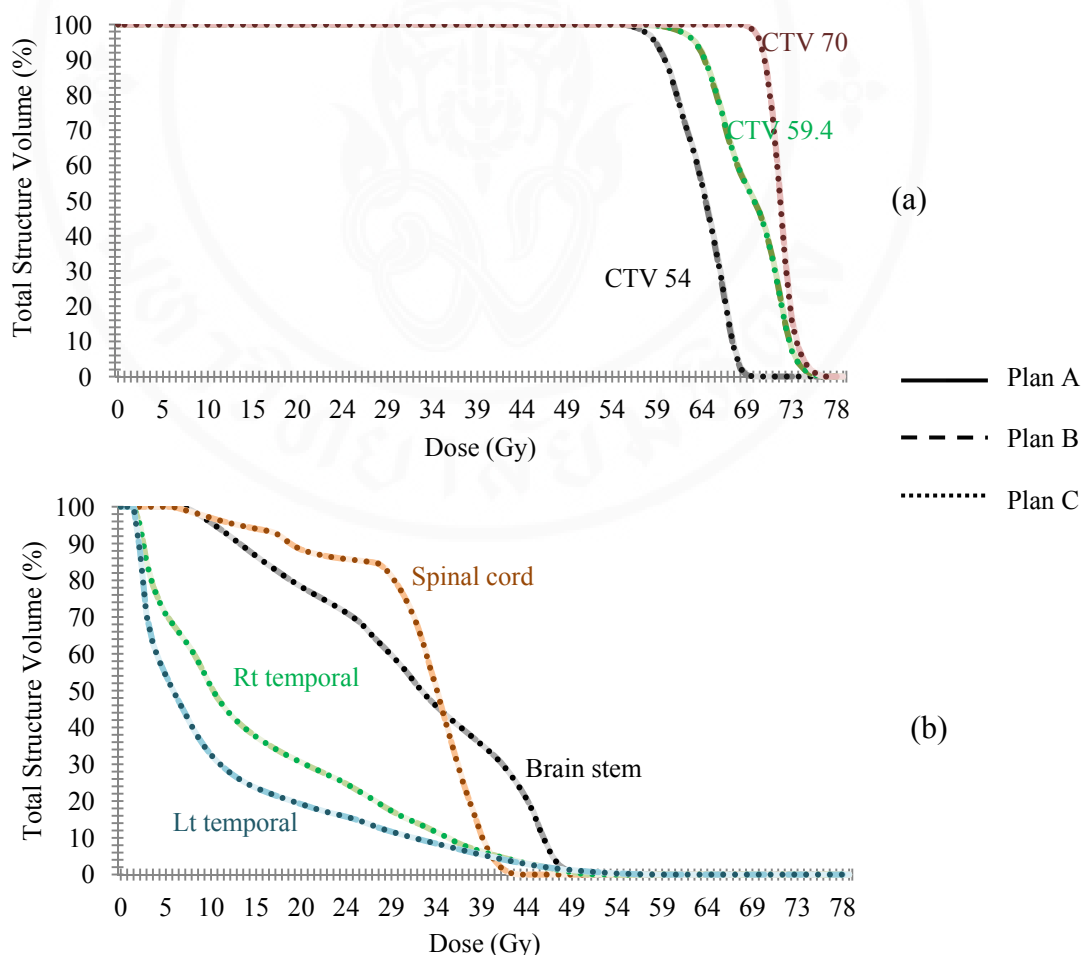


Figure 5.13 Cumulative DVH of (a) the clinical target volumes (CTV70, CTV59.4 and CTV 54) and (b) spinal cord, brainstem and brain (right and left temporal lobes) in all three IMRT plans.

Table 5.8 Summation of the maximum dose (D_{\max}), mean dose (D_{mean}) and minimum dose (D_{\min}) in the target volumes and organ at risks of the IMRT calculated on beam data set A, B and C, respectively.

Structure	D_{\max} (Gy)			D_{mean} (Gy)			D_{\min} (Gy)		
	Plan A	Plan B	Plan C	Plan A	Plan B	Plan C	Plan A	Plan B	Plan C
GTV	76.7	76.6	76.6	72.1	72.1	72.1	68.1	68.0	68.0
CTV 54	70.5	70.4	70.5	63.7	63.6	63.6	54.7	54.7	54.7
CTV 59.4	77.5	77.4	77.5	68.9	68.8	68.8	45.4	45.4	45.4
CTV 70	77.3	77.2	77.2	72.3	72.2	72.2	66.8	66.7	66.7
PTV 54	71.3	71.1	71.3	62.9	62.8	62.8	47.5	47.3	47.4
PTV 59.4	77.7	77.6	77.6	66.8	66.8	66.8	35.9	35.9	35.9
PTV 70	77.7	77.6	77.6	71.6	71.6	71.6	58.7	58.6	58.6
Brain stem	51.2	51.2	51.1	31.5	31.5	31.5	6.4	6.4	6.4
Spinal cord	43.6	43.5	43.5	32.2	32.2	32.2	5.3	5.3	5.3
Rt Temporal	56.5	56.5	56.4	14.9	14.9	14.9	1.5	1.5	1.5
Lt Temporal	59.1	59.0	59.0	11.0	11.0	11.0	1.4	1.4	1.5
Rt Len	3.0	3.0	2.9	2.8	2.8	2.8	2.7	2.7	2.7
Lt Len	3.0	3.0	3.0	2.9	2.9	2.8	2.8	2.8	2.7
Rt Eye	18.4	18.4	18.4	4.4	4.4	4.4	2.2	2.2	2.2
Lt Eye	17.3	17.3	17.3	3.9	3.2	3.9	2.1	2.1	2.1
Rt Parotid	73.2	73.1	73.1	48.2	48.1	48.2	18.5	18.4	18.5
Lt Parotid	79.1	78.8	79.0	47.3	47.1	47.2	23.5	23.4	23.5
Rt Sup parotid	70.3	70.2	70.3	41.9	41.7	41.8	18.4	18.3	18.4
Lt Sup parotid	79.1	78.8	79.0	40.3	40.1	40.2	23.5	23.4	23.5
Rt TM joint	56.1	56.0	56.0	43.9	43.9	43.9	33.2	33.2	33.2
Lt TM joint	57.2	57.1	57.1	35.9	35.8	35.8	27.3	27.2	27.2
Mandible	76.2	76.0	76.1	48.5	48.4	48.5	9.7	9.7	9.7
Oral cavity	65.0	64.9	64.9	38.4	39.4	39.4	9.8	9.7	9.8

5.4.4 Verification of the 2D planar dose distribution on three IMRT plans

The TPS planar dose distribution on three head and neck IMRT plans was as well evaluated using the measured dose from the MapCHECK 2D detector arrays. From the total number of 755 measuring points, the passing rate using the criteria of 3% dose difference and 3 mm DTA, can be detected on IMRT plan A, B and C at 98.9%, 97.9% and 99.1%, respectively. Good agreement of dose at point of beam

central axis, were as well presented at 2.06%, 3.16% and 2.13% on three IMRT plans. Figure 5.14 showed the comparison of the calculated and measured dose distribution obtained from three IMRT in this study.

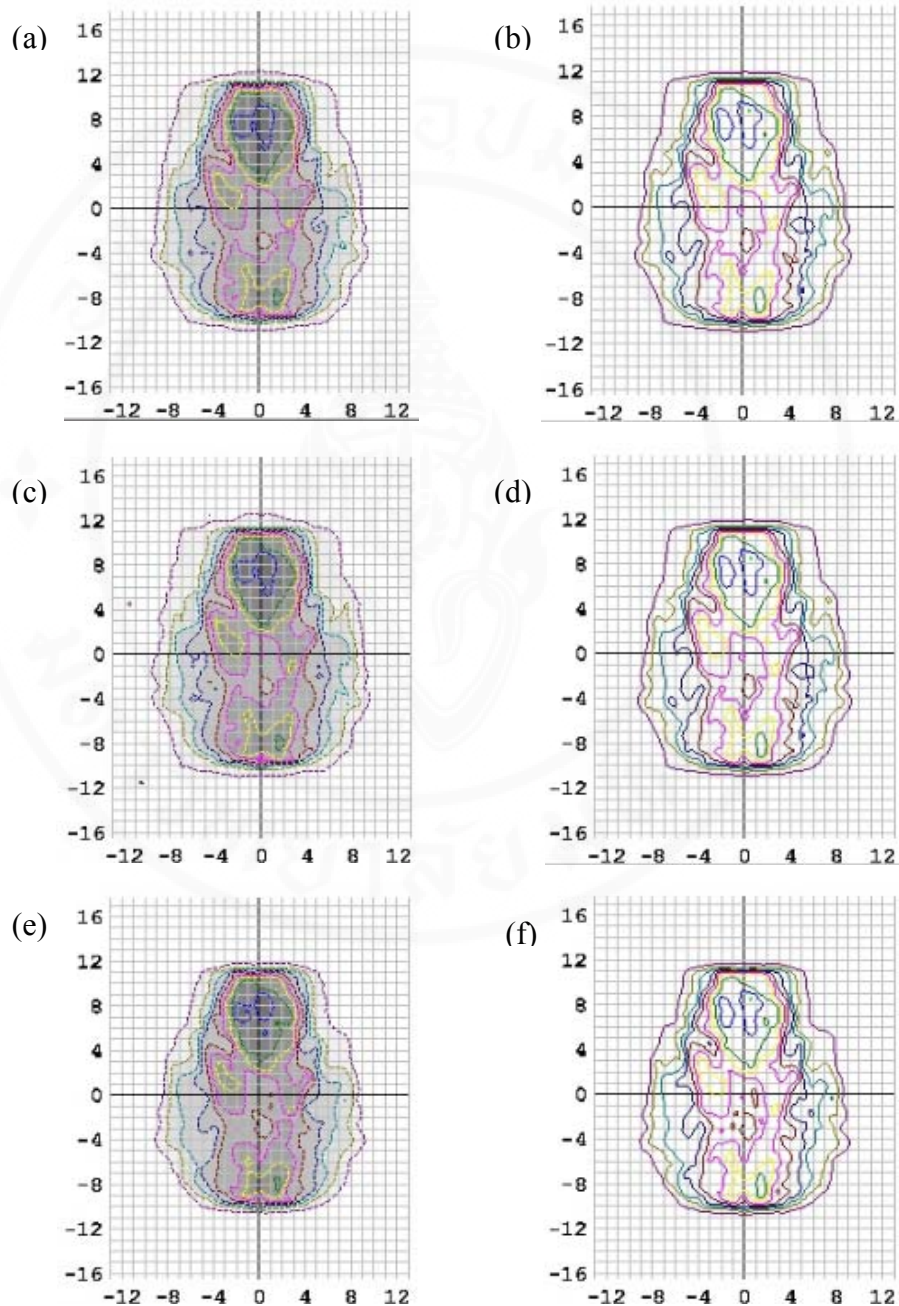


Figure 5.14 Planar dose distribution verified with MapCHECK on three head and neck IMRT plans. Left side (a), (c), (e) are the measured dose distribution obtained from IMRT plan A, B and C, respectively and the right side are the TPS planned dose

In the next step, the other criteria (2%, 2 mm and 1%, 1 mm) was used to verify the difference. The agreement of the dose distribution between measurement and calculation in all plans were decrease in the same direction. The passing rate were presented at 97.6%, 90.1%, 93.4% that used 2%, 2 mm criteria and decreased to 59.9%, 55.9%, 61.5% for 1%, 1 mm criteria of plan A, B and C, respectively.

5.5 IMRT point dose verification using TLD-100 dosimeters

The accuracy of AAA 8.6 algorithm for IMRT dose calculations based on different beam commissioning data was verified by performing point dose measurement with TLD-100 dosimeters in ART phantom. Performance of the TLD measurement was firstly assessed from the percentage of dose deviation and their standard deviation (SD) at point of the central axis (CAX) beam. In this investigation, the measurement accuracy was found to be satisfactorily acceptable, by an average percent difference of dose between calculation and the measurement at CAX point was to be $2.135 \pm 2.707\%$, $2.053 \pm 6.605\%$ and $3.770 \pm 2.202\%$ on plan A, B and C, respectively. All three IMRT plans still presented the similar calculated readings on each observed point. This can be implied that, the additional small field dosimetry, of 1×1 and 2×2 cm² beam data, for the AAA 8.6 commissioning do not affect on the quality of dose calculation in head and neck IMRT plan.

However, the AAA 8.6 calculated dose from a total number of sixty measuring points, were detected to be underestimation. The range of dose difference is seen between 5% to -19% for all plans with mean \pm SD of all calculated dose points when compared to measurement were at $-9.284 \pm 3.751\%$, $-9.827 \pm 3.771\%$ and $-9.888 \pm 3.358\%$, respectively. The worst point with -19% dose underestimation was observed at point 5AB which is the location of air cavity in the phantom. About fifty percent of the measuring points were detected to be 10% greater than the TPS calculated dose. Figure 5.15-5.18 showed percent dose deviation at each measurement point in ART phantom and as the plotted graph on three IMRT plans. Frequency of dose deviation between the measurement and calculation was also analyzed and shown in figure 5.19. Result of the measured doses from TLD-100 dosimeters presented the

underestimation of calculation dose while this finding cannot be detected from the planar dose distribution verification with MapCHECK QA system.

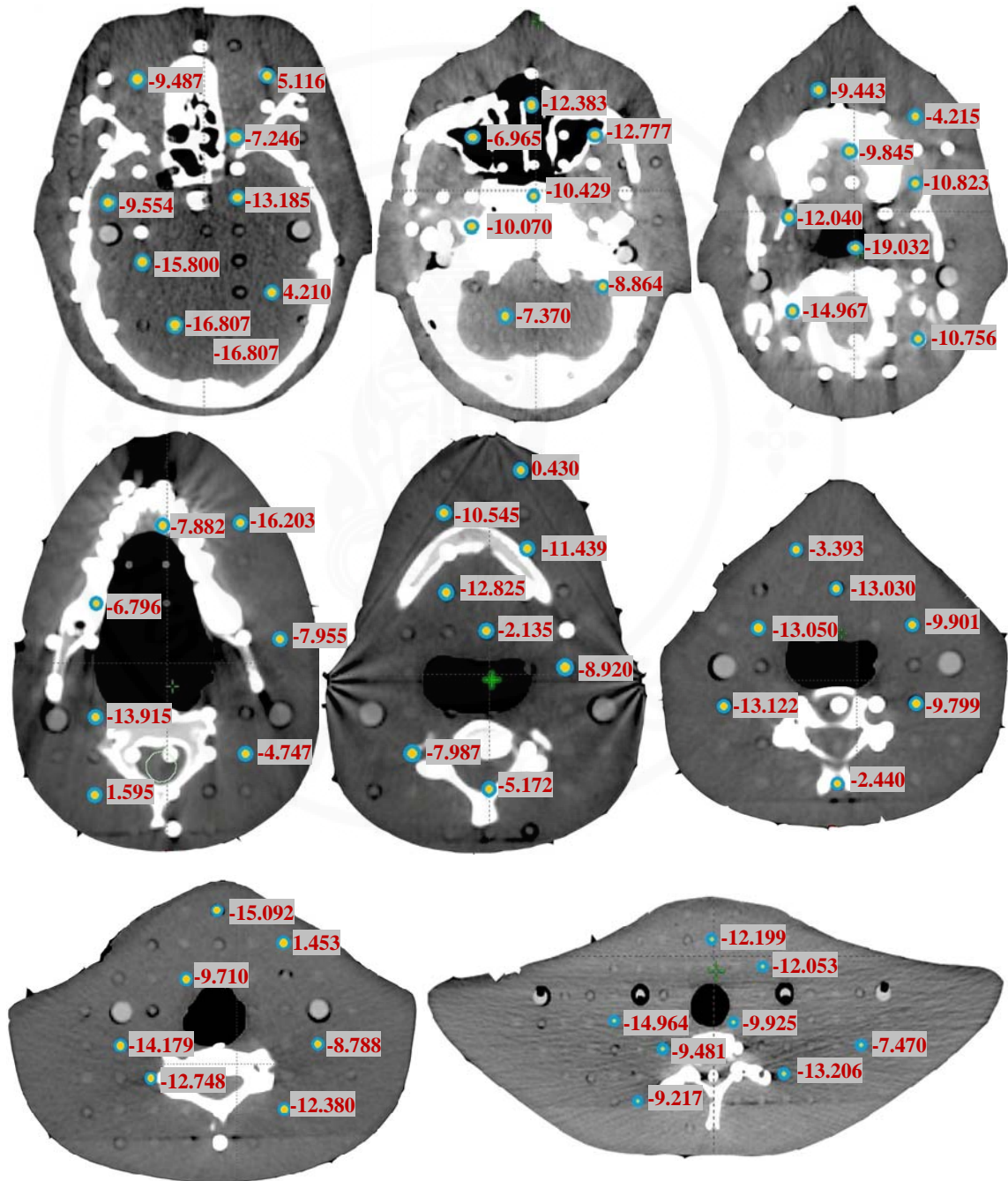


Figure 5.15 The percent difference of the calculation dose in plan A compared with the TLDs measurement for each point

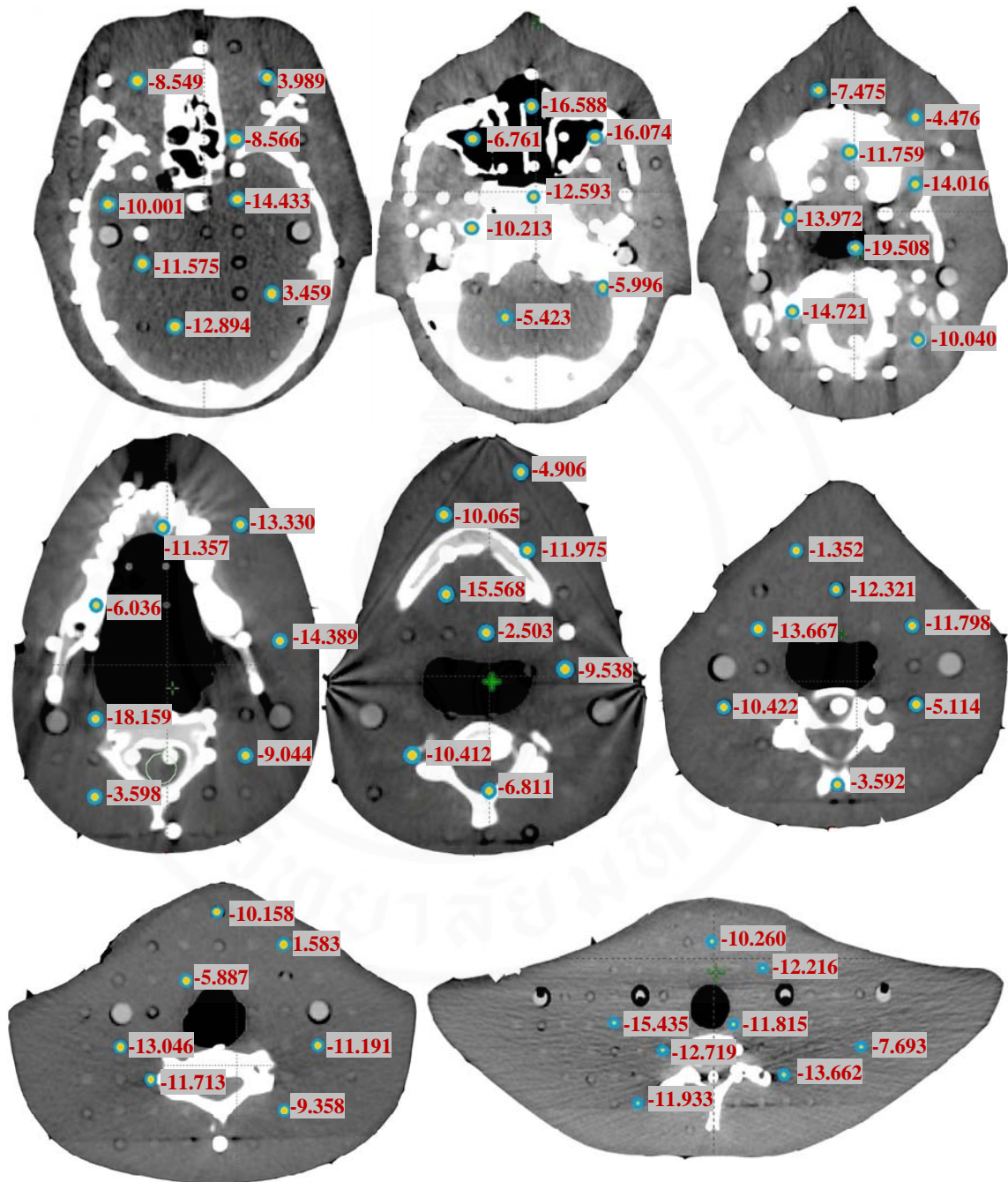


Figure 5.16 The percent difference of the calculation dose in plan B compared with the TLDs measurement for each point

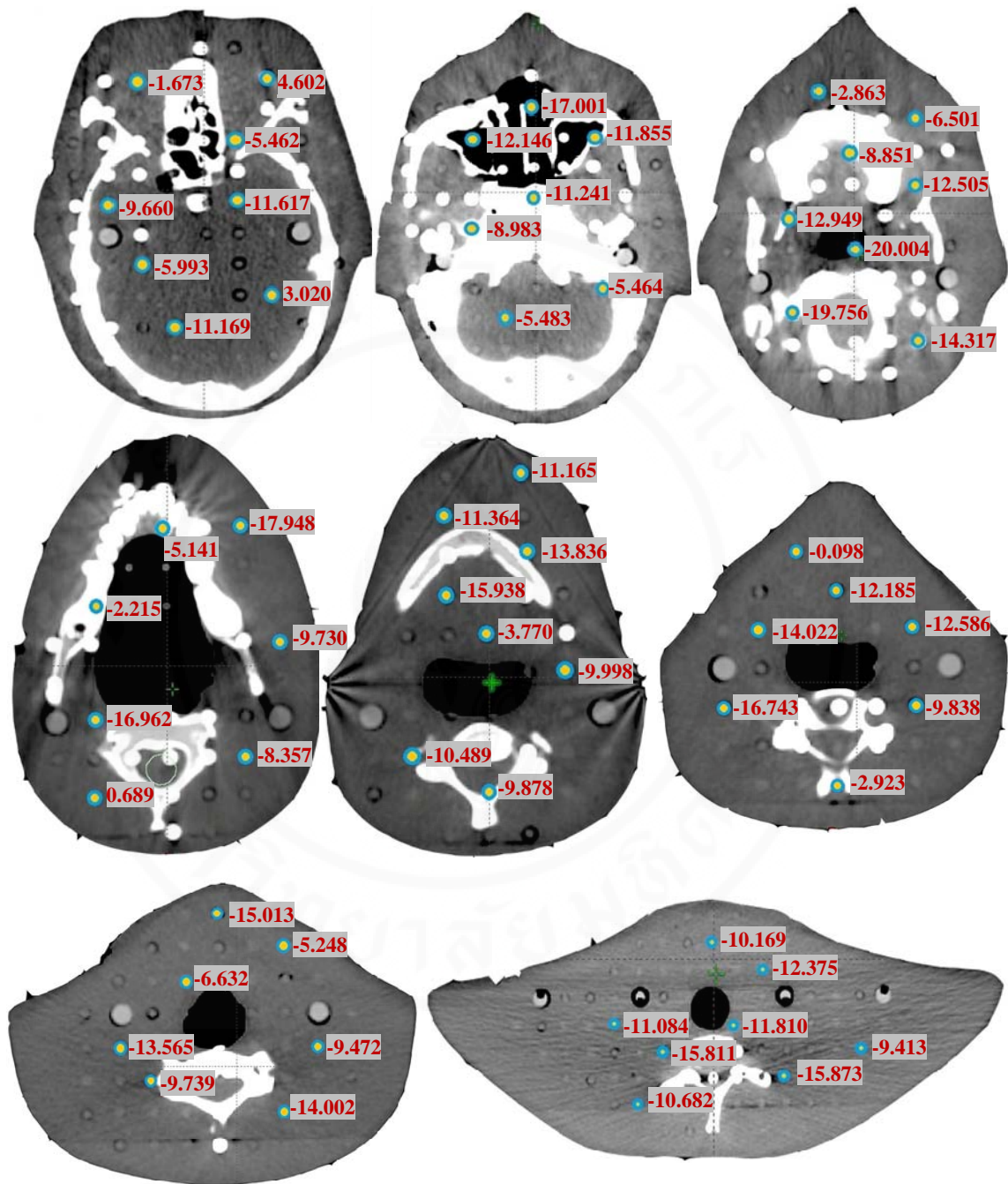


Figure 5.17 The percent difference of the calculation dose in plan C compared with the TLDs measurement for each point

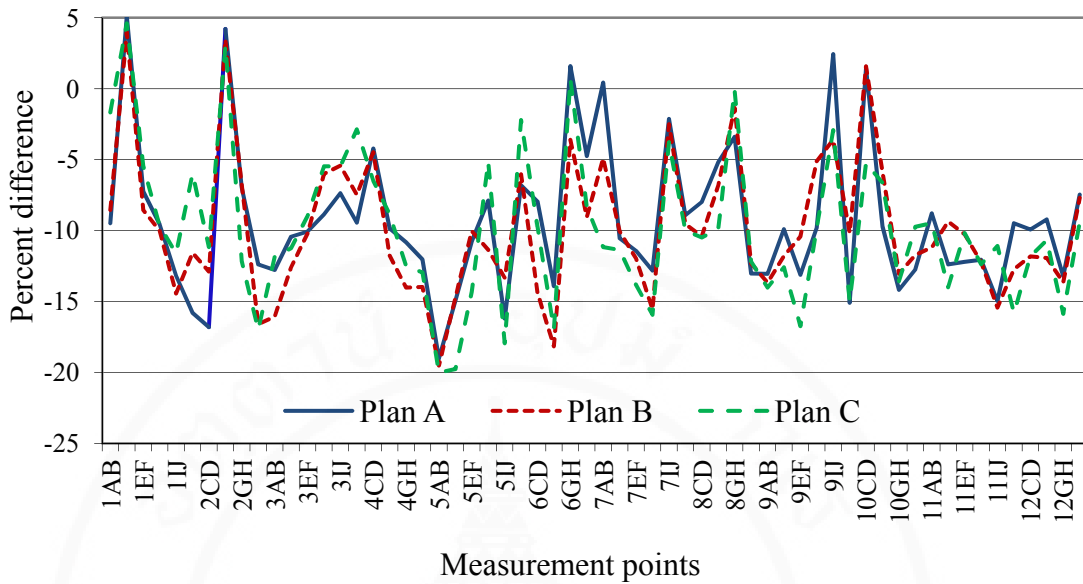


Figure 5.18 Percent dose difference between calculation and measurement at each TLD point in humanoid head and neck phantom of three IMRT plans

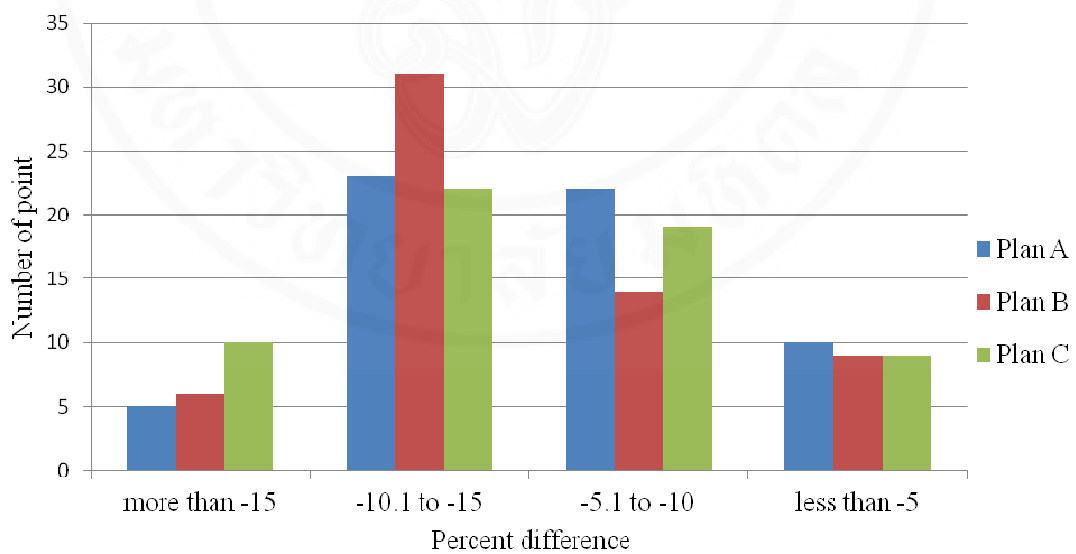


Figure 5.19 The percent difference frequency between the measurement and the calculation of three IMRT plans.

CHAPTER VI

DISCUSSION AND CONCLUSIONS

6.1 Appropriate beam commissioning data for AAA 8.6 algorithm

The non-uniform dose distribution in advance technique as IMRT, the small segmented field to create the intensity pattern. It is challenging for all types of dose calculation algorithm to predict the accurate dose under these small and narrow field geometries. To obtain the desired accuracy, AAPM report of TG-106 has recommended the TPS beam commissioning data suited for IMRT technique in clinical practice. The report suggest beam data for IMRT should be collected in the range of field size from 1×1 to 40×40 cm² fields to increase the accuracy of IMRT dose calculation.

At Division of radiation oncology, Siriraj hospital, the routine beam data validated for Eclipse TPS for both 3D-CRT and IMRT technique, was previously acquired on field size 3×3 to 40×40 cm². Thus, the IMRT dose calculation based on the smallest field dosimetry at 3×3 cm², should be investigated for their accuracy. In this study, due to the complex intensity pattern of head and neck IMRT, dose distributions calculated on three different beam commissioning data for AAA 8.6 were compared. Results of the examination, would suggest an appropriate beam dataset for Eclipse TPS commissioning for IMRT application. The accuracy level of AAA 8.6 algorithm for predicting dose distribution on head and neck IMRT plan were as well determined by compared with the measured dose using TLD-100 dosimeters.

From the investigation, it was clearly seen that all three beam commissioning data presented the similar calculated depth doses and profiles for the small fields. Using criteria for acceptability according to Venselaar et al [42], the calculated depth dose and profiles of the small fields, 1×1 to 3×3 cm², were analyzed and compared with measurements. Excellent agreement of the depth doses at point beyond the d_{\max} (δ_1), at point in the buildup region, 90% of dose (δ_{2a}) and point at the deeper depth, 10% of dose (δ_{2b}) of all the calculated depth doses were observed as

shown in Table 6.1. About the profiles, verification at depth d_{\max} and 10 cm. using the criteria of point outside the central axis which contain small dose gradient (δ_3), and at point of off the beam edges (δ_4), the % variation were found to be less than 1%. Comparison of the field width (RW_{50}) and beam fringe (δ_{50-90}), as well detected the distance of difference were within ± 1 mm for all beam data set as shown in Table 6.2 and 6.3. It is indicated from the results that acquisition of the beam data for Eclipse TPS for IMRT calculation, the smallest field dosimetry can be started at field size 3×3 cm^2 . Since, the AAA algorithm is efficient enough to extend the calculated small field depth dose and profiles to be 1×1 and 2×2 cm^2 field, with an acceptable accuracy.

Table 6.1 The result of depth dose verification in 1×1 , 2×2 , 3×3 and 10×10 cm^2 at d_{\max} depth of three beam data sets.

Field size (cm^2)	Beam data set	δ_1^* (%)	δ_{2a}^* (mm)	δ_{2b}^* (%)
1×1	A (1×1-40×40 cm^2)	-0.357	0.376	4.355
	B (2×2-40×40 cm^2)	-0.022	0.003	1.566
	C (3×3-40×40 cm^2)	-0.143	0.328	4.041
2×2	A (1×1-40×40 cm^2)	-0.305	0.865	3.743
	B (2×2-40×40 cm^2)	-0.102	0.345	1.538
	C (3×3-40×40 cm^2)	-0.265	0.772	3.457
3×3	A (1×1-40×40 cm^2)	-0.133	0.510	3.062
	B (2×2-40×40 cm^2)	0.056	-0.073	0.483
	C (3×3-40×40 cm^2)	-0.094	0.427	2.736
10×10	A (1×1-40×40 cm^2)	0.042	0.130	1.087
	B (2×2-40×40 cm^2)	0.187	-0.318	-0.346
	C (3×3-40×40 cm^2)	0.051	0.135	1.110

* Recommended values for the tolerances of depth dose verification are 2% for data at point beyond the d_{\max} (δ_1), 2 mm and 10% for data points in the build-up region (δ_{2b} and δ_{2b})

Table 6.2 The result of beam profile verification in 1×1, 2×2, 3×3 and 10×10 cm² at d_{max} depth of three beam data sets.

Field size (cm ²)	Beam data set	δ_3^* (%)	δ_4^* (%)	RW ₅₀ [*] (mm)	δ_{50-90}^* (mm)
1×1	A (1×1-40×40 cm ²)	-	-0.097	0.900	-0.010
	B (2×2-40×40 cm ²)	-	-0.097	0.890	0.020
	C (3×3-40×40 cm ²)	-	-0.116	0.990	-0.140
2×2	A (1×1-40×40 cm ²)	-0.250	-0.162	0.460	-0.130
	B (2×2-40×40 cm ²)	0.048	-0.155	0.300	-0.300
	C (3×3-40×40 cm ²)	-0.096	-0.161	0.520	-0.180
3×3	A (1×1-40×40 cm ²)	0.339	-0.213	-0.420	-0.190
	B (2×2-40×40 cm ²)	0.405	-0.203	0.380	-0.340
	C (3×3-40×40 cm ²)	0.382	-0.208	0.340	-0.270
10×10	A (1×1-40×40 cm ²)	-0.403	-0.074	0.640	-0.570
	B (2×2-40×40 cm ²)	-0.788	0.130	0.940	-0.430
	C (3×3-40×40 cm ²)	-0.303	-0.018	1.030	0.280

* Recommended values for the tolerances of beam profile verification are 3% for data point outside the central axis (δ_3) and point of off the beam edges (δ_4), the criteria of field width (RW₅₀) and beam fringe (δ_{50-90}) comparison is 2 mm.

Table 6.3 The result of beam profile verification in 1×1, 2×2, 3×3 and 10×10 cm² at 10 cm depth of three beam data sets.

Field size (cm ²)	Beam data set	δ_3^* (%)	δ_4^* (%)	RW ₅₀ [*] (mm)	δ_{50-90}^* (mm)
1×1	A (1×1-40×40 cm ²)	-	-0.105	0.780	-0.210
	B (2×2-40×40 cm ²)	-	-0.097	0.940	-0.200
	C (3×3-40×40 cm ²)	-	-0.104	0.760	-0.080
2×2	A (1×1-40×40 cm ²)	-0.798	-0.208	0.320	-0.260
	B (2×2-40×40 cm ²)	-0.784	-0.204	-0.390	-0.230
	C (3×3-40×40 cm ²)	-0.135	-0.202	0.390	-0.190
3×3	A (1×1-40×40 cm ²)	-0.625	-0.273	0.150	-0.420
	B (2×2-40×40 cm ²)	-0.420	-0.261	0.340	-0.400
	C (3×3-40×40 cm ²)	-0.478	-0.253	0.140	-0.380
10×10	A (1×1-40×40 cm ²)	0.253	-0.122	0.790	-0.300
	B (2×2-40×40 cm ²)	0.201	-0.159	0.770	-0.110
	C (3×3-40×40 cm ²)	0.166	-0.152	0.770	-0.170

* Recommended values for the tolerances of beam profile verification are 3% for data point outside the central axis (δ_3) and point of off the beam edges (δ_4), the criteria of field width (RW₅₀) and beam fringe (δ_{50-90}) comparison is 2 mm.

6.2 Accuracy of AAA 8.6 algorithm for IMRT dose calculation

Similar number of calculated monitor units, number of field segments including segmental shape and area were seen on three head and neck IMRT plans. Dose distributions were as well compared using plan evaluation tool, DVHs, on both the target volumes and organs at risk. No significant difference of the statistical dose data such as the minimum dose, mean and maximum dose in all structures was presented. The results suggested that addition of small field beam data smaller than 3×3 cm² did not affect on the calculated dose distribution in head and neck IMRT plans.

Typically, it is highly recommended from all guidelines for the accuracy verification of the TPS calculation algorithms. In this study, AAA 8.6 algorithm was

verified their accuracy by comparing the readings on planar dose distribution with the measured dose using 2D detector arrays (MapCHECK2TM). The comparison showed the dose variation at beam central axis was within $\pm 3\%$ on all three IMRT plans while the other measuring points contained a satisfactorily passing rate at more than 97% with the criteria 3% dose difference and 3 mm DTA. The passing rates was noticed that the decrease in IMRT plan was calculated with beam data set $2 \times 2\text{-}40 \times 40 \text{ cm}^2$ less than other plans. The gamma evaluation will fail in the other criteria that may induced from the improperly resolution use in the dose calculation. However, this result was in contrast with the readings obtained from using TLD-100 dosimeters. By almost of the measuring points (54/60), the TLD reading doses were higher by 9% average than the calculation. All three IMRT plans demonstrated a similar trend of the difference between the calculation and measurement.

The error of AAA 8.6 dose calculation was also reported and explained in the notification letter from Varian medical system to all affected customers on March 2011[44]. The report explained about the underestimation of the calculated dose in IMRT fields using AAA 8.6. They described that the impropriety has derives from the second source modeling for IMRT with multiple carriage group is incorrect. The delivered dose was estimated from the calculation can be less than the delivered locally by up to 10% and these errors can not be detected from dose measurement verification using 2D dose array tool. They suggest a few actions to avoid these unexpected errors. The first one, if it is possible, do not use the large field IMRT and user should unapproved the split-field treatment plan and recalculate it. They also advise the users to calculate IMRT dose distribution with other algorithms or use AAA version 8.9.

In this study, since the Eclipse TPS used in this study was upgraded for AAA 8.9 algorithm. Thus, recalculation with AAA 8.9 algorithm based on the routine beam commissioning data were performed and compared with the AAA 8.6 algorithm. It can be seen that most of the observed points on AAA 8.9, showed the higher absorbed dose than AAA 8.6 as presented in Fig 6.1. However, the underestimation of the calculated dose still be shown in the range of -5 to -15% when compared to the measurements. In our investigation, the most dose discrepancy was observed in the measured point near air cavity. Moreover, the reading on studied points which near or

at the high dose gradient area may also affect from uncertainty of the TLD positioning in the phantom holes as well as the uncertainty from phantom positioning in each experiment.

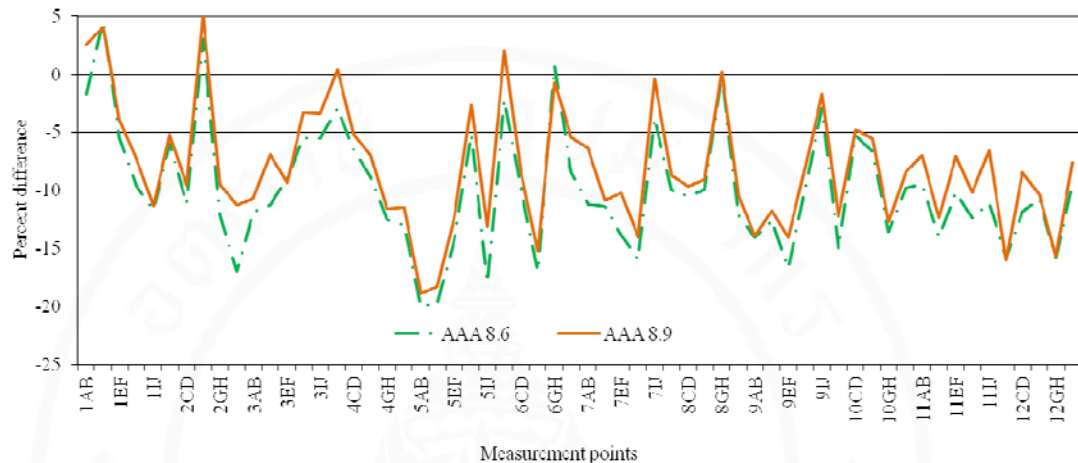


Figure 6.1 Percent dose difference between calculation and measurement at each TLD point in humanoid head and neck phantom, compared between AAA 8.6 and 8.9 version.

This study shows that the addition of small field beam data did not affect on the accuracy of dose calculation in the Head and Neck IMRT plan. Although this plan consists of multiple small radiation fields, those small fields are defined by the MLC instead of the jaws. Moreover the sizes of the jaw were opened a much larger than $3 \times 3 \text{ cm}^2$. This result obtains similar to the work done by Azimi R et al. [45] They revealed that small field output factor was insignificant to the accuracy of IMRT dose calculation in Varian machine because most of the jaws were opened widely and fixed for all segments to deliver each IMRT beam. Further study need to be performed in the stereotactic radiosurgery technique. This technique represents the true small field defined by jaws which worth to concern especially in the inhomogeneity areas. Moreover the ideal dosimeter needs to have a linear response, energy and dose rate independent, high spatial resolution and water equivalence therefore other than TLD, radiochromic film dosimetry is other choices to be recommended to reduce laborious work and uncertainty from the TLD measurement.

6.3 Conclusion

It can be concluded from the study that, an additional of the small field, 1×1 and 2×2 cm², beam data for the AAA 8.6 commissioning do not affect on the quality of head and neck IMRT dose calculation. Suitable beam data acquisition for Eclipse TPS can be performed from the smallest field 3×3 cm² to the largest 40×40 cm². However, the underestimation of AAA dose calculation, especially in the inhomogeneity area should be aware for their accuracy.

REFERENCES

1. Parkin DM, Bray F, Ferlay J and Pisani P. Global cancer statistics 2002. *A Cancer Journal for Clinicians* 2005; 55: 74-108.
2. Lee N, Puri DR, Blanco AI, Chao KS. Intensity-modulated radiation therapy in head and neck cancers: an update. *Head Neck*. 2007; 29(4): 387-400.
3. Hunt MA, Zelefsky MJ, Wolden S, Chui CS, LoSasso T, Rosenzweig K, Chong L, Spirou SV, Fromme L, Lumley M, Amols HA, Ling CC, Leibel SA. Treatment planning and delivery of intensity-modulated radiation therapy for primary nasopharynx cancer. *Int J Radiat Oncol Biol Phys*. 2001 ; 49: 623-32.
4. Bucci MK, Bevan A, Roach M 3rd. Advances in radiation therapy: conventional to 3D, to IMRT, to 4D, and beyond. *CA Cancer L Clin* 2005; 55: 117-34.
5. Bhide SA, Nutting CM. Radiotherapy: Future directions in head and neck cancer. *Oncology news* 2007; 1: 7-9.
6. Hale BC, Aaron MA. Intensity-modulated radiotherapy for head and neck cancer. *Clinical advances in Hematology & Oncology* 2007; 5: 425-431.
7. Khan FM, Stathakis S. Modern radiation therapy: Intensity-modulated radiation therapy. *The physics of radiation therapy* 2010: 481-505.
8. Ezzell GA, Galvin JM, Low D, Palta JR, Rosen I, Sharpe MB, Xia P, Xiao Y, Xing L and Yu CX. Guidance document on delivery, treatment planning, and clinical implementation of IMRT: report of the IMRT Subcommittee of the AAPM Radiation Therapy Committee. *Med Phys* 2003; 30: 2089-2115.
9. Schlegel W, Mahr A. 3D conformal radiation therapy: multimedia introductions to methods and techniques, Heidelberg; Springer (e-book) 2001.
10. Jeffrey V Siebers. Dose calculation for IMRT. *Image-guided IMRT* 2006: 61-71.
11. Uwe Oelke and Christian Scholz. Dose calculation algorithms; New technologies in radiation oncology, *Medical Radiology* 2006; part3: 187-196.

12. ICRU Report 29 Dose Specification for Reporting External Beam Therapy with Photons and Electrons, was published in 1978.
13. Fraass B, Doppke K, Hunt M, Kutcher G, Starkschall G, Stern R, Van Dyke J. American Association of Physicists in Medicine Radiation Therapy Committee Task Group 53: quality assurance for clinical radiotherapy treatment planning. *Med Phys* 1998; 25: 1773-1829.
14. Das IJ, Cheng CW, Watts RJ, Ahnesjo A, Gibbons J, Li XA, Lowenstein J, Mitra RK, Simon WE, Zhu TC. Accelerator beam data commissioning equipment and procedures: Report of the TG-106 of the Therapy Physics Committee of the AAPM. *Med Phys* 2008; 35: 4186-4215.
15. Das IJ, Ding GX, Ahnesjo A. Small fields: nonequilibrium radiation dosimetry. *Med Phys* 2008; 35: 206-215.
16. Miller DW, Bloch PH, Curran BH, Ibbott GS, Jones D, Jucius SZ, Leavit DD, Mohan R, Geijn JV. American Association of Physicists in Medicine Radiation Therapy Committee Task Group 23: Radiation treatment planning dosimetry verification. American Institute of Physics 1995.
17. Gifford KA, Followill D, Liu H, Starkschall G. Verification of the accuracy of a photon dose calculation algorithm. *J. Appl. Clin. Med Phys* 2002; 3: 26-45.
18. Andres M. and Manfred S. Dosimetry, 2007. <http://www.sasro.ch/SRO/phys2011/Dosimetry.pdf>.
19. Azcona JD, Siochi RA, Azinovic I. Quality assurance in IMRT: importance of the transmission through the jaws for an accurate calculation of absolute doses and relative distributions. *Med Phys* 2002; 29: 269-274.
20. Sohn JW, Dempsey JF, Suh TS, Low DA. Analysis of various beamlet sizes for IMRT with 6 MV photons. *Med Phys* 2003; 30: 2432-2439.
21. Cheng CW, Das IJ, Hug MS. Lateral loss and dose discrepancies of multileaf collimator segments in intensity modulated radiation therapy. *Med Phys* 2003; 30: 2959-2968.
22. Fogliata A, Nicolini G, Vanetti E, Clivio A, Cozzi L. Dosimetric validation of the anisotropic analytical algorithm for photon dose calculation: fundamental characterization in water. *Phys Med Biol* 2006; 51:1421-38.

23. Bragg CM, Conway J. Dosimetric verification of the anisotropic analytical algorithm for radiotherapy treatment planning: *Radiother Oncol* 2006; 81: 315-23.
24. Bragg CM, Wingate K, Conway J. Clinical implications of the anisotropic analytical algorithm for IMRT treatment planning and verification: *Radiother Oncol* 2008; 86: 276-84.
25. Van Esch A, Tillikainen L, Pyykkonen J, Tenhunen M, Helminen H, Siljamäki S, Alakuijala J, Paiusco M, Lori M, Huyskens DP. Testing of the analytical anisotropic algorithm for photon dose calculation: *Med Phys* 2006; 33: 4130-48.
26. Breitman K, Rethee S, Newcomb C, Murray B, Robinson D, Field C, Warkentin H, Connors S, MacKenzie M, Dunscombe P, Fallone G. Experimental validation of the Eclipse AAA algorithm: *J Appl Clin Med Phys* 2007 ; 8:76-92.
27. Kan MW, Cheung JY, Leung LH, Lau BM, Yu PK. The accuracy of dose calculations by anisotropic analytical algorithms for stereotactic radiotherapy in nasopharyngeal carcinoma: *Phys Med Biol* 2011; 56: 397-413.
28. Wellhofer dosimetric GmbH. Blue phantom manual, Germany: 2001.
29. CIVCO medical solution. Radiation oncology sourcebook: 2001.
30. Fraser D, Parker W, Seuntjens J. Characterization of cylindrical ionization chambers for patient specific IMRT QA. *J Appl Clin Med Phys*. 2009; 10: 241-251.
31. PTW Freiburg GmbH. Small field dosimetry application guide: 2011.
32. IBA Dosimetry GmbH. Detectors for relative and absolute dosimetry: 2009. <http://www.iba-dosimetry.com/complete-solutions/radiotherapy/relative-dosimetry/products>.
33. IBA Dosimetry GmbH. DOSE1 brochure: 2009. <http://www.iba-dosimetry.com/complete-solutions/radiotherapy/absolute-dosimetry/dose-1>.
34. Varian medical system, Inc. CLINAC accelerators: 2000. <http://home.c2i.net/ntoerres/brystkreft/clinac.pdf>.

35. Varian medical system, Inc. EclipseTM treatment planning system: 2006.
http://www.haedong.co.kr/product/product_download.php?idx=126.
36. Radiology support devices Inc. The Alderson radiation therapy phantom (ART).
<http://www.rsdphantoms.com/pdf/aldersonradiationtherapy.pdf>.
37. Philips Healthcare. Brilliance CT-Big Bore Oncology. http://www.healthcare.philips.com/in_en/products/ct/products/ct_brilliance_big_bore_oncology/index.wpd
38. Thermo Fisher Scientific Inc. TLD-100 Thermoluminescent Dosimetry Material.
<http://www.thermoscientific.com/ecom/servlet/productsdetail?productId=11961431&groupType=PRODUCT&searchType=0&storeId=11152&from=search>.
39. Thermo Fisher Scientific Inc. Harshaw 5500 automatic dosimetry reader.
<http://www.envinet.cz/pt/files/thermo/TLDMModel5500.pdf>.
40. PTW Freiburg GmbH. TLDO Annealing Oven: 2011. http://www.ptw.de/tldo_annealing_oven.html.
41. SUN NUCLEAR Corporation. MapCHECK 2TM data sheet: 2011. <http://www.sunnuclear.com/documents/mapcheck.pdf>.
42. Venselaar J, Welleweerd H, Mijnheer B. Tolerance for the accuracy of photon beam dose calculations of treatment planning systems: Radiother. Oncol; 60: 191-201.
43. A phase II study of intensity-modulated radiation therapy (IMRT) +/- chemotherapy for nasopharyngeal cancer: The Radiation Therapy Oncology Group (RTOG 0225) of the American College of Radiology (ACR) 2003; 6: 5-7.
44. Varian medical system, Inc. Urgent medical device correction and field safety notice. 2011 (March).
45. Azimi R, Alaei P, Higgins P. The effect of small field output factor measurements on IMRT dosimetry: Med Phys 2012; 39: 4691-4.



APPENDICES

APPENDIX A

Anisotropic Analytical Algorithm (AAA)

AAA is a new algorithm in Eclipse treatment planning system for photon dose calculation. It is a three-dimension (3D) pencil beam convolution/superposition algorithm which uses Monte Carlo drive kernels of multiple sources. The dose deposition characteristics are modeled with the mathematical formalism that enable analytical convolution (which significantly reduces the computational time). The AAA accounts for tissue heterogeneity anisotropically in the entire 3D neighborhood of an interaction site. The final dose distribution is obtained by the superposition of photon and electron convolution.

The clinical implementation of AAA for the dose calculation is divided into two parts (dose calculation and configuration algorithm).

- The configuration algorithm: It is used to determine the fundamental physical parameters required for the dose calculation. The clinical beam is described by multiple source models which are primary photon, scattered extra-focal photon and electron scattered. The first term models the initial photon spectra resulting from Bremsstrahlung interaction on the target not interacting in the treatment head. The second model the additional photons generated in the flattening filter, primary collimator and the secondary jaws. The third component describes the electrons created mainly by Compton interaction in the head of treatment machine and in air. Each source is modeled by optimizing a number of parameters and correction curves in order to obtain the agreement between calculated and measured basic beam data.

- The dose calculation algorithm: It calculates the dose deposition using the physical parameters defined beamlets. The parameters characterize the particle fluences and energy spectra of the photons and electrons comprising the clinical beam. The dose calculation is based on the convolution and the final dose distribution is obtained as a superposition for every beamlet.

The dose from each beamlet being calculated through a convolution of three sources. The dose contribution $D_{\beta}(x,y,z)$ from beamlets is modeled fluence Φ and energy deposition density function $I(z, p)$ with scatter kernel $K(x, y, z, p)$, that defines the lateral dose scattering in the phantom:

$$D_{\beta}(x, y, z) = \phi_{\beta} \times I_{\beta}(z, \rho) \times \iint_{\beta} K_{\beta}(x'-x, y'-y, z, \rho) dx' dy' \quad (\text{A.1})$$

Each contributing function is defined separately for each of the energy fluence components. The scatter kernels are density dependent and are evaluated in multiple directions laterally from the beamlet. The photon scatter is convolved with density-scaled kernel along the beamlet direction to more accurately reproduce the dose at the border of heterogeneities

APPENDIX B

TPS calculated beam depth doses and profiles verification

To validate the commissioning beam data generated from AAA 8.6 algorithm were verified with those from measurements. Comparison of the depth doses and profiles between the calculated and measured in different field sizes and depths showed an excellent agreement. Figure B.1-B.8 presented the depth doses of beam data set B (2×2 - 40×40 cm²) and C (3×3 - 40×40 cm²) in the range of field size 1×1 - 3×3 and 10×10 cm². And figure B.9-B.16 showed the profiles of beam data set B and C in the same field size at d_{\max} and 10 cm depths.

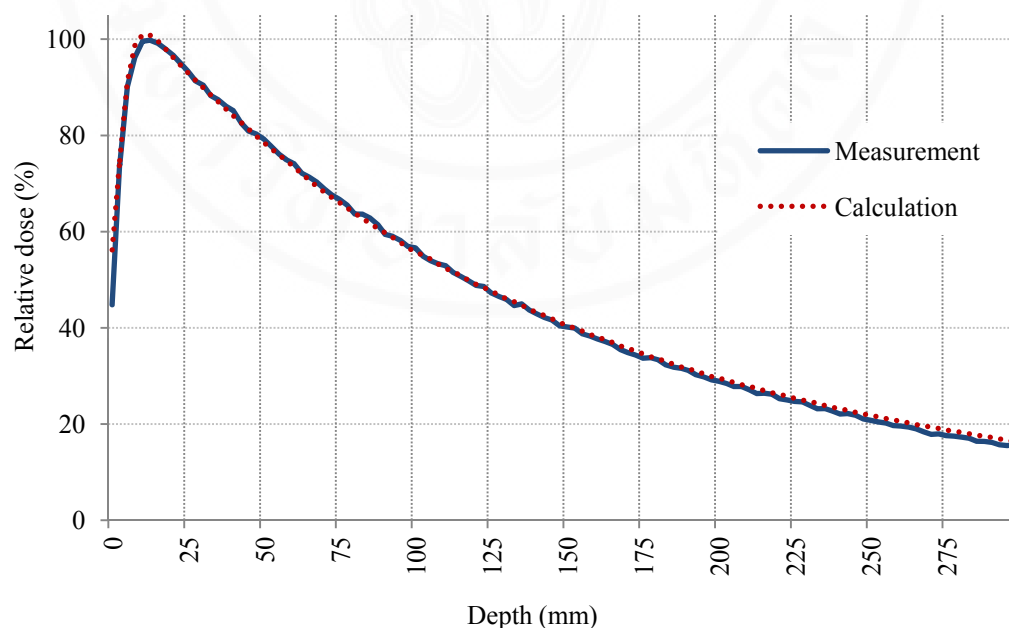


Figure B.1 The comparison of PDD curves between the calculation (red) and measurement (blue) on beam data set B (2×2 - 40×40 cm²) in 1×1 cm² field size at 100 cm SSD.

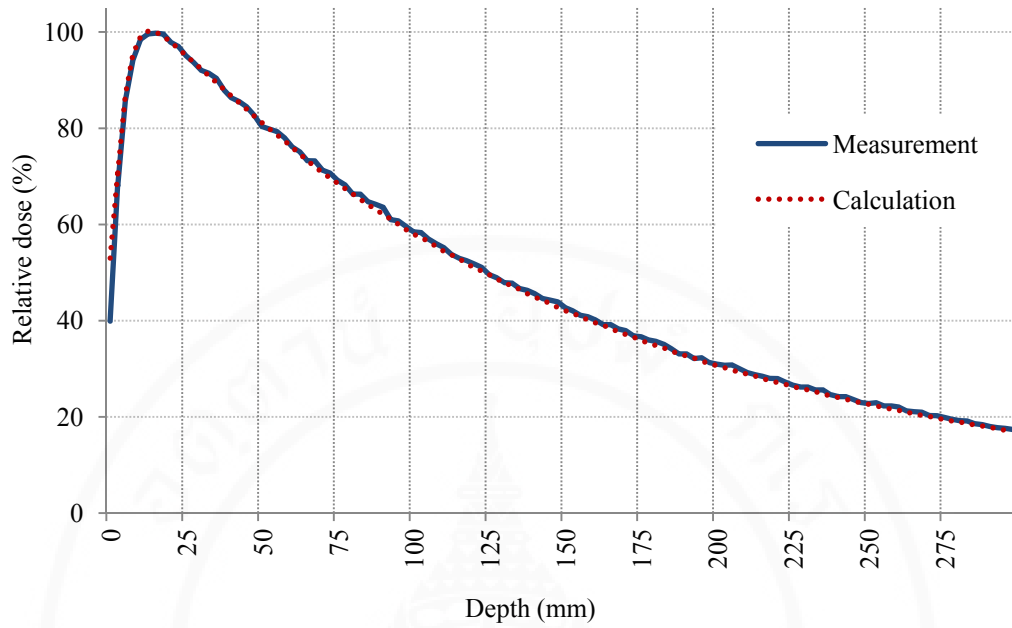


Figure B.2 The comparison of PDD curves between the calculation (red) and measurement (blue) on beam data set B (2×2 - 40×40 cm²) in 2×2 cm² field size at 100 cm SSD.

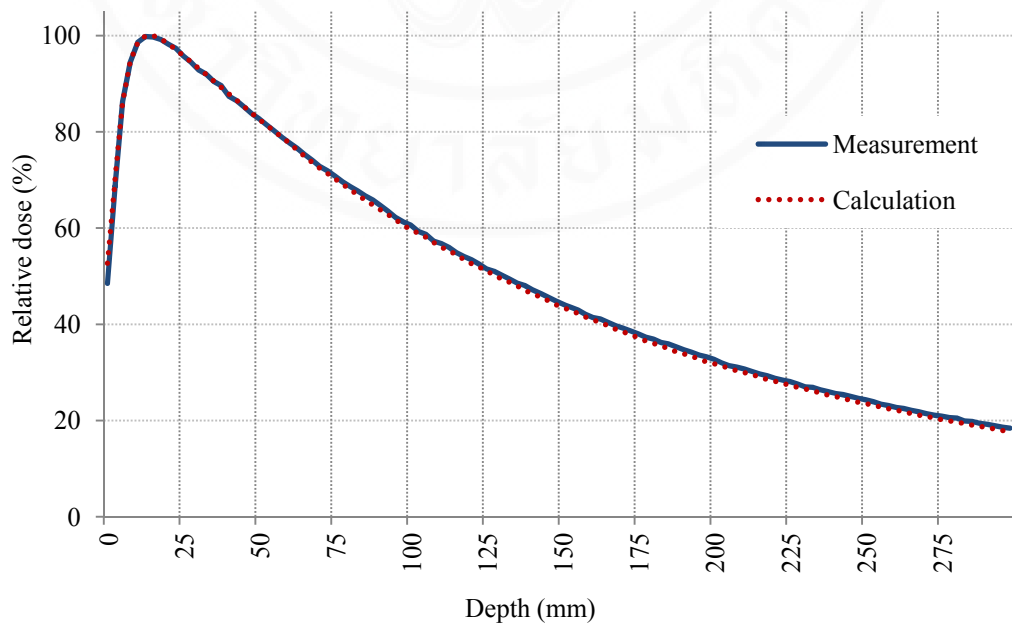


Figure B.3 The comparison of PDD curves between the calculation (red) and measurement (blue) on beam data set B (2×2 - 40×40 cm²) in 3×3 cm² field size at 100 cm SSD.

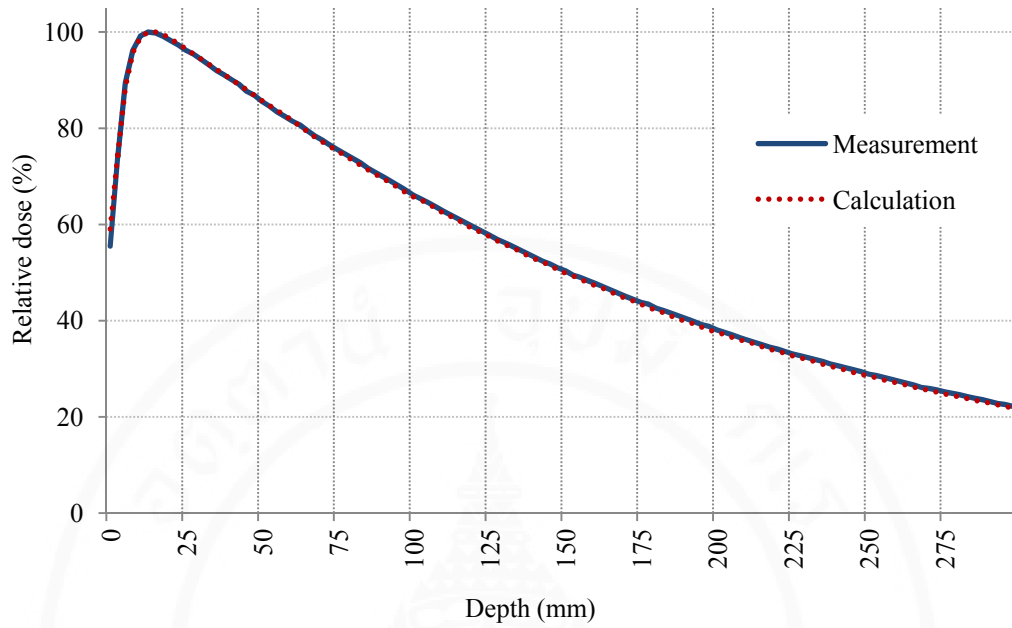


Figure B.4 The comparison of PDD curves between the calculation (red) and measurement (blue) on beam data set B (2×2 - 40×40 cm²) in 10×10 cm² field size at 100 cm SSD.

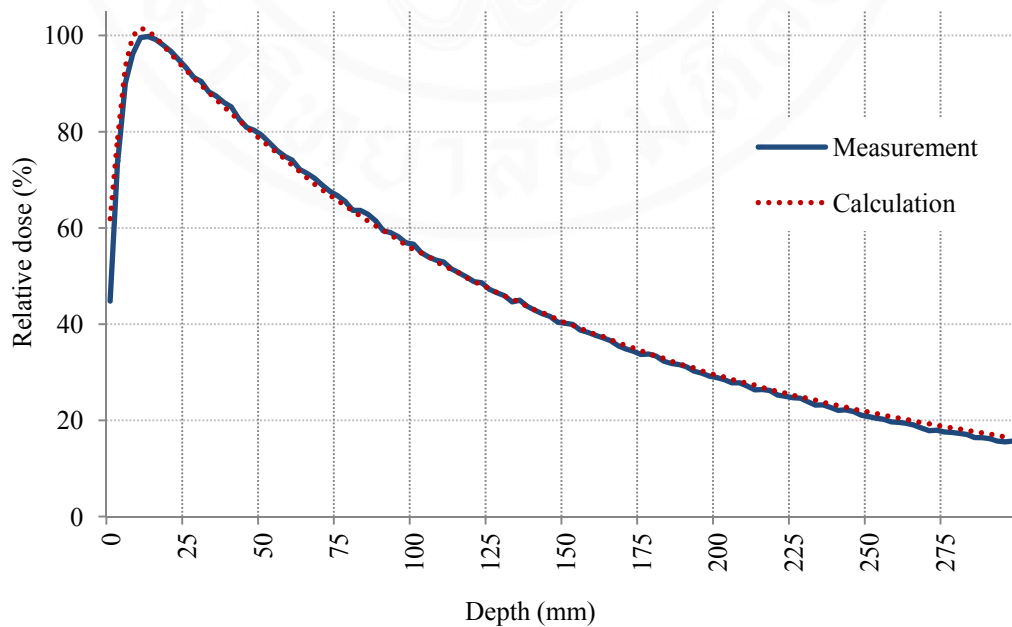


Figure B.5 The comparison of PDD curves between the calculation (red) and measurement (blue) on beam data set C (3×3 - 40×40 cm²) in 1×1 cm² field size at 100 cm SSD.

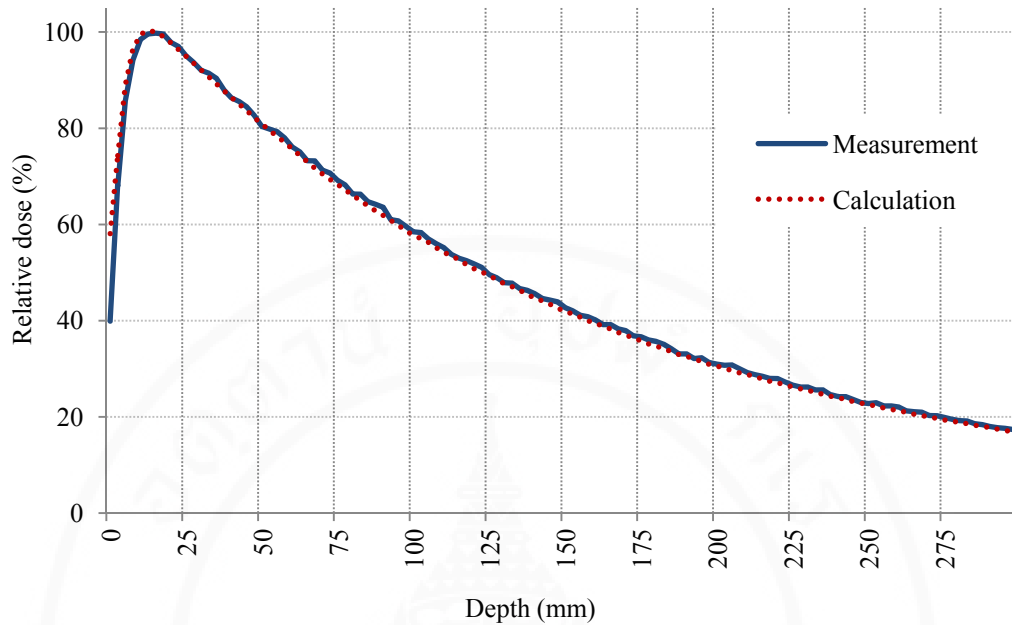


Figure B.6 The comparison of PDD curves between the calculation (red) and measurement (blue) on beam data set C ($3\times 3-40\times 40\text{ cm}^2$) in $2\times 2\text{ cm}^2$ field size at 100 cm SSD.

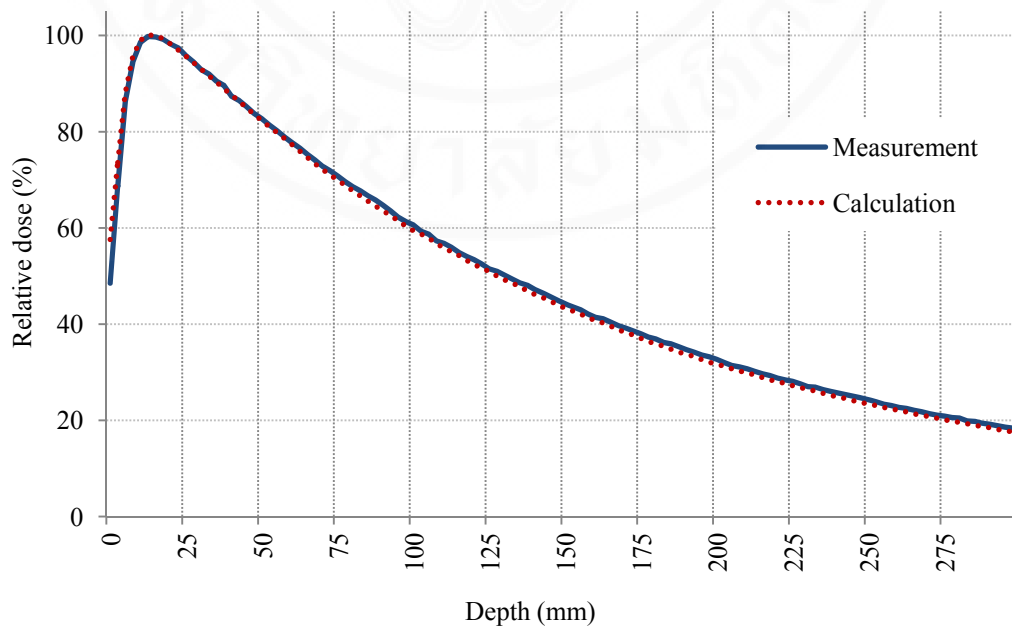


Figure B.7 The comparison of PDD curves between the calculation (red) and measurement (blue) on beam data set C ($3\times 3-40\times 40\text{ cm}^2$) in $3\times 3\text{ cm}^2$ field size at 100 cm SSD.

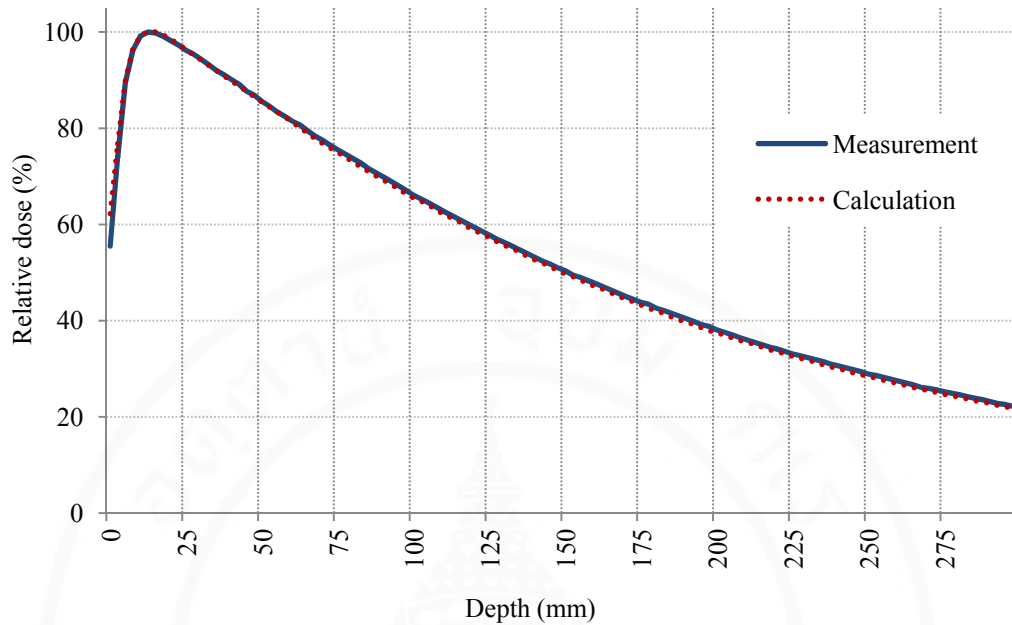


Figure B.8 The comparison of PDD curves between the calculation (red) and measurement (blue) on beam data set C (3×3 - 40×40 cm²) in 10×10 cm² field size at 100 cm SSD.

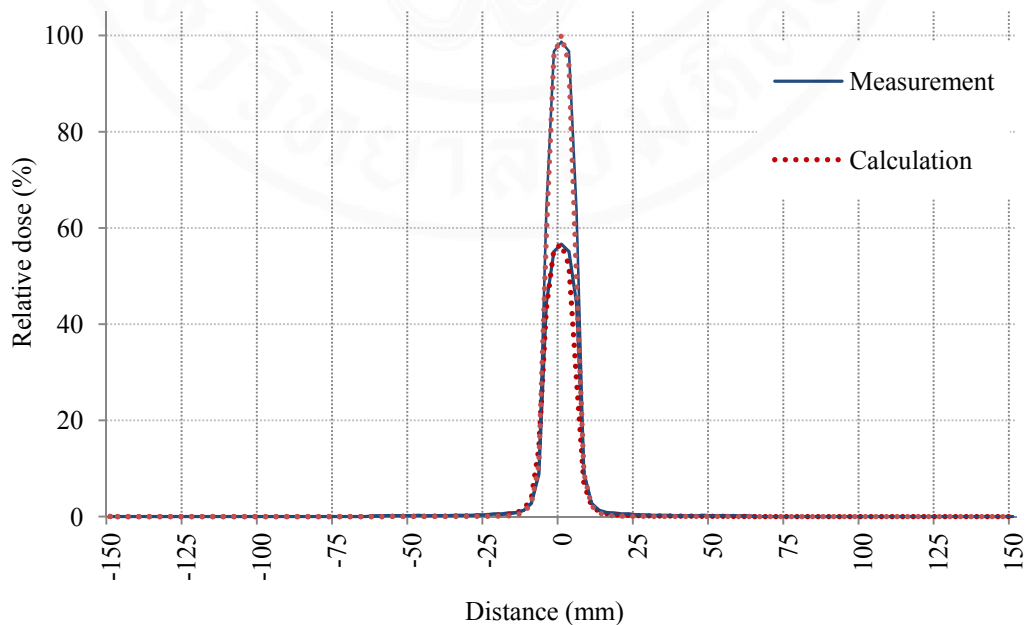


Figure B.9 Comparison of the cross plane profiles between calculation (red) and measurement (blue) in 1×1 cm² field size from beam commissioning data set B (2×2 - 40×40 cm²)

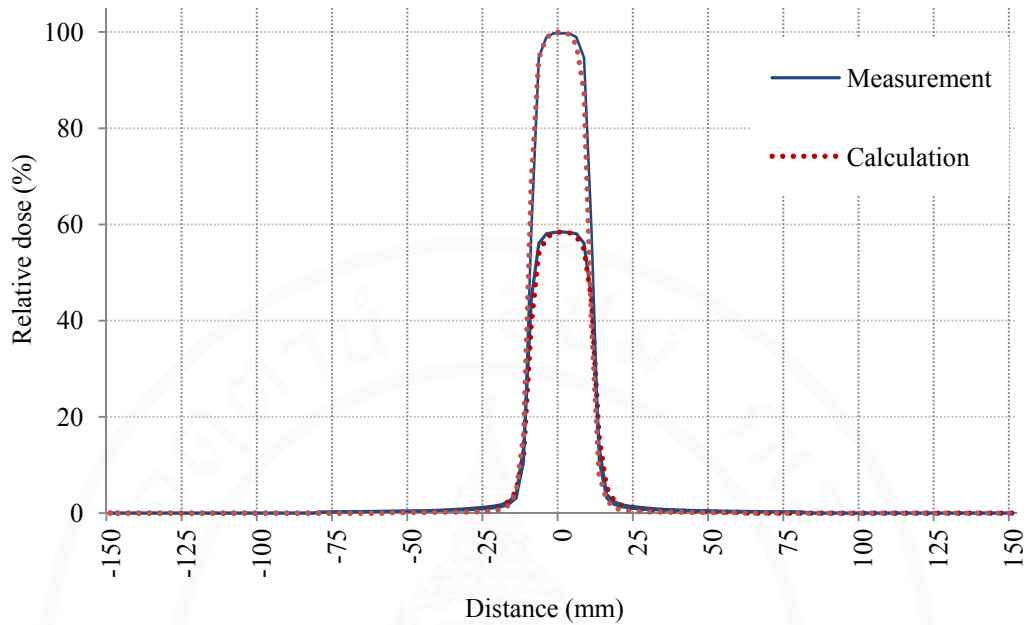


Figure B.10 Comparison of the cross plane profiles between calculation (red) and measurement (blue) in $2 \times 2 \text{ cm}^2$ field size from beam commissioning data set B (2×2 - $40 \times 40 \text{ cm}^2$)

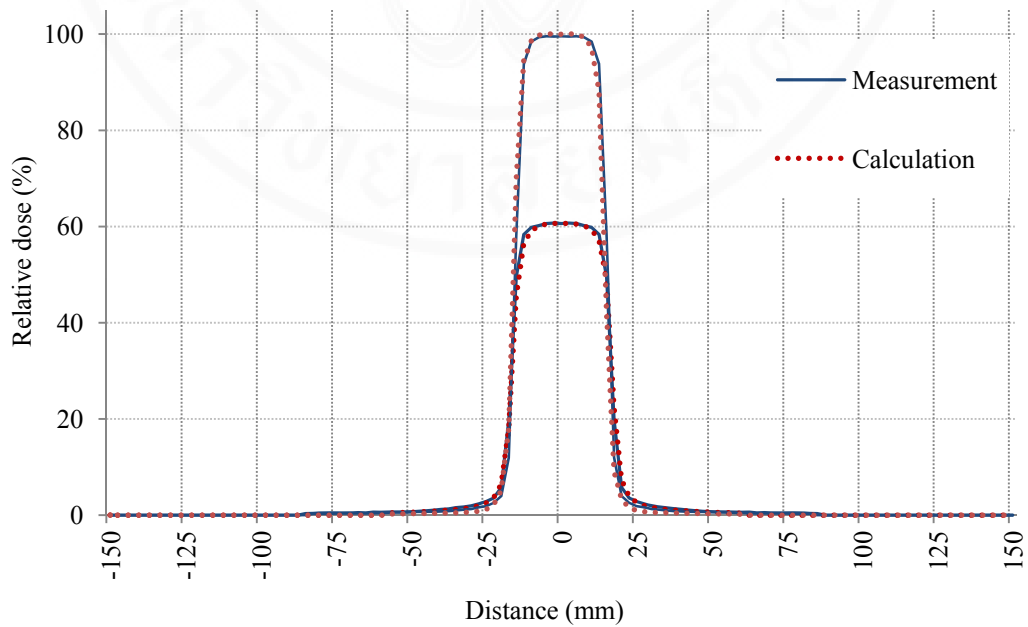


Figure B.11 Comparison of the cross plane profiles between calculation (red) and measurement (blue) in $3 \times 3 \text{ cm}^2$ field size from beam commissioning data set B (2×2 - $40 \times 40 \text{ cm}^2$)

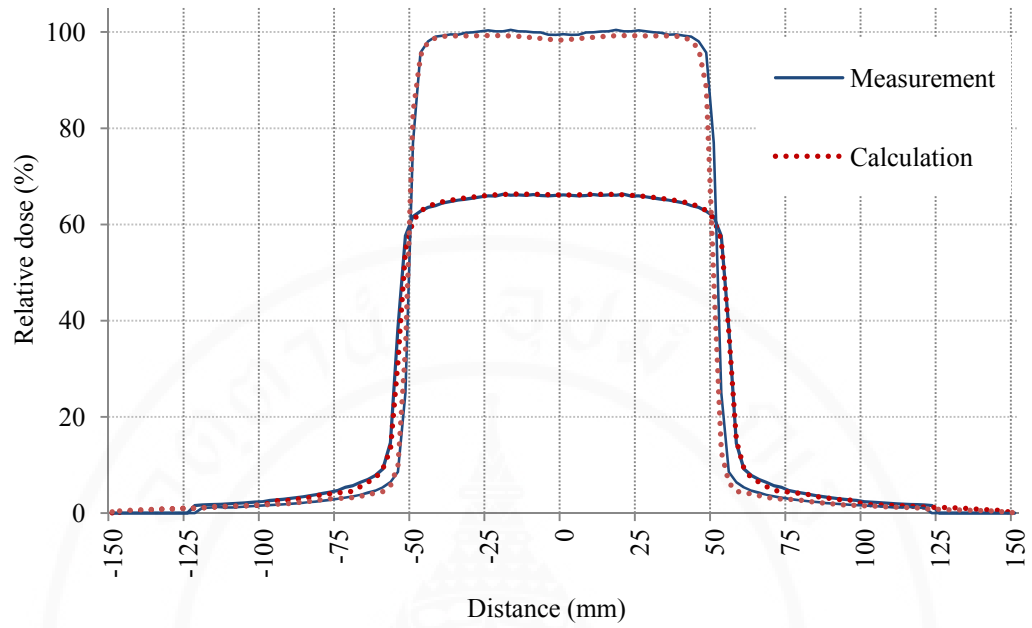


Figure B.12 Comparison of the cross plane profiles between calculation (red) and measurement (blue) in $10 \times 10 \text{ cm}^2$ field size from beam commissioning data set B (2×2 - $40 \times 40 \text{ cm}^2$)

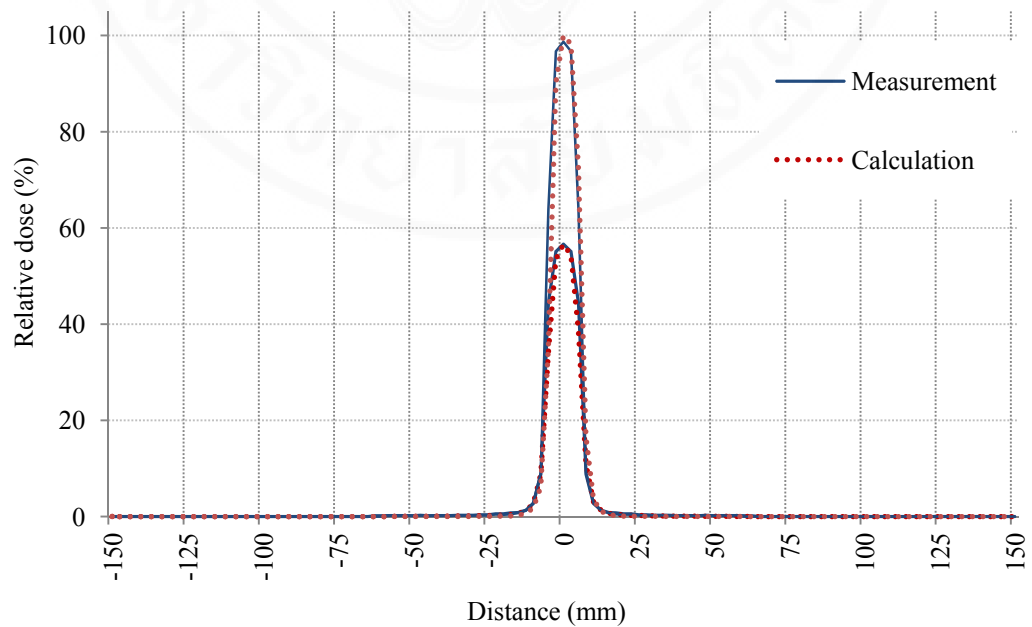


Figure B.13 Comparison of the cross plane profiles between calculation (red) and measurement (blue) in $1 \times 1 \text{ cm}^2$ field size from beam commissioning data set C (3×3 - $40 \times 40 \text{ cm}^2$).

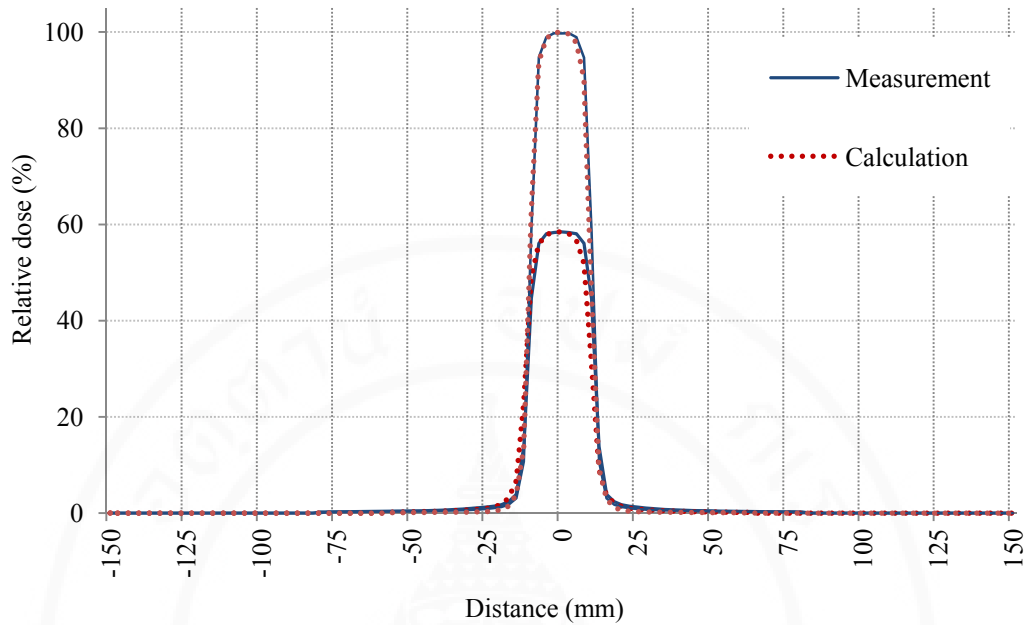


Figure B.14 Comparison of the cross plane profiles between calculation (red) and measurement (blue) in $2 \times 2 \text{ cm}^2$ field size from beam commissioning data set C (3×3 - $40 \times 40 \text{ cm}^2$)

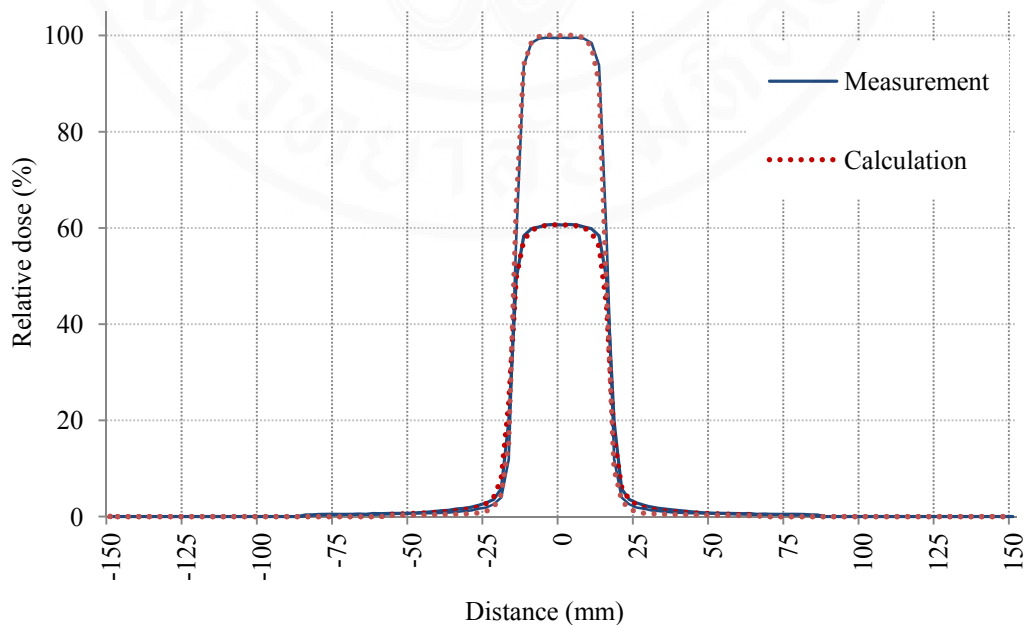


Figure B.15 Comparison of the cross plane profiles between calculation (red) and measurement (blue) in $3 \times 3 \text{ cm}^2$ field size from beam commissioning data set C (3×3 - $40 \times 40 \text{ cm}^2$)

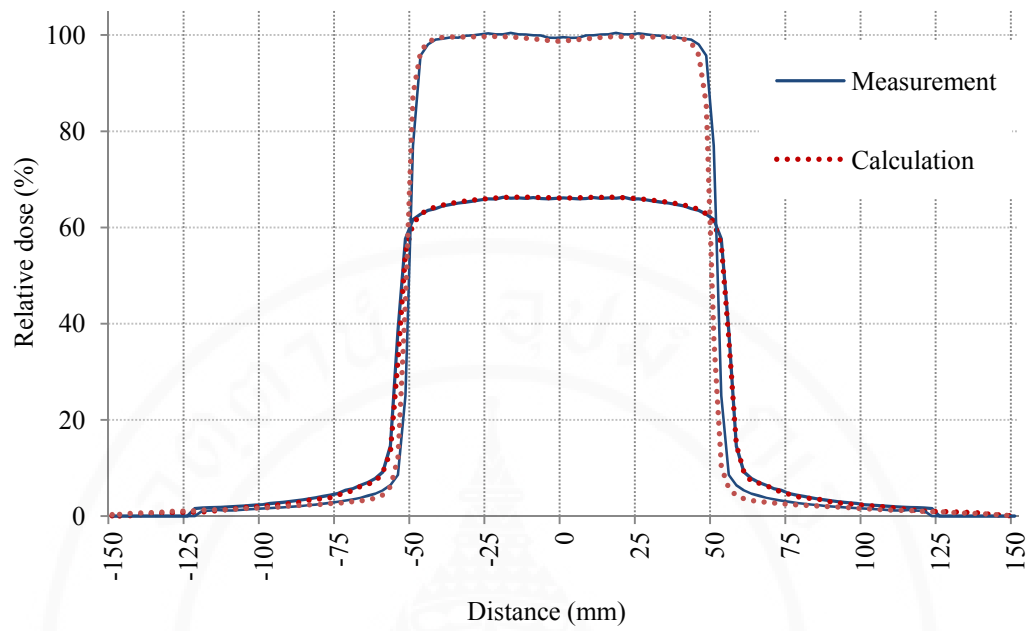


Figure B.16 Comparison of the cross plane profiles between calculation (red) and measurement (blue) in $10 \times 10 \text{ cm}^2$ field size from beam commissioning data set C (3×3 - $40 \times 40 \text{ cm}^2$)

BIOGRAPHY

NAME Miss Thida Niyomthai

DATE OF BIRTH 7 March 1977

PLACE OF BIRTH Bangkok, Thailand

INSTITUTIONS ATTENDED Mahidol University, 1994-1998
Bachelor of Science
(Radiological Technology)

Mahidol University, 2009-2013
Master of Science
(Medical Physics)

OFFICE National Cancer Institute
268/1 Rama VI road, Thungpayathai
Rajthevee, Bangkok, Thailand 10400
Tel. 0-2354-7028

HOME ADDRESS 40/41 Soi Petchkasem 77/4,
Petchkasem road, Nongkangploo,
Nongkhaem, Bangkok, Thailand 10160
Tel. 0-2809-9311
E-mail: thida.niyomthai@gmail.com